Oligodendroglial anillin facilitates septin assembly to prevent myelin outfoldings

Dissertation

for the award of the degree
"Doctor rerum naturalium" (Dr. rer. nat)
of the Georg-August University Göttingen

within the doctoral program Biology
of the Georg-August University School of Science (GAUSS)

submitted by
Michelle Scarlett Erwig
from Neuss, Germany

Göttingen, November 2018

Members of the Examination Board:

Thesis committee:

PD Dr. Hauke Werner (Reviewer)
Department of Neurogenetics
Max Planck Institute of Experimental Medicine

Prof. Dr. Siegrid Löwel (Reviewer)
Department of Systems Neuroscience
Georg-August University, Göttingen

Further members of the Examination Board:

Prof. Dr. Martin Göpfert
Department of Cellular Neurobiology
Schwann-Schleiden Research Centre
Georg-August University, Göttingen

Prof. Dr. Ralf Heinrich
Department of Cellular Neurobiology
Schwann-Schleiden Research Centre
Georg-August University, Göttingen

Prof. Dr. Dr. Hannelore Ehrenreich
Department of Clinical Neuroscience
Max Planck Institute of Experimental Medicine

Prof. Dr. Alexander Flügel
Institute for Neuroimmunology and Multiple Sclerosis Research
University Medical Center Göttingen

Date of oral examination: January 28th, 2019

Declaration

I hereby declare that the Ph.D. thesis entitled “Oligodendroglial anillin facilitates septin assembly to prevent myelin outfoldings”, has been written independently and with no other sources and aids than quoted.

Göttingen, November 27th, 2018

_____
Michelle Erwig

Für meine Eltern.

Danksagung

Ich möchte Prof. Klaus-Armin Nave Ph.D. danken, dass ich in seiner Abteilung arbeiten konnte. Danke für wissenschaftliche Diskussionen und eine Arbeitsatmosphäre in der alle auf einem Level diskutieren können.

Ein großer Dank geht an PD Dr. Hauke Werner. Danke für die Betreuung der Arbeit und die Zusammenarbeit. Die wissenschaftlichen Diskussionen sowie die familiäre Arbeitsatmosphäre aber auch das Ermutigen, sich weiter zu entwickeln, werden mir immer in guter Erinnerung bleiben.

Des Weiteren möchte ich Prof. Dr. Sigrid Löwel dafür danken, dass sie das Amt der zweiten Betreuerin übernommen hat. Danke für hilfreiche Diskussionen in den TCMs und die unkomplizierte Betreuung.

Ein weiteres Danke geht an Dr. Julia Patzig, die dieses Projekt begonnen hat und mir so viel beigebracht hat.

Ulrike Bode, Annette Fahrenholz, Torben Ruhwedel, Christos Naidis und Uschi Kutzke möchte ich für all die technische Hilfe danken.

Danke an Dr. Wiebke Möbius und Dr. Anna Steyer für Hilfe aller Art in der Elektronenmikroskopie. Danke, dass ihr euer Wissen mit mir geteilt habt und auf so wunderbare Weise zu dieser Arbeit beigetragen habt.

Danke an unsere Kollaboratoren: Dr. Olaf Jahn für die Proteomanalyse und Hilfe bei angefallenen Fragen; Prof. Dr. Ingo Heilmann für die PIP_2 Messungen; Dr. Payam Dibaj für die elektrophysiologischen Messungen. Danke für die reibungslose und unkomplizierte Zusammenarbeit.

Ebenfalls ein großer Dank geht an Dr. Kathrin Kusch. Danke für deine Hilfe, deine Geduld und, dass du dein Wissen mit mir geteilt hast.

Von Herzen danken möchte ich Ramona Jung. Danke für all deine Hilfe ob während der Elternzeit oder wenn sonst etwas schief gegangen ist.

Ein großer Dank geht an die AG Werner. Es war eine schöne Zeit mit euch zu arbeiten, zu diskutieren, zu singen, zu tanzen, zu kochen & essen und immer wieder auch zu lachen.

Ein extra Danke geht an Lena, Lisa und Maria. Unsere Diskussionen und eure Korrekturen haben zur Fertigstellung dieser Arbeit beigetragen.

Ein großer Dank geht an die Tierpfleger Marion Peine und Kerstin Claus. Danke, dass ihr immer ein Auge auf meine Tiere hattet und unsere Zusammenarbeit so reibungslos verlief. Eure Arbeit war die Grundlage für all meine Experimente.

Danke ebenfalls an die glorreichen 6. 2007 haben wir unser Abenteuer in Göttingen begonnen und den Entschluss gefasst, dieses eine Mädchen zu küssen. Aus Fremden sind dabei Freunde geworden; danke, dass ihr immer für mich da seid.

Besonders dankbar bin ich für meine Familie: Mama, Papa, Natalie und Christopher danke für eure Unterstützung und all die Liebe.

Von ganzem Herzen möchte ich Jan Erwig danken. Du hast immer an mich geglaubt und mir immer den Rücken gestärkt. Danke, dass du mich verstehst, so geduldig bist und mich so liebst wie ich bin. Danke für unsere wunderbare Tochter und dafür, dass du Karlotta der beste Papa der Welt bist.

Content

List of Figures

Abbreviations

Abbreviation	Full form
3D	Three dimensional
Akt	RAC-alpha serine/threonine-protein kinase (Protein kinase B)
Anln	Anillin (gene)
Anln cKO	$Anln^{fl/fl};Cnp^{Cre/Wt}$
ANOVA	Analysis of variance
APS	Ammonium persulfate
BBB	Blood brain barrier
bp	Base pairs
BSA	Bovine serum albumin
°C	Degrees Celsius
cDNA	Complementary DNA
cKO	Conditional knockout
CLAHE	Contrast Limited Adaptive Histogram Equalization
CNS	Central nervous system
CRISPR	Clustered regularly interspaced short palindromic repeats
DAB	3,3'-Diaminobenzidine
DAPI	4'-6-Diamidino-2-phenylindole
ddH_2O	Double-distilled water
DDSA	Dodecenylsuccinic anhydride
DDT	Dichlorodiphenyltrichloroethane
Dhh	Desert hedgehog
DMP-30	2,4,6-Tris(dimethylaminomethyl)phenol
DNA	Deoxyribonucleic acid
dNTP	Deoxyribonucleoside triphosphate
DPSS	Diode-pumped solid-state
ECL	Enhanced chemiluminescence
EDTA	Ethylenediaminetetraacetic acid
e.g.	*Exempli gratia*
EM	Electron microscopy
Erk	Extracellular signal–regulated kinase
ES	Embryonic stem
EUCOMM	European Conditional Mouse Mutagenesis Program

F-actin	Filamentous actin
FIB SEM	Focused ion beam scanning electron microscopy
FPKM	Fragments per kilobase of exon per million fragments mapped
FVB	Friend leukemia virus B
g	Gramm
g	Gravity
G-actin	Globular actin
GTP	Guanosine triphosphate
GS	Goat serum
h	Hour
HBSS	Hank's Balanced Salt Solution
HGNC	HUGO gene nomenclature committee
HNA	Hereditary neuralgic amyotrophy
HRP	Horseradish peroxidase
HS	Horse serum
i.e.	*Id est* (that is)
i.p.	Interperitoneally
JXP	Juxtaparanode
kDa	Kilodalton
K&S	Karlsson-Schultz fixative
kV	Kilovolt
log_2 FC	Log_2 fold change
LSAB	Labelled streptavidin biotin
M	Molar
mA	Milliampere
MGB	Modified Gitschier buffer
µg	Microgram
min	Minutes
mm	Millimeter
MNA	Methyl nadic anhydride
ml	Milliliter
µl	Microliter
mM	Millimolar
mm	Millimeter
µM	Micromolar
µm	Micrometer
mo	Month

MPI EM	Max-Planck-Institute of Experimental Medicine
mRNA	Messenger RNA
MS	Mass spectrometry
mTOR	Rapamycin
N	Normality
n	Number (biological replicates)
nA	Nanoampere
ng	Nanogram
NgR1	Nogo receptor 1
nm	Nanometer
n.s.	Non-significant
o/n	Overnight
OPC	Oligodendrocyte precursor cell
OTO	Osmium thiocarbohydrazide osmium
P	Postnatal day
p	P-value
$p75^{NTR}$	Neurotrophin receptor p75
pA	Picoampere
PB	Phosphate buffer
PBS	Phosphate buffered saline
PCR	Polymerase chain reaction
PFA	Paraformaldehyde
PH	Pleckstrin homology
pH	Potential hydrogen
PI3K	Phosphoinositide 3-kinase
PIP_2	Phosphatidylinositol 4,5-bisphosphate
PIP_3	Phosphatidylinositol 3,4,5-trisphosphate
PL	Paranodal loop
pmol	Picomoles
PNS	Peripheral nervous system
Ppia	Peptidylprolyl isomerase A
PVDF	Polyvinylidene difluoride
qRT-PCR	Quantitative real time PCR
R	Arginine
RIPA	Radioimmunoprecipitation assay
RNA	Ribonucleic acid
RNA-Seq	Ribonucleic acid sequencing

rpm	Revolutions per minute
RT°C	Room temperature
SDS	Sodium dodecyl sulfate
SDS PAGE	Sodium dodecyl sulfate-polyacrylamide gel electrophoresis
sec	Seconds
SEM	Standard error of the mean
SLI	Schmidt-Lanterman incisures
SpJ	Septate-like junction
SUE	Septin unique element
TBE	Tris-borat-EDTA
TBS	Tris-buffered saline
TBST	Tris-buffered saline with Tween-20
TEMED	Tetramethylethylendiamin
tRNA	Transfer ribonucleic acid
UV	Ultraviolett
v/v	Volume per volume
V	Volt
w/v	Weight per volume
W	Tryptophan
Wt	Wild type

Protein names

Abbreviation	Protein name
ACTBL2	Actin beta-like 2
ADAM22	Metalloproteinase 22
ANLN	Anillin
APP	Amyloid precursor protein
ARPC2	Actin-related protein 2/3 complex subunit 2
ATP1A1	ATPase Na+/K+ transporting subunit alpha 1
ATP1A3	ATPase Na+/K+ transporting subunit alpha 3
CA2	Carbonic anhydrase II
CADM4	Cell adhesion molecule 4
Cas9	CRISPR associated protein 9
CASPR	Contactin associated protein 1
CASPR2	Contactin associated protein 2
CDC42	Cell division control protein 42 homolog
CLD11	Claudin 11
CNP	2'3'-cyclic nucleotide 3'phosphodiesterase
CNTN	Contactin 1
CNTN2	Contactin 2
CORO1C	Coronin-1C
EPB41L3	Erythrocyte membrane protein band 4.1 like 3
GFAP	Glial fibrillary acidic protein
GLUT1	Glucose transporter 1
GSN	Gelsolin
IBA1	Ionized calcium-binding adapter molecule 1
$K_v1.1$	Potassium voltage-gated channel subfamily A member 1
$K_v1.2$	Potassium voltage-gated channel subfamily A member 2
Kvβ2	Voltage-gated potassium channel beta 2 subunit
L-MAG	Large myelin-associated glycoprotein
MAG	Myelin associated glycoprotein
MAC3	Lysosomal-associated membrane protein 2 (LAMP2/MAC3)

MAP1A	Microtubule associated protein 1A
MAP1B	Microtubule associated protein 1B
MAP1LC3A	Microtubule associated protein 1 light chain 3 alpha
MAP6	Microtubule associated protein 6
MAPT	Microtubule associated protein tau
MBP	Myelin basic protein
MOBP	Myelin-associated oligodendrocytic basic protein
MOG	Myelin oligodendrocyte glycoprotein
$Na_v1.1$	Sodium channel, voltage-gated, type I, alpha subunit
$Na_v1.2$	Sodium channel, voltage-gated, type II, alpha subunit
$Na_v1.6$	Sodium channel, voltage gated, type VIII, alpha subunit
$Na_v1.8$	Sodium channel, voltage gated, type X, alpha subunit
$Na_v1.9$	Sodium channel, voltage gated, type XI, alpha subunit
NF	Neurofilament
NFASC	Neurofascin
NFASC155	Neurofascin-155
OMG	Oligodendrocyte-myelin glycoprotein
PLLP	Plasmolipin
PLP	Proteolipid protein
PTEN	Phosphatase and tensin homolog
RDX	Radixin
RHOA	Ras homolog gene family, member A
RHOB	Ras homolog gene family, member B
SEPT2	Septin 2
SEPT4	Septin 4
SEPT7	Septin 7
SEPT8	Septin 8
SEPT9	Septin 9
SEPT11	Septin 11
SIRT2	Sirtuin 2
TLR4	Toll-like receptor 4
TNF	Tumor necrosis factor

TPPP	Tubulin polymerization-promoting protein
TPPP3	Tubulin polymerization-promoting protein family member 3
TUBA4A	Tubulin alpha-4A
TUBB3	Tubulin beta-3
TUBB4A	Tubulin beta-4A
TUBB4B	Tubulin beta-4B
TUBB5	Tubulin beta-5
TUJ1	Class III beta-tubulin

1 Abstract

Myelination of axons facilitates rapid and precise impulse propagation in the nervous system and thus, normal motor, sensory, and cognitive capabilities. In the central nervous system (CNS), myelin is formed by oligodendrocytes, which enwrap axons with several layers of compacted membrane. The axon/myelin-unit is often impaired in myelin-related disorders and upon normal aging. However, only little is known about proteins that maintain the structure of mature myelin, many of them localized to its non-compacted sub-compartments. For example, one of the latest steps of myelin maturation in the CNS is the assembly of septin filaments, which prevent the formation of pathological myelin outfoldings. This work focusses on the analysis of *Anln*$^{fl/fl}$;*Cnp*$^{Cre/Wt}$ (*Anln* cKO) mice, which lack the cytoskeletal adaptor protein anillin (ANLN) in myelinating oligodendrocytes. To assess the role of ANLN for myelination, different biochemical and microscopic analyses have been performed. By quantitative mass spectrometry (MS) analysis of purified myelin and immunoblot validation, a specific reduction of ANLN, SEPT2, SEPT4, SEPT7, and SEPT8 has been detected in *Anln* cKO mice compared to controls. Electron micrograph analysis revealed the emergence of pathological myelin outfoldings upon conditional ANLN deletion and the observed reduction of myelin septins. Interestingly, these myelin outfoldings are a very specific neuropathology, as other analyzed neuropathological features were not observed in *Anln* cKO mice. By focused ion beam-scanning electron microscopy (FIB-SEM), it has been observed that these outfoldings are large sheets of multiple compact membrane layers, a plausible explanation for an altered membrane resistance along myelinated fiber tracts and thus, the observed reduced nerve conduction velocity. The results lead to the assumption that anillin-dependent scaffolding of mature myelin by septin filaments is required for its normal function in facilitating rapid nerve conduction in the healthy CNS.

2 Introduction

2.1 The central nervous system

The central nervous system (CNS) is classified into the brain and the spinal cord. It is essential for sensory and motor functions, which are rendered possible by signal propagation along axons. To allow fast signal propagation, evolution came up with two different strategies (Figure 1) (Rushton, 1951). First, increasing axon diameter like giant axons in some Bilateria. These giant axons are capturing a lot of space, which compete with complexity in a restricted space. To overcome this spatial problem, vertebrates secondly have evolved specialized cells that enwrap axons and thereby insulating them. The latter form of increasing nerve conduction of action potentials along the axons allows faster signal propagation, even though the axon diameter remains small (Alberts, 2002). These specialized cells are oligodendrocytes in the CNS, while in the peripheral nervous system (PNS) Schwann cells enwrap axons. Beside neurons and oligodendrocytes, the CNS consists of astrocytes and microglia, whereby oligodendrocytes, astrocytes and microglia are classified into glia cells (Kettenmann and Ransom, 2005).

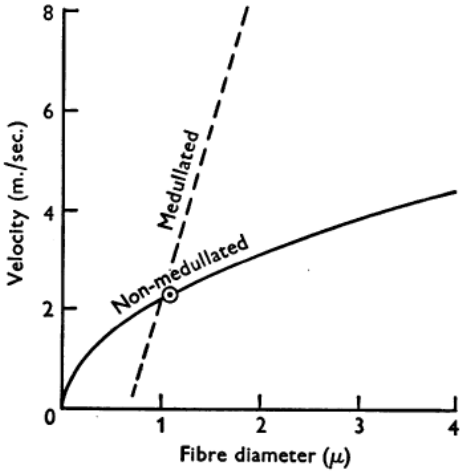

Figure 1: Theoretical relation between conduction velocity and axon diameter. Dashed line indicates the relation between conduction velocity and axon diameter for myelinated axons. The permanent line indicates the theoretical relation for non-myelinated axons. The point marks the largest c-fibers (Figure 5 from Rushton, 1951).

2.1.1 Oligodendrocytes

As described above, oligodendrocytes wrap their membrane around axons and thereby enable fast signal propagation. Oligodendrocytes are multipolar and build up multiple processes to form several myelin sheaths (Figure 3A). Between myelin sheaths, short non-myelinated segments are present, the so-called nodes of Ranvier. Myelin restricts action potentials to these non-myelinated segments and thereby provides the basis for saltatory nerve conduction (Baumann and Pham-Dinh, 2001, Kettenmann and Ransom, 2005). Myelinating glia cells constitute different compartments by enwrapping axons. The

innermost (adaxonal) and outermost (abaxonal) layer, as well as incisures and paranodal loops are classified as non-compact myelin, and are comprised of cytoplasm and cytoskeletal filaments (Arroyo and Scherer, 2000). The compact myelin is formed by multiple adhesive membrane layers (Figure 2).

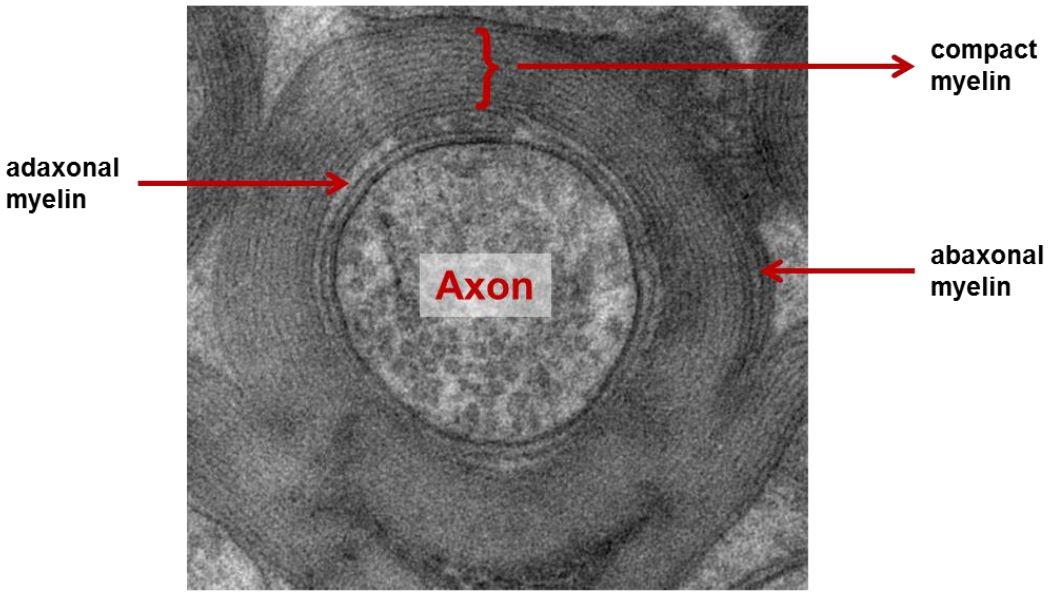

Figure 2: Illustration of compact and non-compact myelin in optic nerve cross section. Electron micrograph of a high pressure frozen optic nerve cross section, illustrates an axon and the corresponding myelin layers. Adaxonal and abaxonal myelin represent non-compact myelin. Densely packed myelin layers represent compact myelin.

The myelin sheath also leads to segmentation along the axon (Figure 3B). Each segment has a specific function and molecular composition. The node of Ranvier is a non-myelinated segment where voltage-gated sodium channels ($Na_v1.1$, $Na_v1.2$, $Na_v1.6$, $Na_v1.8$, $Na_v1.9$) are clustered (Bennett, 2013, Salzer, 2003, Zhou et al., 1998). Furthermore, subtypes of potassium channels, axonal transmembrane proteins, and axonal cytoskeletal components are found (Bennett, 2013, Berghs et al., 2000, Sherman et al., 2005). The nodes of Ranvier are flanked by paranodes. In the paranodal segment, the paranodal loops of the enwrapping oligodendrocytes are in close contact to the axon via septate-like junctions (SpJ). These junctions are build up by adhesion proteins located in the axon (contactin-associated protein (CASPR), contactin (CNTN)) and in the myelin membrane (neurofascin-155 (NFASC155)) (Einheber et al., 1997, Salzer et al., 2008). The adhesion complex is anchored to the axonal cytoskeleton via the erythrocyte membrane protein band 4.1 like 3 (EPB41L3) (Boyle et al., 2001, Gollan et al., 2002). Beside the paranode, the juxtaparanode (JXP) is located. Here, voltage-gated potassium channel subunits ($K_v1.1$, $K_v1.2$) as well as a cytoplasmic subunit (Kvβ2) are located (Rasband, 2011). The clustering of these potassium channel subunits is regulated by CASPR2 and CNTN2 (Poliak and Peles, 2003). Moreover, the complex consists of disintegrin and metalloproteinase 22 (ADAM22) (Ogawa et al., 2010). The last

segment is the internode, which is tightly enwrapped with myelin, facing the adaxonal myelin membrane.

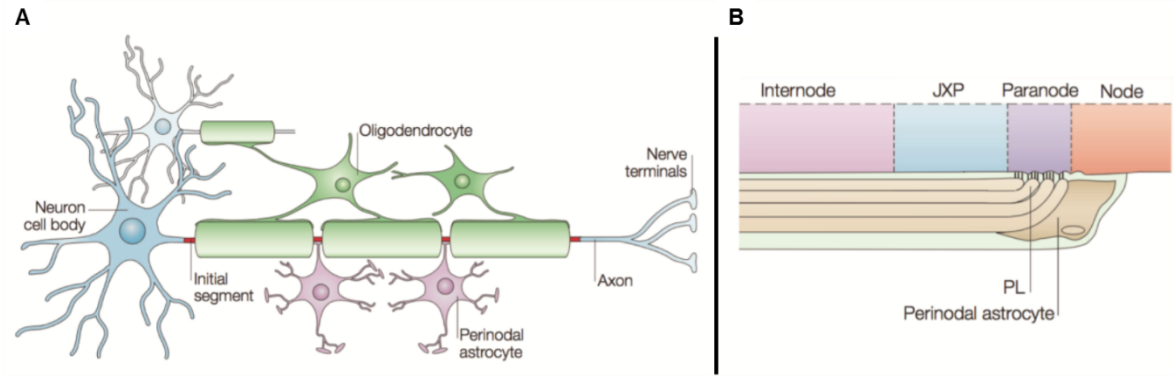

Figure 3: Structure of CNS myelinated axons. (**A**) Scheme of myelination in the central nervous system. Oligodendrocytes form multiple myelin sheaths and thereby enable salutatory signal propagation. (**B**) Scheme of the segmentation of a heminode. By myelinating an axon, the oligodendrocyte segments the axon into different parts. The node is not covered by myelin, whereas at the paranode the paranodal loops (PL) are in close contact with the axon via septate-like junctions. The juxtaparanode (JXP) is classified by a high abundance of potassium channels, whereas the internode is the largest segment covered by adaxonal myelin (modified Figure 1 from Poliak and Peles, 2003).

For a long time, it was thought that the only role of oligodendrocytes is the insulation of an axon and the accompanied saltatory nerve conduction. Nowadays, there is more and more evidence that oligodendrocytes are important for the axonal integrity by providing trophic support (Nave, 2010, Funfschilling et al., 2012, Lee et al., 2012).

2.1.2 Astrocytes

Astrocytes are the most abundant cells in the CNS and have several important functions, e.g. supplying neurons with oxygen and nutrients, store nutrients (glycogen), transport neuronal metabolites, such as CO_2, and take up neurotransmitters from the synaptic cleft (Fields and Stevens-Graham, 2002). They are indispensable for functional signal propagation, as they terminate neurotransmission and contribute to the ion homeostasis. In addition, astrocytes are interconnected via gap junctions and can communicate with each other over long distances (Kirchhoff et al., 2001). Furthermore, astrocytes are in direct contact with axons at the nodes of Ranvier and thought to have a stabilization and supply function for the nodes (perinodal astrocyte) (Black and Waxman, 1988). Astrocytes are also involved in the formation of the blood-brain barrier (BBB) by contacting blood vessels. Via the glucose transporter GLUT1, they are able to take up glucose from capillaries, and therefore are able to supply oligodendrocytes and neurons with lactate (via glycolysis) (Nave and Werner, 2014).

After CNS injury, astrocytes react to biochemical changes, leading to astrogliosis around the lesion. This defense response has the goal to minimize and repair primary damage. In

contrast to the goal of repair, astrocytes often release high levels of molecules that suppress neuron outgrowth and thereby inhibit axon regeneration (Sharma, 2015).

2.1.3 Microglia

Microglia account for ~10% of cells found within the brain. They are the main macrophages of the brain and therefore involved in, e.g. phagocytosing cell debris. Furthermore, they initiate immune responses upon for example lesions or infections. Microglia are highly mobile and scanning the environment constantly for any signs of disturbance. By detecting signs of disturbance, like cell debris or cell injury, microglia respond with repair or phagocytosis (Hanisch and Kettenmann, 2007, Nimmerjahn et al., 2005, Streit et al., 2005). In a disease state, like a lesion or infection, microglia can change into a different state, in which they can actively migrate towards the place of disturbance. In close proximity to this place, microglia induce specific responses, e.g. phagocytosis or cytokine and chemokine secretion upon detection of the relevant molecules with their various receptors (Kettenmann et al., 2011, Hanisch, 2002). Microglia support the axonal regeneration by phagocytosing cell debris and secondary release of TLR4 or TNF. If cell debris is not removed, which possibly leads to a chronic or false activation of microglia, axons get degenerated (Figure 4) (Rivest, 2009).

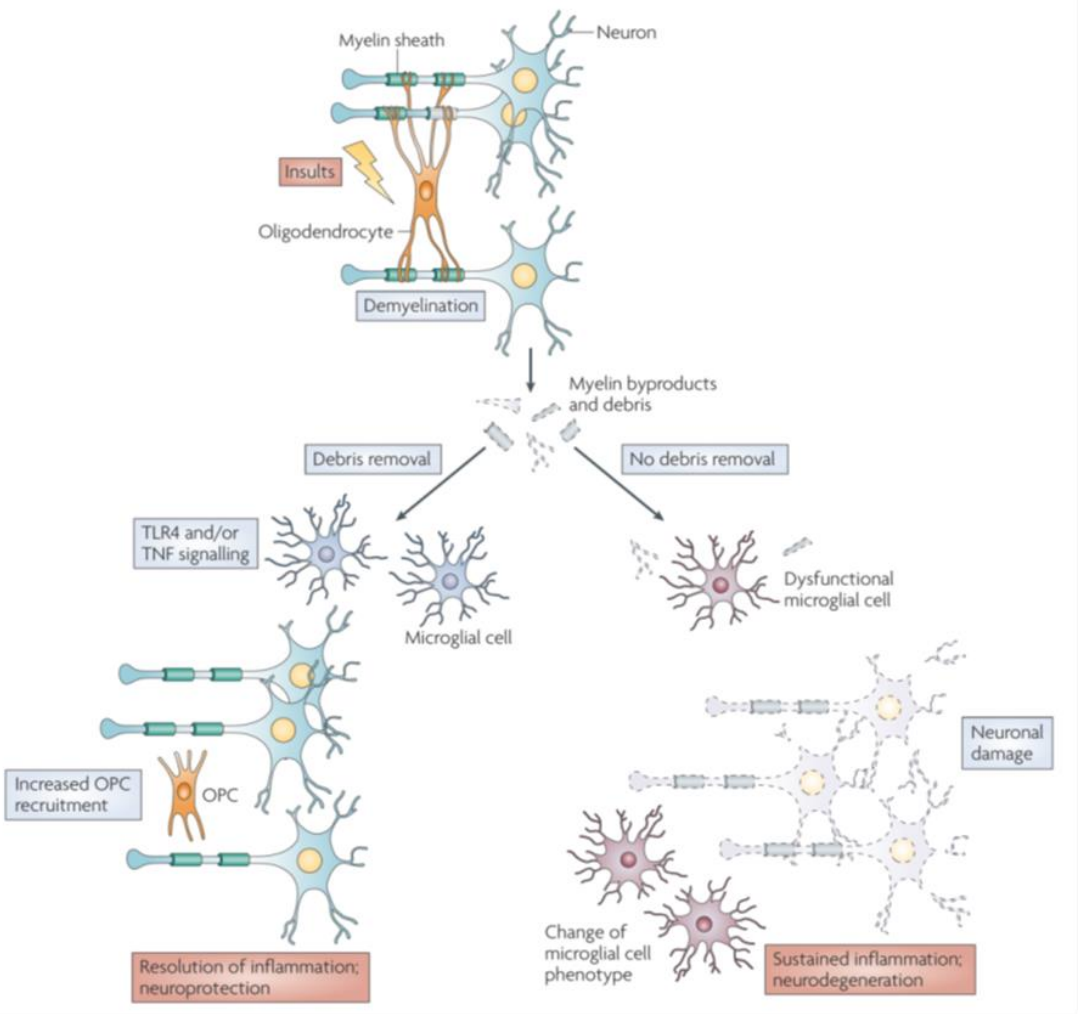

Figure 4: Neuroprotection or neurodegeneration induced by microglia. Upon demyelination, microglia are in charge of cell debris removal. By removing cell debris and releasing TLR4 or TNF, microglia act in a neuroprotective way. More oligodendrocyte precursor cells (OPCs) are recruited, which re-myelinate axons and thereby prevent axon degeneration. If microglia fail to phagocytose cell debris, neurons are damaged and further degraded, leading to neurodegeneration (Rivest, 2009) (Image taken from Rivest, 2009 (Figure 5)).

2.2 Schwann cells

Schwann cells are the glia cells of the peripheral nervous system (PNS). They are subdivided into myelinating Schwann cells and non-myelinating Schwann cells, which form Remak bundles (Figure 5). Schwann cells are important for the maintenance of axons and the survival of neurons.

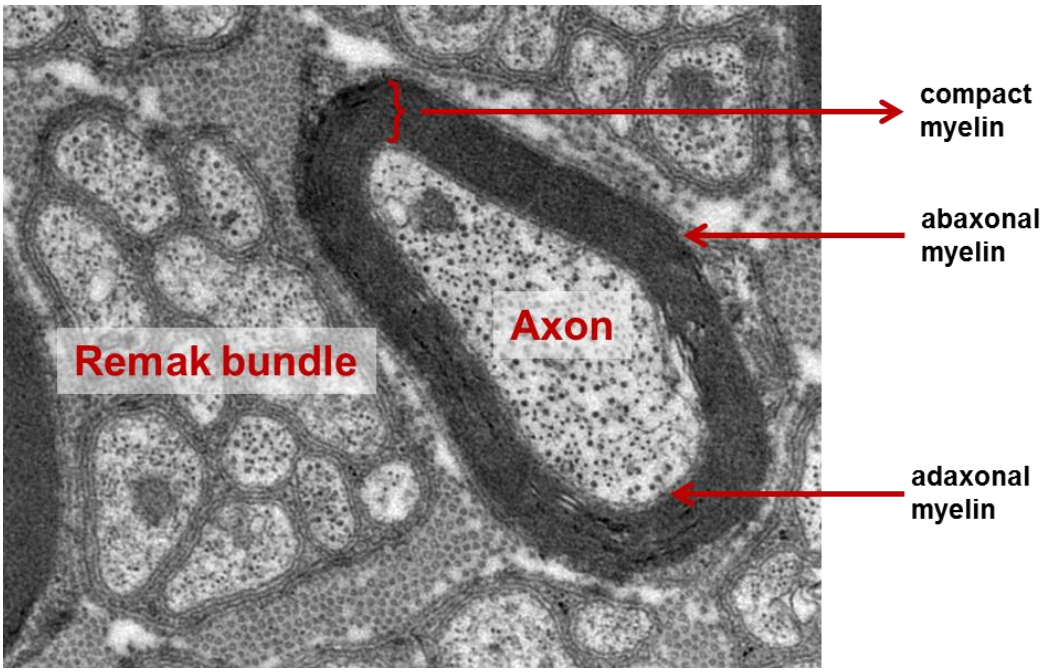

Figure 5: Schwann cell types in the PNS. Electron micrograph of a sciatic nerve cross section illustrates both types of Schwann cells. Non-myelinating Remak bundle group C fibers together and ensure that the axons are in close proximity but do not touch each other. Therefore, the cytoplasm of the non-myelinating Schwann cell surrounds the axons. Myelinating Schwann cells form myelin around the axon, exhibiting the same structures as oligodendrocytes in the CNS (compact myelin and the non-compact abaxonal and adaxonal layers).

2.2.1 Myelinating Schwann cells

In the PNS, myelinating Schwann cells form myelin around motor and sensory neurons, thereby insulating the axon and enable saltatory nerve conduction, like oligodendrocytes in the CNS. Different from oligodendrocytes, Schwann cells just form one myelin sheath (Figure 6A). The segmentation in node, paranode, juxtaparanode and internode is the same as in the CNS, including the clustering of ion channels. The node is partially in contact with microvilli of the Schwann cell and the myelinated fiber is surrounded by a basal lamina (Figure 6B).

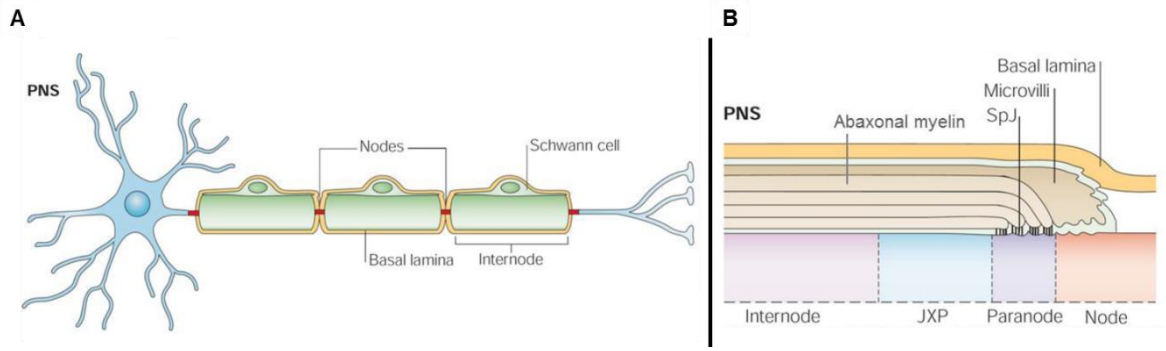

Figure 6: Structure of PNS myelinated axons. (**A**) Scheme of myelination in the peripheral nervous system. Each Schwann cell forms just one myelin sheath around an axon and thereby enable salutatory signal propagation. (**B**) Scheme of the segmentation of a heminode. By myelinating an axon, the Schwann cell segments the axon into different parts, like oligodendrocytes in the CNS. The segments are divided in node, paranode with septate-like junctions (SpJ), juxtaparanode (JXP) and the internode (modified Figure 1 from (Poliak and Peles, 2003)).

2.2.2 Remak bundle

Non-myelinating Schwann cells form so-called Remak bundles. Within these Remak bundles, several small caliber axons are grouped together. These axons are C fibers that have a very small axon diameter (<1 µm) and low conduction velocity. In a Remak bundle, axons are grouped together but are separated from each other by the cytoplasm of the non-myelinating Schwann cell. C fibers are sensory fibers and therefore often involved in neuropathic pain.

2.3 Myelin integrity and pathological myelin outfoldings

As described above, oligodendrocytes enwrap axons to form myelin. It is notable, that the myelin thickness is dependent on the axon diameter, as the ratio between the axonal diameter and the myelin diameter is constantly about 0.7 +/- 0.1 (Hildebrand and Hahn, 1978, Chomiak and Hu, 2009), suggesting an optimal signal propagation within this given ratio. There is a need for several signals that lead to the start of myelination, but also for attenuating myelination when the optimal myelin thickness is reached. For the PNS, it is known that axonal expressed neuregulin-1 regulates myelin thickness, whereas in the CNS, such a regulator has not been identified so far (Michailov et al., 2004, Brinkmann et al., 2008). However, there are different pathways known, which indeed influence myelin thickness and integrity. For example, mice that lack PTEN (phosphate and tensin homolog) from oligodendrocytes show increased myelin thickness (Goebbels et al., 2010). PTEN is a regulator of the mTOR pathway. By converting PIP_3 (Phosphatidylinositol (3,4,5)-trisphosphate) into PIP_2 (Phosphatidylinositol-4,5-bisphosphat), the PI3K induced mTOR pathway activation is antagonized (Stiles et al., 2004, Suzuki et al., 2008). Thereby, Akt gets over-activated and PIP_3 accumulates in the plasma membrane (Cantley and Neel, 1999). Additionally, in 2016 it was shown that PTEN mutant mice develop pathological myelin outfoldings (Patzig et al., 2016). Myelin outfoldings are seen in several mouse mutants and are a common neuropathological phenotype. For example, mice that lack proteins, which are highly abundant in CNS myelin, $Cnp^{null/null}$, $Mag^{null/null}$ and $Plp1^{null/null}$ mice (Patzig et al., 2016), as well as $Cdc42^{fl/fl};Cnp^{Cre/Wt}$ mice (Thurnherr et al., 2006) show pathological myelin outfoldings. In all mutants, compact myelin is formed, whereby only $Mag^{null/null}$ and $Plp1^{null/null}$ mice display alterations in myelin thickness (Patzig et al., 2016, Thurnherr et al., 2006). Interestingly, these mice show reduced levels of the cytoskeletal ANLN/septin filament, indicating the relevance of cytoskeletal stabilization of CNS myelin for myelin integrity (Patzig et al., 2016).

2.4 Anillin

Anillin (ANLN) is a conserved protein implicated in several cytoskeletal dynamics and cytokinesis. In 1989, ANLN was identified as a protein that binds F-actin in *Drosophila melanogaster* (Miller et al., 1989). It was shown that in the interphase ANLN localizes to the nucleus, while during cytokinesis it co-localizes with RhoA at the contractile ring (Field and Alberts, 1995, Piekny and Glotzer, 2008). There are further homologues of ANLN, for example, the two anillin-like proteins Boi1p and Bio2p in *Saccharomyces cerevisiae*. These proteins localize to the nucleus (Boi1p) and the contractile ring (Boi2p) and thereby are essential for cell growth and bud formation (Toya et al., 1999, Bender et al., 1996).

ANLN has several other cytoskeletal binding partners. Besides the binding of F-actin during cell division, anillin directly interacts with e.g. myosin, RhoA, microtubules and septins (Piekny and Glotzer, 2008, Straight et al., 2005, Piekny and Maddox, 2010, Versele and Thorner, 2005). The interaction with septins has been reported in different studies. In yeast, it was shown that ANLN and septins co-localize within the cleavage furrow and thereby enable proper cell division (Maddox et al., 2007, Oegema et al., 2000). *In vitro* studies have shown that anillin enhances PIP_2-mediated septin filament formation (Kinoshita et al., 2002, Liu et al., 2012). The studies indicate that septin filament formation relies on anillin, at least *in vitro* and in yeast. Interestingly, it was shown, that anillin also relies on septins. An *in vivo* study shows that in CNS myelin of mice lacking septin filaments, ANLN is also reduced (Patzig et al., 2016). These results indicate that ANLN not only promotes septin filament formation but also interacts with the filament to stabilize adaxonal myelin. Brain RNA-Seq analysis of mouse cerebral cortex show expression of ANLN in oligodendrocytes (Figure 7) (Zhang et al., 2014).

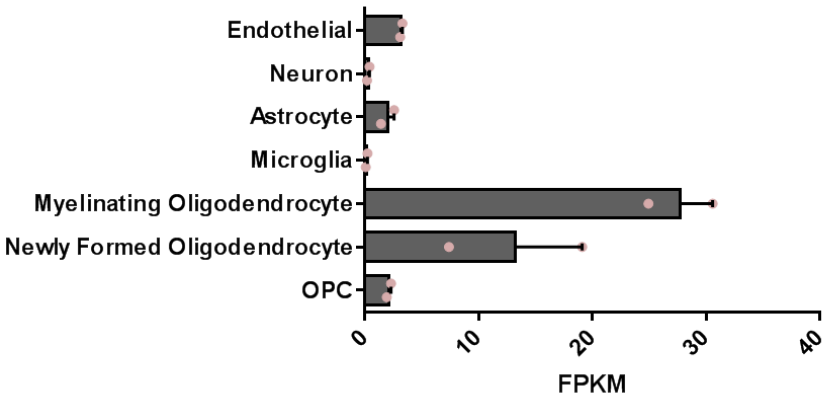

Figure 7: RNA-Seq analysis indicates *Anln* mRNA expression in oligodendrocytes. RNA-Seq analysis of cells immunopanned from mouse cerebral cortex, shows expression of *Anln* mRNA. *Anln* mRNA is detected in myelinating and newly formed oligodendrocytes. The cell-type specific abundance was extracted from Zhang et al., 2014. Mean with SEM; n=2; FPKM = fragments per kilobase of exon per million fragments mapped; OPC = oligodendrocyte precursor cell.

2.5 Septins

Septins are a family of highly conserved GTP-binding proteins, containing an N-terminal polybasic domain and a septin unique element (SUE) at the C-terminal. The proline-rich N-terminus is variable in length and the C-terminal end can contain a coiled-coil region (Cao *et al.*, 2007). In mammals, 13 septin genes are known. Most of them encode more than one polypeptide by alternative splicing and/or multiple translation start sites (Kinoshita, 2003). The mammalian septin gene family can be divided into four subgroups, which are named after the representing septins, by sequence comparison and bioinformatic analysis. SEPT1, SEPT2, SEPT4 and SEPT5 belong to the SEPT2 group, whereby every member shows two C-terminal coiled-coil domains. The SEPT6 group has five members; SEPT6, SEPT8, SEPT10, SEPT11 and SEPT14; all of them have one C-terminal coiled-coil domain. SEPT3 is the third group, consisting of SEPT3, SEPT9 and SEPT12; this group has no coiled-coil domain. The last group only consists of SEPT7 (Mostowy and Cossart, 2012, Hall and Russell, 2012, Macara et al., 2002). SEPT13 is not classified, as it was identified to be a pseudogene of SEPT7 (HGNC: 32339).

Septin monomers build up hetero-oligomers upon GTP binding and are able to assemble even further into higher order structures, like rings, meshwork or filaments (Mendoza et al., 2002, Oh and Bi, 2011). It was shown by several studies that a hetero-oligomer consists of septins out of different subgroups in a 1:1:1 ratio (Kinoshita, 2003). In an *in vitro* experiment, for example, a hetero-oligomer consisting of SEPT2, SEPT6, and SEPT7 assembled into filaments (Low and Macara, 2006, Sirajuddin et al., 2007). It was also shown that septins have various functions in cytokinesis, ciliogenesis, dendrite maturation, and sperm development (Hall and Russell, 2004, Kissel et al., 2005, Kwitny et al., 2010, Tada et al., 2007, Xie et al., 2007, Mostowy and Cossart, 2012). Septin oligomers polymerize further into a meshwork upon interaction with membrane lipids. This meshwork is comparable to an actin cytoskeleton, but it is less dynamic (Tooley et al., 2009). It was therefore suggested that septins play a role in stabilizing membranes (Tanaka-Takiguchi et al., 2009, Gilden and Krummel, 2010). Indeed, it was shown that septins stabilize the adaxonal myelin membrane and thereby prevent the formation of pathological myelin outfoldings in the CNS of mice (Patzig et al., 2016). The study also shows that SEPT2, SEPT4, SEPT7, and SEPT8 are the most abundant septins in CNS myelin. Furthermore, SEPT8 is essential to form a septin filament in CNS myelin, as the loss of SEPT8 leads to post-translational reduction of all other myelin septins (Patzig et al., 2016).

2.6 Other cytoskeletal filaments

Actin filaments are composed of globular actin (G-actin) monomers that polymerize into filamentous actin (F-actin). Within a filament, all actin monomers are orientated in the same

direction, leading to a polar actin filament. This polarization gives raise to the plus and minus end, which on the one hand sets the direction of assembly of the filament and on the other hand enables a directed movement of myosin along the actin filament (Pollard, 2017, Oda et al., 2009). Actin filaments are often found in close proximity to plasma membranes, where the build meshwork has functions in mechanical support, cell shape determination, and enables movement of the cell surface to allow e.g. cell migration or division (Cooper, 2000). Another compartment of the cytoskeleton are intermediate filaments. There are different proteins that build up intermediate filaments cell type specific, e.g. lamin (nuclear envelope), neurofilaments ((NF) neural cells) or keratin (epithelial cells) (Dechat et al., 2010, Yuan et al., 2012, Chou and Buehler, 2012). Similar to actin filaments, intermediate filaments have functions in the maintenance of the cell shape. They anchor cell organelles and thereby keep up the 3-dimensional cell shape (Herrmann et al., 2007).

In addition, microtubules are a part of the cytoskeleton. α- and β-tubulin dimers build up protofilaments, which associate laterally into a microtubule. Like actin filaments, microtubules have a plus and a minus end, arising from the filament formation, as the β-subunit of the tubulin dimer always contacts the α-subunit of the next dimer. Therefore, at the plus end the β-subunits are exposed, whereas at the minus end the α-subunits are exposed. Microtubules can extend at both, plus and minus ends to elongate (Walker et al., 1988). Microtubules have important functions in e.g. the mitotic spindle or intracellular transport. The intracellular transport is associated with the motor proteins kinesin and dynein, which transport for example mitochondria along microtubules (Hirokawa and Takemura, 2005, Vale, 2003).

2.7 Axon caliber

Beside myelination, the axon diameter influences the signal propagation along axons, as the transverse resistance of an axon decreases with increasing caliber (Hartline and Colman, 2007, Seidl, 2014). For the CNS and PNS, different mechanisms, by which the axonal diameter is regulated, have been identified. For example, in the PNS it was shown that the phosphorylation state of the neurofilaments NF-medium and NF-heavy plays an important role in axonal diameter regulation (Garcia et al., 2003). Interestingly, the phosphorylation state of neurofilaments is regulated by Schwann cells in an “outside-in” fashion via the interaction of myelin associated glycoprotein (MAG) with e.g. the receptor p75NTR on the axon (de Waegh et al., 1992, Yin et al., 1998, Garcia et al., 2003, Wang et al., 2002). Furthermore, in the CNS the multimeric Nogo receptor 1 (NgR1) was identified as an axonal interaction partner of MAG *in vitro* using a soluble form of MAG (Palandri et al., 2015). It has been shown that mice deficient for Nogo1 (*Ngr1*$^{-/-}$) showed reduced

neuronal somata *in vitro* as well as decreased axonal diameter in the optic nerve and the spinal cord *in vivo* (Palandri et al., 2015, Lee et al., 2017).

Furthermore, axonal intrinsic mechanisms regulating the axon diameter include α-adducin and PTEN. It has been shown that the loss of α-adducin, an actin binding protein that stabilizes actin rings along the axon, show a progressive enlargement of axon diameter (Leite et al., 2016). Moreover, mice that conditionally lack PTEN in cerebellar granule cells, showed increased neuronal diameter of these specific neuron population in the cortex (Goebbels et al., 2017).

2.8 Aim of the study

Deletion of the *Sept8* gene in mature oligodendrocytes prevents the assembly of myelin septin filaments; notably, when myelin septin filaments are absent the abundance of ANLN in myelin is also diminished (Patzig et al., 2016). This implies that the association with myelin septin filaments prevents rapid turnover and degradation of ANLN. Here, the hypothesis is to be tested that oligodendroglial ANLN, beyond its mere association with myelin septins, may serve a crucial function in myelin septin filament assembly. To do so, a novel line of $Anln^{fl/fl};Cnp^{Cre/Wt}$ (*Anln* cKO) mouse mutants is to be analyzed, in which mature oligodendrocytes do not express ANLN. The loss of ANLN and its effect on myelin septin assembly, as well as related myelin pathology is to be analyzed. For understanding the possible relevance of ANLN for septin filament assembly in CNS myelin, immunohistochemistry is to be used to test for co-localization of ANLN and septins in Wt mice. Additionally, it is to be tested if a developmental dependence of ANLN and septins can be identify. To test the functional relevance of ANLN for myelin septins, ANLN is to be deleted in mature oligodendrocytes of mice, using Cre recombinase under control of the *Cnp* promotor ($Cnp^{Cre/Wt}$ (Lappe-Siefke et al., 2003)). The abundance of ANLN and septins is to be analyzed using quantitative mass spectrometry, as well as immunoblot validation. Thereby, an unbiased identification of other effected proteins is possible. As the loss of septins is directly related to structural changes in myelin, possible myelin abnormalities upon the absence of ANLN, are to be analyzed. Furthermore, axonal changes upon ANLN-absence are to be analyzed. As oligodendrocytes are reported to support axonal integrity (Klugmann et al., 1997, Griffiths et al., 1998), secondary pathologies like axonopathy and gliosis are to be analyzed in $Anln^{fl/fl};Cnp^{Cre/Wt}$ mouse brains by immunohistochemistry. It is of interest, to 3D reconstruct possible myelin abnormalities, such as myelin outfoldings, using focused ion beam scanning electron microscopy (FIB SEM), to get a better understanding of the size and dimension of such abnormalities.

3 Materials and Methods

3.1 Materials

3.1.1 General material

General laboratory materials were purchased from BD Falcon (Heidelberg, Germany), Bio-Rad (Munich, Germany), Gilson (Limburg-Offheim, Germany), Brand (Radebeul, Germany), Sarstedt (Nümbrecht, Germany) and Eppendorf (Hamburg, Germany). All chemicals used, were obtained from Sigma-Aldrich GmbH (Munich, Germany), Merck KGaA (Darmstadt, Germany) and SERVA (Heidelberg, Germany).

3.1.2 Kits

All kits were used according to the manufacturer instructions, unless otherwise stated.

Description	Manufacturer
RNA purification ‘RNeasy mini prep’	Qiagen (Portland, USA)
DC Protein Assay (Lowry)	Bio-Rad (Munich, Germany)
DAB Zytomed Kit	Zytomed Systems GmbH (Berlin, Germany)
LSAB2 Kit	Dako (Hamburg, Germany)
Vector Elite ABC Kit	Vector Labs (Loerrach, Germany)
Agilent RNA 6000 Nano KIT	Agilent Technologies (Santa Clara, California, United States)

3.1.3 Materials for genotyping

Description	Content	
Modified Gitschier buffer (MGB)	Tris/HCl, pH 8.8	67 mM
	$(NH_4)_2SO_4$	16.6 mM
	$MgCl_2$	6.5 mM
	Triton X-100	0.5 % [v/v]
Tris-borat-EDTA (TBE) buffer	Tris Base	40 mM
	Boric acid	20 mM
	EDTA	1 mM

10 mM dNTP (50x stock)	dATP	2.5 mM
	dCTP	2.5 mM
	cGTP	2.5 mM
	cTTP	2.5 mM
	200 µM final concentration in a PCR reaction (50 µM each nucleotide)	

Description	Manufacturer
Proteinase K	Boehringer GmbH (Mannheim, Germany)
GoTaq DNA polymerase	Promega (Mannheim, Germany)
GoTaq buffer 5x	Promega (Mannheim, Germany)
Superscript III-reverse transcriptase	Invitrogen (Karlsruhe, Germany)
dNTPs	Boehringer GmbH (Mannheim, Germany)
GeneRuler 100 bp DNA ladder	Thermo Fisher Scientific (St. Leon-Rot, Germany)

3.1.4 Genotyping primers

Description	Number	Sequence
Anln genotyping	29823	5‘- GACATAGCCCTCAGTGTTCAGG -3‘
	29824	5‘- GAATCCTGCATGGACAGACAG -3‘
	32002	5'- GAGCTCAGACCATAACTTCG -3'
Sept8 genotyping	16458	5’- CAGGCAGATGTATATGCAGCAG -3’
	16459	5’- GGTGGCTTTGAACTTGCTATCC -3’
	16460	5’- GAAGCAGCCATAGAGGAGATCC -3’
Cre recombinase genotyping	2016	5'- GCCTTCAAACTGTCCATCTC -3'
	7315	5'- CCCAGCCCTTTTATTACCAC -3'
	4192	5'- CAGGGTGTTATAAGCAATCCC -3'
	4193	5'- CCTGGAAAATGCTTCTGTCCG -3'
Mbp genotyping	30833	5'- GAGCTCTGGTCTTTTCTTGCAG -3'
	30834	5'- CCCGTGGTAGGAATATTACATTAC -3'
	30835	5'- CAGGGGATGGGGAGTCAG -3'
	1879	5'- ATGTATGTGTGTGTGTGCTTATCTAGTGTA -3'

Sept9 genotyping	23844	5'- GACCATGCATGCACTCAGCCACAG -3'
	23845	5'- CAGAACTGAAATCCCCTACAGTAG -3'
	23846	5'- GCTCAGACAACGATATTTGGG -3'
Dhh Cre recombinase genotyping	10967	5’- CCTGCGGAGATGCCCAATTG -3’
	15793	5’- CAGCCCGGACCGACGATGAA -3’

3.1.5 Quantitative real-time PCR primers

Gene	Direction	Sequence
Anln	Forward	5’- ACAATCCAAG GACAAACTTGC -3'
	Reverse	5’- GCGTTCCAGG AAAGGCTTA -3'
Cnp	Forward	5‘- CGCTGGGGCAGAAGAATA -3'
	Reverse	5‘- AAGGCCTTGCCATACGATCT -3'
Sept2	Forward	5‘- TCCTGACTGA TCTCTACCCAGAA -3'
	Reverse	5‘- AAGCCTCTAT CTGGACAGTTCTTT -3'
Sept4	Forward	5‘- ACTGACTTGT ACCGGGATCG -3'
	Reverse	5‘- TCTCCACGGT TTGCATGAT -3'
Sept7	Forward	5‘- AGAGGAAGGC AGTATCCTTGG -3'
	Reverse	5‘- TTTCAAGTCC TGCATATGTGTTC -3'
Sept8	Forward	5‘- CTGAGCCCCG GAGCCTGT -3'
	Reverse	5‘- CAATCCCAGT TTCGCCCACA -3'
Sept9	Forward	5'- GACTCCATCCTGGAGCAGAT -3'
	Reverse	5'- TTTGGACTTGAAGAGGGTATTGA -3'
Sept11	Forward	5'- GCTATGAACTCCAGGAAAGCA -3'
	Reverse	5'- GGGCGTCAATGTATTCCACT -3'
Cdc42	Forward	5'- GCTGTCAAGTATGTGGAGTGCT -3'
	Reverse	5'- GGCTCTTCTTCGGTTCTGG -3'
RhoB	Forward	5‘- CAGACTGCCTGACATCTGCT -3'
	Reverse	5‘- GTGCCCACGCTAATTCTCAG -3'
Ppia	Forward	5‘- CACAAACGGT TCCCAGTTTT -3'
	Reverse	5‘- TTCCCAAAGA CCACATGCTT -3'

3.1.6 Protein biochemistry

Description	Content	
10x Phosphate-buffered saline (PBS)	NaCl	1.7 M
	KCl	34 mM
	Na_2HPO_4 x $2H_2O$	40 mM
	K_2HPO_4	18 mM
		pH 7.2 with 1N NaOH
10x Tris-buffered saline (TBS) (for myelin purification)	Tris/HCl, pH 7.4	200 mM
	NaCl	1370 M
Modified RIPA buffer	TBS (10x for myelin purification)	1x
	EDTA	1 mM
	Sodium deoxycholate	0.5% [w/v]
	Triton X-100	1.0% [v/v]
	Protease inhibitor	1 tablet/10 ml

Description	Manufacturer
Complete Mini protease inhibitor	(Roche Diagnostics GmbH, Mannheim, Germany)

3.1.7 SDS PAGE and immunoblot

Description	Content	
SDS separating gel	Acrylamid/Bisacrylamid 29:1	15%, 12% or 10% [v/v]
	Tris/HCl pH 8.8	0.4 M
	SDS	0.1% [w/v]
	APS	0.03% [w/v]
	TEMED	0.08% [v/v]
SDS stacking gel	Acrylamid/Bisacrylamid 29:1	4% [v/v]
	Tris/HCl pH 8.8	125 mM
	APS	0.05% [w/v]
	TEMED	0.1% [v/v]
4x SDS sample buffer	Glycerol	40% [v/v]
	Tris/HCl pH 6.8	240 mM
	SDS	8% [w/v]
	Bromphenol blue	0.04% [w/v]

10x SDS running buffer (Laemmli buffer)	Tris base Glycine SDS	250 mM 1.92 mM 1% [w/v]
Transfer buffer (semi-dry blot)	Tris base Glycine Methanol SDS	96 mM 78 mM 10% [v/v] 0.03% [w/v]
Transfer buffer (wet-tank blot)	Tris base Glycine Methanol	96 mM 78 mM 20% [v/v]
20x Tris buffered saline (TBS)	Tris/HCl, pH 7.4 NaCl	1 M 3 M
1x TBS with Tween-20 (TBST)	Tris/HCl, pH 7.5 NaCl Tween-20	50 mM 150 mM 0.05% [v/v]
Immunoblot stripping buffer	Glycine/HCl, pH 2.5 Tween-20	0.2 M 0.1% [v/v]
Immunoblot blocking buffer	Non-fat dry milk powder	5% [w/v] in TBST

Description	Manufacturer
Western Lightning® Plus-ECL	Perkin Elmer Life Sciences, Inc. (Rodgau, Germany)
WesternBright Chemiluminescence Substrat Sirius	Biozym Scientific GmbH (Hess. Oldendorf, Germany)
PageRuler™ Plus Prestained Protein Ladder	Thermo Fisher Scientific (St. Leon-Rot, Germany)
PVDF Membrane Amersham Hybond P0.45 µm	GE Healthcare Life Science (Buckinghamshire, UK)
PVDF Membrane Imobilon®-FL P0.45 µm	Merck Millipore Ltd. (Darmstadt, Germany)

3.1.8 Primary antibodies - Immunoblot

Antibody	Dilution	Load	% Gel	Species	Source
ANLN	1:500	30 µg	10%	Polyclonal goat	Acris
SEPT2	1:2000	5 µg	10 or 12%	Polyclonal rabbit	PtG
SEPT4	1:100	30 µg	10 or 12%	Polyclonal rabbit	IBL
SEPT7	1:5000	3 µg	10 or 12%	Polyclonal rabbit	IBL
SEPT8	1:2500	5 µg	10 or 12%	Polyclonal rabbit	PtG
SEPT9	1:1000	30 µg	10 or 12%	Polyclonal rabbit	PtG
SEPT11	1:5000	5 µg	10 or 12%	Polyclonal rabbit	W.S.Trimble (Tsang et al., 2011)
L-MAG	1:500	5-10 µg	8%	Polyclonal rabbit	N. Schaeren-Wiemers (Miescher et al., 1997)
MOG	1:500	5 µg	12%	Monoclonal mouse	C. Linington (Linnington et al., 1984)
TUJ1	1:1000	5-10 µg	10 or 12%	Monoclonal mouse	Covance
ATP1A1	1:2000	5 µg	10 or 12%	Monoclonal mouse	Abcam
ATP1A3	1:1000	5 µg	10 or 12%	Monoclonal mouse	Abcam
CNP	1:500	5 µg	10 or 12%	Monoclonal mouse	Sigma

PLP/DM20	1:500	0.5 µg	15%	Polyclonal rabbit	K.-A. Nave (Jung et al., 1996)
SIRT2	1:500	10 µg	10 or 12%	Polyclonal rabbit	Abcam
CD9	1:250	0.5 µg	15%	Monoclonal mouse	BD Biosciences
MAG (513)	1:1000	0.5 µg	15%	Monoclonal mouse	Chemicon
Actin	1:2000	5 µg	10 or 12%	Monoclonal mouse	Millipore

3.1.9 Secondary antibodies - Immunoblot

Antibody	Dilution	Species	Source
anti-rabbit-HRP	1:10000	Goat	Dianova
anti-mouse-HRP	1:10000	Goat	Dianova
anti-goat-HRP	1:1000	Donkey	Dianova

3.1.10 Solutions for fixation

Description	Content	
Avertin	2,2,2 Tribromethanol 99% Amylalcohol Mixed at 40 °C for 30 min while stirring and subsequently filtered Stored at -20°C	2% [w/v] 2% [v/v]
16% Paraformaldehyde (PFA)	PFA NaOH PFA cooked at 65 °C for 20 min while stirring, NaOH droplets until solution was cleared and then filtered	16% [w/v] 5 N

0.2 M Phosphate buffer	Sodiumdihydrogenphosphate	0.36% [w/v]
	di-Sodiumhydrogenphosphate	3.1% [w/v]
	NaCl	1% [w/v]
4% Paraformaldehyde (PFA)	PFA	4% [w/v]
	Phosphate buffer	0.1 M
Karlsson-Schultz fixative (K&S)	PFA	4% [w/v]
	Glutaraldehyde	2.5% [v/v]
	Phosphate buffer	0.1 M

3.1.11 Immunohistochemistry and staining solutions

Description	Content	
Citrate buffer (0.01 M, pH 6.0)	Citric acid	1.8 mM
	Sodium citrate	8.2 mM
Tris buffer (0.05 M, pH 7.6)	Tris/HCl, pH 7.6	50 mM
	Sodium chloride	0.9% [w/v]
Phosphate buffer (0.2 M, pH 7.4)	Sodiumdihydrogenphosphate	0.04 M
	di-Sodiumhydrogenphosphate	0.16 M
PBS/BSA	Sodiumdihydrogenphosphate	0.04 M
	di-Sodiumhydrogenphosphate	0.16 M
	NaCl	1.8% [w/v]
	Bovine serum albumin (BSA)	1.0% [w/v]
Scott`s solution	Potassiumhydrogencarbonate	0.2% [w/v]
	Magnesium sulphate	2% [w/v]
HCl - alcohol	HCl	0.09% [v/v]
	Ethanol	70% [v/v]
Mayer’s haematoxylin solution	Haematoxylin	0.1% [w/v]
	Sodium iodate	0.02% [w/v]
	Potassium aluminum sulfate	5% [w/v]
	Added under constant shaking, solution turned violet	
	Chloralhydrate	5% [w/v]
	Citric acid	0.1% [w/v]

Blocking buffer (cryosections)	Goat serum or horse serum	10% [v/v]
	Triton X-100	0.5% [v/v]
	Dissolved in BSA/PBS	
Blocking buffer (teased fibers)	Horse serum	10% [v/v]
	Tween-20	0.1% [v/v]
	Dissolved in 1x PBS	
Gallyas incubation solution	Ammonium nitrate	0.1% [w/v]
	Silver nitrate	0.1% [w/v]
	Sodium hydroxide (pH 7.5)	12‰ [w/v]
	Brown precipitate dissolved by shaking	
Gallyas physical developer A	Sodium carbonate (dehydrated)	5% [w/v]
Gallyas physical developer B	Ammonium nitrate	0.2% [w/v]
	Silver nitrate	0.2% [w/v]
	Wolframosilicic acid (silicotungstic acid)	1% [w/v]
Gallyas physical developer C	Ammonium nitrate	0.2% [w/v]
	Silver nitrate	0.2% [w/v]
	Wolframosilicic acid (silicotungstic acid)	1% [w/v]
	PFA	0.26% [w/v]
Gallyas fixing solution	Sodium thiosulphate	2% [w/v]

Description	Manufacturer
Eukitt	Kindler (Freiburg, Germany)
Aqua-Poly/Mount	Polysciences (Eppelheim, Germany)
Fluoromount-G™	Invitrogen (Karlsruhe, Germany)

3.1.12 Primary antibodies - Immunohistochemistry

Antibody	Dilution	Species	Source
ANLN	1:200	Polyclonal goat	Acris
SEPT7	1:1000	Polyclonal rabbit	IBL
SEPT8	1:500	Polyclonal rabbit	PtG
MAG (513)	1:50	Monoclonal mouse	Chemicon
βIII-Tubulin (TUJ1)	1:1000	Monoclonal mouse	Covance
NF	1:1000	Monoclonal mouse	Covance
CASPR	1:500	Monoclonal mouse	Neuromabs
$Na_v1.6$	1:500	Polyclonal rabbit	Almonelabs

3.1.13 Secondary antibodies - Immunohistochemistry

Antibody	Dilution	Species	Source
anti-mouse-Alexa 488	1:1000	Donkey	Dianova
anti-rabbit-Alexa 488	1:1000	Donkey	Dianova
anti-mouse-Alexa 555	1:1000	Donkey	Dianova
anti-rabbit-Alexa 555	1:1000	Donkey	Dianova
anti-goat-Cy3	1:500	Donkey	Dianova
anti-mouse-Dyelight633	1:500	Donkey	Dianova

3.1.14 Electron microscopy

Description	Content	
Epon	Glycidether 100	171.3 g
	Dodecenyl succinic anhydride (DDSA)	115 g
	Methyl nadic anhydride (MNA)	89 g
	Mixed using magnet stirrer for 10 min	
	DMP-30	6.5 ml
	Mixed using magnet stirrer for 20 min	
Methylene blue	Na-tetraborat (Borax)	1% [w/v]
	Methylenblau	1% [w/v]
Azure II	Azure II	1% [w/v]
Methylene blue - Azure II staining solution	Methylene blue	50% [v/v]
	Azure II	50% [v/v]
	Freshly mixed before use	

3.1.15 Solutions for silver impregnation of protein gels

Description	Content	
Fixation solution	Ethanol	40% [v/v]
	Acidic acid	10% [v/v]
Sensitization solution	$Na_2S_2O_3$	0.8 mM
Staining solution	$AgNO_3$	0.2% [w/v]
	HCOH	0.02% [v/v]
Developing solution	Na_2CO_3	3% [w/v]
	HCOH	0.02% [v/v]
Stop solution	Acidic acid	5% [v/v]

3.1.16 Mouse lines

Anln$^{fl/fl}$ mice	(ES cells from EUCOMM, Erwig et al., unpublished)
Sept8$^{fl/fl}$ mice	(Patzig et al., 2016)
Sept8$^{null/null}$ mice	(Patzig et al., 2016)
Cnp$^{Cre/Wt}$ mice	(Lappe-Siefke et al., 2003)
Sept9$^{R88W/Wt}$ mice	(CRISPR, F. Benseler; DNA core facility (MPI EM, Göttingen), U. Fünfschilling; transgenic service (MPI EM, Göttingen))
Sept2$^{fl/fl}$ mice	(ES cells from EUCOMM, unpublished)
Sept9$^{fl/fl}$ mice	(Fuchtbauer et al., 2011)
Dhh Cre+ mice	(Jaegle et al., 2003)

3.2 Methods

3.2.1 Animals

All animals used in the experiments were bred and kept in the mouse facility of the Max-Planck-Institute of Experimental Medicine (MPI EM). All mice were sacrificed by cervical dislocation or by perfusion using anesthetics. All experiments were performed in accordance with the German animal welfare law.

3.2.2 Generation of *Anln* conditional knockout mice (*Anln* cKO)

To generate ANLN conditional knockout mice (*Anln* cKO), embryonic stem (ES) cells harboring a modified allele of the *Anln* gene were obtained from the European Conditional Mouse Mutagenesis Program (EUCOMM). ES cells were injected into FVB blastula derived from C57BL/6N mice and implanted into pseudo-pregnant foster mothers (Animal facility, MPI EM). Positive chimaeras of the ES cell clone EPD0545_1_F09 were bred to wild type C57BL/6N mice gaining F1 offspring. *Anln-LacZ* animals were identified by genotyping polymerase chain reaction (PCR) and further bred to the Flp-recombinase positive mouse line to remove the LacZ/neo cassette resulting in floxed mice for conditional gene targeting. Homozygous *Anln* floxed mice ($Anln^{fl/fl}$) together with heterozygous *Cnp* mice ($Cnp^{Cre/Wt}$) (Lappe-Siefke et al., 2003) were used to delete *in vivo* exon 4 of the *Anln* gene in oligodendrocytes and Schwann cells specifically. The generation of *Anln* cKO mice were performed by Ramona Jung (MPI EM) and the animal facility around Ursula Fünfschilling (MPI EM; transgenic service).

3.2.3 Generation of $Sept9^{R88W/Wt}$ mice

For the generation of $Sept9^{R88W/Wt}$ mice, the CRISPR/Cas9 system was used. It was decided to induce a point mutation at the Arginine 88 into a Tryptophan, thereby mimicking a frequent mutation in human hereditary neuralgic amyotrophy (HNA). The implementation of the point mutation using the CRISPR/Cas9 system was achieved by F.Benseler and his group (MPI EM; DAN core facility) and the animal facility around Ursula Fünfschilling (MPI EM; transgenic service).

3.2.4 Genotyping PCR

For genotyping, small tail tips or ear punches of P21 young mice were used. They were digested in 180 µl 1x MGB with 20 µl Proteinase K at 55°C with a agitation of about 1250 rpm for 2 h. Afterwards, the Proteinase K was inactivated by incubation of the tails at 95°C for 10 min. Amplification of genotype specific DNA fragments was performed using the polymerase chain reaction (PCR) (Mullis et al., 1986, Saiki et al., 1988). For this purpose, 20 µl PCR reaction-mix was added to 1 ml DNA. The PCRs were run in a T3 or

Gradient Thermocycler (Biometra GmbH, Göttingen, Germany). Primers were selected manually using the DNASTAR Lasergene 9 core suite and then synthesized in house by the service facility of the MPI EM. To separate the PCR products, gels containing 2% [w/v] agarose in TBE buffer, were used. Before loading 20 µl of the PCR samples, 5 µl of Gel Red Nucleic Acid Stain (BioTrend (Cologne, Germany); 1:2500 in ddH_2O) was added for DNA visualization to each sample. The samples were separated at 120 V for 60 min in TBE buffer. GeneRuler 100 bp DNA ladder (Thermo Fisher Scientific, St. Leon-Rot, Germany) was used as a marker. For documentation pictures were obtained with an Intas UV system (Intas Science Imaging, Göttingen, Germany). Genotyping of *Sept9*$^{R88W/Wt}$ mice, was performed by the sequencing facility of F.Benseler (MPI EM; DNA core facility).

PCR reaction *Anln* gene

ddH_2O	12.2 µl
GoTaq buffer (5x)	4.2 µl
dNTP (2 mM)	2.1 µl
Primer 29823 (10 µM)	0.5 µl
Primer 29824 (10 µM)	0.5 µl
Primer 32002 (10 µM)	0.5 µl
GoTaq DNA polymerase	0.07 µl

Wt ~ 570 bp; Flox ~ 780 bp; Rec ~ 270 bp

PCR reaction *Sept8* gene

ddH_2O	12.4 µl
GoTaq buffer (5x)	4.2 µl
dNTP (2 mM)	2.1 µl
Primer 16458 (10 µM)	0.1 µl
Primer 16459 (10 µM)	0.6 µl
Primer 16460 (10 µM)	0.6 µl
GoTaq DNA polymerase	0.07 µl

Wt ~ 450 bp; Flox ~ 550 bp; Rec ~ 260 bp)

PCR reaction *Cnp* gene

ddH_2O	11.3 µl
GoTaq buffer (5x)	4.2 µl
dNTP (2 mM)	2.1 µl
Primer 4192 (10 µM)	0.2 µl
Primer 4193 (10 µM)	0.2 µl
Primer 2016 (10 µM)	1 µl
Primer 7315 (10 µM)	1 µl
GoTaq DNA polymerase	0.07 µl

Wt ~ 700 bp; Cre+ ~ 450 bp

PCR reaction *Sept9* gene

ddH_2O	11.9 µl
GoTaq buffer (5x)	4.2 µl
dNTP (2 mM)	2.1 µl
Primer 23844 (10 µM)	1 µl
Primer 23845 (10 µM)	0.2 µl
Primer 23846 (10 µM)	0.6 µl
GoTaq DNA polymerase	0.07 µl

Wt ~ 520 bp; Flox ~ 600 bp; Rec ~ 650 bp

PCR reaction *Dhh* Cre

ddH_2O	12.7 µl
GoTaq buffer (5x)	4.2 µl
dNTP (2 mM)	2.1 µl
Primer 10967 (10 µM)	0.5 µl
Primer 15793 (10 µM)	0.5 µl
GoTaq DNA polymerase	0.07 µl

Dhh Cre+ ~ 300 bp

PCR reaction *Mbp* gene	
ddH_2O	12.5 µl
GoTaq buffer (5x)	4.2 µl
dNTP (2 mM)	2.1 µl
Primer 1879 (10 µM)	0.4 µl
Primer 30833 (10 µM)	0.4 µl
Primer 30834 (10 µM)	0.2 µl
Primer 30835 (10 µM)	0.2 µl
GoTaq DNA polymerase	0.07 µl

Wt ~ 170 bp; Mbp- ~ 380 bp

3.2.5 RNA isolation and analysis

For RNA isolation and subsequent analysis the corpus callosum of n=6 mice (male and female, 4 mo of age) was collected. The corpus callosum was dissected using a brain slicer. From each brain section the corpus callosum was collected manually. The collected tissue was directly incubated in RNA*later*™ solution (Ambion®, Thermo Fisher Scientific, St. Leon-Rot, Germany), at 4°C o/n and then stored at -20°C until usage. RNA isolation, cDNA synthesis, and qRT-PCR were done by Ursula Kutzke.

3.2.5.1 RNA isolation

Small scale RNA isolation from separated corpus callosum of male mice was performed using Qiagen's "RNeasy Mini Prep" kit. The kit is based on a selective binding of RNAs bigger than 200 bases to a silica-gel based membrane under high-salt conditions, which excludes binding of 5 S, 5.8 S and tRNAs. RNA isolation and purification was carried out following the manufacturer's instructions. The tissue was homogenized in Trizol (Life Technologies™, Thermo Fisher Scientific, St. Leon-Rot, Germany), followed by chloroform extraction (200 µl chloroform was added to 0.6 ml homogenate). After 15 min of centrifugation at 16000 x *g* (Heraeus Biofuge Pico table centrifuge, 13000 rpm) the upper aqueous phase was transferred to a new 2 ml tube. One volume of ethanol was added to the samples. Then the samples were mixed and applied to RNeasy columns. After 1 min centrifugation at 16000 x *g* the columns were washed one time with the RW1 buffer and two times with the RPE buffer. RNA was eluted with 50 µl of RNase-free ddH_2O. The quality of RNA was tested using the Agilent RNA 6000 Nano KIT and the Agilent 2100 Bioanalyzer

(Agilent Technologies, Santa Clara, California, United States), following the company's instructions. The amount of RNA was measured using the NanoDrop 2000 Spectrophotometer (Thermo Fisher Scientific, St. Leon-Rot, Germany) and the RNA concentration for all samples was adjusted to 100 ng/µl.

3.2.5.2 cDNA synthesis

As a next step, the isolated RNA was transcribed into a complementary single stranded DNA (cDNA) in a reverse transcription reaction catalyzed by RNA dependent DNA polymerase SuperScript III (Invitrogen, Karlsruhe, Germany).

cDNA synthesis protocol

8 µl	RNA (800 ng total)
2 µl	dT mix Primer (0.6 pmol/µl)
2 µl	N9 (random nonamers 120 pmol/µl)

To denaturate RNA and primers, the mixture was incubated for 10 min at 70ºC and 1 min on ice.

Add following premix to the reaction:

4 µl	5x first strand buffer
1 µl	dNTP (10 mM)
2 µl	DDT (100 mM)
1 µl	SuperScript III reverse transcriptase (200 U/µl)

Incubation in thermocycler with the following settings:

25°C	10 min
50°C	45 min
55°C	45 min

Synthesized cDNA was diluted 1:30 with ddH_2O and stored at -20°C.

3.2.5.3 Quantitative real-time PCR (qRT-PCR)

The pipetting robot epMotion 5075 (Eppendorf, Hamburg, Germany) was used for pipetting. qRT-PCR was performed using the Power SYBR Green PCR Master Mix (Promega, Fitchburg, Wisconsin, United States) and the Light Cycler 480II (Roche Diagnostics GmbH, Mannheim, Germany).

Mixture for gene expression analysis

2 µl	cDNA (2 ng/µl)
5 µl	SYBR Green PCR Master Mix
0.1 µl	Forward primer
0.1 µl	Reverse primer
2.8 µl	ddH_2O

All reactions were performed in quadruplicates.

Program for 50 cycles

15 sec	95°C
1 min	60°C

mRNA abundance was analyzed in relation to the mean of the standard peptidylprolyl isomerase A (*Ppia*), which did not differ between genotypes. Statistical analysis was performed using GraphPad Prism 6.

3.2.6 Biochemical protein analysis

3.2.6.1 Sample collection

Brains of male mice were dissected at P75. The optic nerves were removed at the chiasma, as well as the brainstem underneath the cerebellum. The brains were cut in half and directly frozen on dry ice and stored at -80°C until usage.

Sciatic nerves of male mice were dissected at P75. The nerves were collected from the distal end without muscle tissue, up to the proximal end where the nerve enters the backbone. The sciatic nerves were directly frozen on dry ice and stored at -80°C until usage.

3.2.6.2 Myelin purification

The myelin purification was adapted from a protocol of Norton and Poduslo (Norton and Poduslo, 1973, Larocca and Norton, 2007). Briefly, all supplies were precooled and

procedure was performed on ice or at 4°C. n=3 mouse brains per genotype were used. For myelin purification, half brains were homogenized in 5 ml 0.32 M sucrose containing protease inhibitor (Roche Diagnostics GmbH, Mannheim, Germany) using the IKA T10 basic Ultra-Turrax (Speed 3). For PIP2 measurements, additionally to the protease inhibitor also phosphatase inhibitor (Roche Diagnostics GmbH, Mannheim, Germany) was added. From the homogenate, 200 µl were stored at -80°C for further analysis. For density gradient centrifugation, the homogenate was carefully overlaid on 6 ml 0.85 M sucrose and centrifuged for 30 min at 75000 x *g* in a swing out rotor TH641 (Thermo Fisher Scientific, St. Leon-Rot, Germany) using the Sorvall WX+ Ultra series centrifuge (Thermo Fisher Scientific, St. Leon-Rot, Germany). The roughly purified myelin accumulated at the interphase and was transferred into a new tube. Water was added to the purified myelin and centrifuged again for 15 min at 75000 x *g*. The pellet was re-suspended in ddH_2O, incubated for 10 min on ice and then centrifuged at 12000 x *g* for 15 min. This so-called osmotic shock was repeated a second time. Afterwards the pellet was re-suspended in 5 ml 0.32 M sucrose (containing protease inhibitor (additionally phosphatase inhibitor for PIP_2 measurements)) and carefully overlaid on 6 ml 0.85 M sucrose for a second density gradient centrifugation (30 min at 75000 x *g*). Further purified myelin again accumulated at the interphase and was transferred into a new tube. Water was added to the myelin and centrifuged again for 15 min at 75000 x *g*. The pellet containing a myelin enriched fraction (further referred as purified myelin) was re-suspended in 200 µl 1xTBS including protease inhibitor (additionally phosphatase inhibitor for PIP_2 measurements) and was stored at -80°C (detailed protocol in Erwig et al., accepted).

3.2.6.3 Lysate preparation (PNS)

Of n=3 animals per genotype both sciatic nerves were taken from -80°C and then cut on dry ice. Homogenization was performed in 400 µl RIPA buffer using Precellys (Peqlab, Erlangen, Germany). The nerves got lysed two times with the following adjustments: 6500 rpm 3x 10 sec + 10 sec break. After each time the developed foam was removed by short centrifugation (Heraeus Biofuge Pico table centrifuge, 13000 rpm) and the lysate was kept on ice for further 10 min. In the next step the lysate was transferred into a 1.5 ml tube and centrifuged at 13000 rpm for 10 min at 4°C. The supernatant was then transferred to a new tube and stored at -80°C.

3.2.6.4 Protein concentration determination and sample preparation

To determine the protein concentration of purified myelin, brain lysate, or sciatic nerve lysate, the Lowry assay was performed (Lowry et al., 1951; Peterson, 1979) using the Bio-Rad DC Protein Assay kit. The kit was used according to the manufacturer's 'microplate

assay'-protocol. The optical density was measured at 650 nm using the Eon™ High Performance Microplate Spectrophotometer (BioTek, Vermont, USA).

The obtained protein concentrations were used to set up samples for SDS PAGE separation. The samples were adjusted to 0.1 µg/µl and to 1 µg/µl including 1x SDS sample buffer and 5% β-mercaptoethanol [v/v] to denature the proteins. To detect myelin associated glycoprotein (MAG) and CD9, non-reduced conditions without β-mercaptoethanol were used (protein concentration set to 0.1 µg/µl). The samples were heated for 10 min at 40°C and afterwards kept at -20°C. Before usage the samples were always put to 40°C for 10 min.

3.2.6.5 Protein separation using SDS PAGE

Acrylamid gels (8%, 10%, 12%, or 15% [w/v]) were prepared using the Bio-Rad system. The gels were casted between 1.5 mm thick spacer plates and thin coverplates. First the SDS separating gel was casted and overlaid with isopropanol to get a smooth border. The gel polymerized for 30-60 min, afterwards the isopropanol was rinsed off with ddH_2O. The remaining water was removed with filter papers and the SDS stacking gel was casted on top of the SDS separating gel. A plastic comb (10 well) was used to obtain pockets for protein samples. After another 30 min of polymerization, the gels were used immediately or stored in wet papers at 4°C, not longer than 5 days.

Bio-Rad chambers were used to assemble the gels and the plastic combs were removed. The pockets were washed with 1x Laemmli running buffer while filling up the chamber. The samples were pipetted carefully into the pockets, whereby different amounts of protein were loaded to obtain optimal signals for each antibody detection (see 3.1.8 Primary antibodies - Immunoblot). Proteins were separated by constant current (200 V) for 1 h (until the blue 1x SDS front runs out of the SDS separating gel) using a Bio-Rad power supply. Afterwards the gels were removed from the coverplates and incubated in transfer buffer for 15 min before transferring the proteins to a polyvinylidene difluoride (PVDF) membrane.

3.2.6.6 Immunoblot - semi-dry

For immunodetection, proteins were transferred to a PVDF membrane as described by Towbin and colleagues (Towbin et al., 1979). The PVDF membrane was activated in 100% ethanol [v/v] for 1 min, washed two times shortly with ddH_2O and kept in transfer buffer for 10 min. For the semi-dry blot the Novex® Semi-Dry Blotter (Invitrogen, Karlsruhe, Germany) was used. On the anode plate four Whatman™ papers (GE Healthcare Life Science, Buckinghamshire, UK) soaked in ice cold transfer buffer were placed. To avoid air bubbles in the stack, the Whatman™ papers were rolled with a blotting roller. Afterwards the activated PVDF membrane was placed on top, followed by the gel and four more Whatman™ paper (soaked with ice cold transfer buffer). Proteins were transferred at 20 V

for 45 min using a Bio-Rad power supply. Up to four gels could be transferred simultaneously.

3.2.6.7 Immunoblot - wet tank

To transfer big proteins (>100 kDa) a wet tank blot was performed. The PVDF membrane was activated as described for the semi-dry immunoblot. The membrane was incubated in wet-tank transfer buffer (methanol 20% [v/v]) for 10 min. For blotting the Bio-Rad system was used. Between the brace, a stack of 3 thick Whatman™ paper, the activated membrane, the SDS separating gel, and further 3 thick Whatman™ paper was build. The Whatman™ paper were sucked with ice cold transfer buffer and the whole stack was built together in the buffer. After removing air bubbles with a blotting roller, the brace was clapped together and put in the chamber. The chamber was placed in an ice bucked and filled with pre-cooled transfer buffer. Proteins were transferred by constant current at 100 V for 1.5 h using a Bio-Rad power supply.

3.2.6.8 Immunodetection of blotted proteins

After blotting, the PVDF membrane was incubated in blocking buffer (5% [w/v] non-fat dry milk in TBST) at RT°C for 30-60 min. The primary antibodies were diluted in 5 ml blocking buffer in a 50 ml Falcon® tube (see 3.1.8 Primary antibodies - Immunoblot). The membrane was incubated in these tubes on a rotor at 4°C o/n or over two nights. To increase the binding of some antibodies (e.g. Anillin), the membrane was incubated for further 2 h at RT°C. Afterwards, the membranes were washed in TBST 3x 5 min and then incubated in diluted HRP coupled secondary antibodies (in blocking buffer) for 1-2 h on a rotor at RT°C. The membranes were than washed 3x 5 min in TBST. Membranes were carefully picked up with forceps and placed onto a glass plate. Enhanced chemiluminescence detection (ECL) solution was added according to the manufacturer's recommendations (Western Lightning® Plus-ECL or WesternBright Chemiluminescence Substrat Sirius). After 1 min of incubation, membranes were placed between two plastic foils and chemiluminescence was scanned for one time 1 min and afterwards for 15 min using the Intas ChemoCam system (Intas Science Imaging, Göttingen, Germany).

3.2.6.9 Quantitative Mass Spectrometry

For quantitative mass spectrometry (MS), samples with a protein content of at least 100 µg of purified myelin in 1xTBS (3x *Anln*$^{fl/fl}$ and 3x *Anln*$^{fl/fl}$;*Cnp*$^{Cre/Wt}$) were given to Dr. Olaf Jahn (MPI EM; proteomics unit). Probes were analyzed using DRE-HD-MS^{E}, as described in (Erwig *et al*., accepted). Experiments were performed using three biological replicates each

in two technical replicates. Final quantifications, statistical analysis, and diagrams were prepared with Microsoft Excel 2013 and GraphPad Prism 6.

3.2.7 Histological analysis

3.2.7.1 Perfusion fixation of mouse tissue

Mice were anesthetized by injection of avertin (0.2 ml per 10 g of body weight) interperitoneally (i.p.). The successful anesthesia was confirmed by testing reflexes using a pinch in the hind paws. Afterwards the mice were stabilized with the ventral side up and the abdomen was opened. To expose the heart the diaphragm was removed, so a butterfly cannula (27G, Venofix), connected to a peristaltic pump, could be injected in the left ventricle, while the right atrium was cut. The blood was flushed out with 37°C warm Hank's Balanced Salt Solution (HBSS) (Invitrogen, Karlsruhe, Germany) for 5 min. Afterwards the HBSS was replaced by 4% PFA fixative. To fix the tissue, the fixation run for 10 min (40-50 ml 4% PFA).

3.2.7.2 Embedding for cryosections

Either freshly dissected optic nerves or perfused brains and spinal cords were embedded. Therefore, the tissue was incubated in 4% PFA for 1 h at 4°C and then transferred to 10% [w/v] sucrose in 0.1 M phosphate buffer for 1 h at 4°C. Afterwards, the tissue was kept in 20% [w/v] sucrose in 0.1 M phosphate buffer at 4°C o/n. After further o/n incubation in 30% [w/v] sucrose in 0.1 M phosphate buffer at 4°C the tissue was embedded in Tissue-Tek® O.C.T.™ Compound (Sakura, Staufen, Germany) and afterwards stored at -20°C. For sectioning, the Reichert Jung® Cryocut 1800 Cryostat (Leica, Wetzlar, Germany) was used. 10 µm thick sections were collected on Superfrost® Plus microscope slides (Thermo Fisher Scientific, St. Leon-Rot, Germany) and dried at RT°C. For storage, the slides were kept at -20°C.

3.2.7.3 Immunohistochemistry - cryosections

The following protocol was used for immunohistochemistry of cryosections:

Purpose	Reagent	Conditions
Permeabilization	Methanol	3 min at RT°C
Washing	1x PBS	3x 5 min at RT°C
Blocking	Blocking buffer (3.1.11)	1 h at RT°C

1. Antibody	Diluted in blocking buffer	o/n at 4°C	
Washing	1x PBS	3x 5 min	
2. Antibody	Diluted in blocking buffer	1-2 h at RT°C	Kept dark
Washing	1x PBS	2x 10 min at RT°C	
DAPI	DAPI 1:50000 in 1x PBS	10 min at RT°C	
Washing	1x PBS	2x 10 min at RT°C	
Washing	ddH_2O	2x 2 min at RT°C	
Mounting	Aqua-Poly/Mount or Fluoromount-G™	at RT°C	
Storage		4°C	

3.2.7.4 Imaging and analysis of fluorescent staining

Slides were imaged with the confocal microscope Leica SP5. Signal was collected sequentially with the objective HCX PL APO CS 63.0 × 1.30 GLYC 21°C UV. An argon laser with the excitation of 488 nm was used to excite the Alexa 488 fluorophore and the emission was set to 500-560 nm. Cy3 was excited with the DPSS 561 laser at an excitation of 561 nm and the emission was set to 573-630 nm. Also the Alexa 555 fluorophore was excited with the DPSS 561 laser, and the emission was set to 575-630 nm. The HeNe laser was used to excite Dyelight633 with 633 nm and emission was detected between 645-738 nm. DAPI was excited with 405 nm and collected between 417-480 nm. The LAS AF lite software was used to export the images as TIF files. The original pictures of images in Figure 8A and B, were partially provided by Julia Patzig. The Imaris software was used for 3D-reconstructions.

For the quantifications of nodal density, the frequency of occurrence of two CASPR-immunopositive paranodes was analyzed using the ImageJ software. CASPR-immunopositivity was converted using a threshold and counted using ITNC plugin (n=4 animals per genotype, 1 section each, 1 micrograph analyzed (size 16000 μm^2). Statistical analysis was performed using GraphPad Prism 6.0.

The node and paranode length (indicated in Figure 16) was assessed using the ImageJ software. For paranode length the mean of both paranodes beside an axon were calculated.

n=4 animals per genotype, 1 section each, 5 random micrographs of spinal cord white matter. Statistical analysis was performed using GraphPad Prism 6.0.

3.2.7.5 Embedding for paraffin sections

Mice were perfused with 4% PFA and post-fixed o/n at 4°C. Before embedding, brains were divided coronal into 3 parts using a brain slicer. For thin sectioning, the tissue was embedded in paraffin (Paraplast, Leica, Wetzlar, Germany) using the automated system HMP 110 ((Microm, Walldorf, Germany) with the following program:

Procedure	Time
50% [v/v] Ethanol	1 hour
70% [v/v] Ethanol	2x 2 hours
96% [v/v] Ethanol	2x 2 hours
100% [v/v] Ethanol	2x 2 hours
Isopropanol	1 hour
Xylol	2x 2 hours
Paraffin	2x 2 hours

Afterwards, the tissue was placed into metal forms with the sectioning side facing the ground. The tissue was then casted with 60°C warm paraffin and put on a pre-cooled plate for hardening (Paraffin embedding station: MICROM AP280 (Microm, Walldorf, Germany). The blocks were removed and stored at RT°C. The tissue was cut in 5 µm thick sections using a microtome (HM 400, MICROM (Microm; Walldorf, Germany) and dried o/n at 37°C. The sections were stored at RT°C until further usage. The sectioning was partially done by Annette Fahrenholz.

3.2.7.6 Immunohistochemistry - paraffin sections

Before usage, the sections were deparaffinized by the following steps:

Procedure	Time
60°C	10 min
Xylol	2x 10 min
Xylol/Isopropanol (1:1)	10 min
100% [v/v] Ethanol	5 min
90% [v/v] Ethanol	5 min
70% [v/v] Ethanol	5 min
50% [v/v] Ethanol	5 min
ddH_2O	5 min

For permeabilization of the 5 µm thick sections, the slides were incubated in citrate buffer for 5 min and then cooked for 10 min in boiling citrate buffer (650 Watts in microwave oven). After cooling for 20 min, the sections were placed in Tris buffer containing 2% [w/v] non-fat dry milk. Afterwards the slides were placed into Shandon Coverplates™ (Thermo Fisher Scientific, St. Leon-Rot, Germany). These coverplates ensure an even distribution of small volume amounts of antibody-dilutions. The slides were again rinsed with Tris buffer containing 2% [w/v] non-fat dry milk. Afterwards, as horse radish peroxidase (HRP) coupled secondary antibodies were used, the endogenous peroxidase activity was inhibited by applying 3% [v/v] hydrogen peroxide for 5 min. After washing with Tris buffer containing 2% [w/v] non-fat dry milk, the slides were incubated in blocking solution (20% [v/v] goat serum in BSA/PBS) for 30 min at RT°C. Primary antibodies were diluted in BSA/PBS and incubated o/n at 4°C. On the next day, the slides were washed with Tris buffer containing 2% [w/v] non-fat dry milk. For staining of amyloid beta precursor protein (APP), ionized calcium-binding adapter molecule 1 (IBA1), and glial fibrillary acidic protein (GFAP) the LSAB2 kit (Dako, Hamburg, Germany) was used. The sections were incubated with 100 µl of bridging antibody i.e. a biotinylated secondary antibody for 10 min at RT°C and rinsed with Tris buffer containing 2% [w/v] non-fat dry milk. The HRP complex bound antibody was incubated for 10 min at RT°C. For staining of macrophages/activated microglia (MAC3), sections were incubated with an α-rat-biotinylated antibody (Vector Labs, Burlingame, California, United States) for 30 min. The two components of the Vector Elite ABC kit (Vector Labs) were mixed and the slides incubated for 30 min. The coverplates were removed and all sections were rinsed with Tris buffer without non-fat dry milk. The HRP substrate 3,3'-Diaminobenzidine (DAB) was applied by using the DAB Zytomed Kit (Zytomed Systems GmbH, Berlin, Germany) and incubated for 10 min. Brown labeling appeared where antibodies recognized their targets. After additional washing with ddH_2O, sections were incubated in 0.1% [w/v] Haematoxylin for 5 min to label nuclei. Blue coloration appears due to the interaction with the basic nuclear compartment. Sections were rinsed with ddH_2O, incubated with HCl-Alcohol for 5-10 sec and with Scott's solution for 5 min. This was followed by additional rinse with ddH_2O. The tissue was dehydrated by the following steps:

Procedure	Time
50% [v/v] Ethanol	5 min
70% [v/v] Ethanol	5 min
90% [v/v] Ethanol	5 min
100% [v/v] Ethanol	5 min
Xylol/Isopropanol (1:1)	5 min
Xylol	2x 5 min

In the end, slides were mounted using Eukitt (Kindler, Freiburg, Germany). The stainings were partially done by Annette Fahrenholz.

3.2.7.7 Imaging and quantification of DAB developed stainings

The DAB stained sections were imaged using the Zeiss Axio Z1 with the Zen 2011 software (Zeiss, Oberkochern, Germany). The quantification of GFAP, IBA1, and MAC3 signal was done using an ImageJ plugin for semi-automated analysis. First, the color threshold was used to transform the colored picture to a black and white picture; brown signal represented by positive black signal. Second, the area of the positive black signal was measured and related to the size of the analyzed area. Diagrams, quantification and Student's t-test (p-value) were prepared with GraphPad Prism 6.

The APP positive spheroids were counted manually, using the ImageJ software. Diagrams, quantification and statistical analysis were prepared with GraphPad Prism 6.

For all quantifications, the hippocampal fimbria was selected. For each animal, the average of both fimbriae was calculated. Data were normalized to wild type levels. All quantifications were performed blinded to the genotype. The quantifications were performed at P75 with an n=5 per genotype.

3.2.7.8 Gallyas silver impregnation

Deparaffinized 10 µm brain sections (coronal) and cerebellum sections (sagital) were used. The technique developed by Gallyas is based on binding of colloidal silver particles to myelinated fibers (Gallyas, 1979). The silver impregnation has been done by Annette Fahrenholz. To visualize myelin, the following protocol has been used:

Purpose	Reagent	Incubation time
Blocking of non-myelin tissue	Pyridine/acetic acid (2:1)	30 min
Washing	ddH_2O	3x 10 min
Incubation	Incubation solution	1 min 100 Watts microwave 10 min RT°C
Washing	0.5% [v/v] Acetic acid	3x 5 min

Developing	Physical developer: 100 ml Solution A 70 ml Solution B 30 ml Solution C	3-15 min
Stop reaction	1.0% [v/v] Acetic acid	3x 5 min
Washing	ddH_2O	2x 3 min
Stabilization	2% [v/v] Sodium thiosulfate	5 min
Dehydartion	50% [v/v] Ethanol 70% [v/v] Ethanol 90% [v/v] Ethanol 100% [v/v] Ethanol Xylol/Isopropanol (1:1) Xylol	5 min 5 min 5 min 5 min 5 min 2x 5 min

The slides were in the end mounted using Eukitt (Kindler, Freiburg, Germany). Images were captured at 10x magnification (Zeiss AxioImager Z1) and stitched using Zeiss Zen2011. Images in Figure 18A and A' are representative for n=3 mice per genotypes at P75.

3.2.8 Electron microscopy (EM)

3.2.8.1 Tissue preparation - Electron microscopy

Animals were sacrificed by cervical dislocation and optic nerves were carefully removed at the chiasm. Sciatic nerves were dissected, whereby at the distal side a piece of muscle was kept attached for future identification of the distal end. The freshly dissected nerves were directly incubated in Karlsson-Schultz fixative (K&S) and stored at 4°C until further processing.

3.2.8.2 Epon embedding

For EM imaging, the fixed nerves were embedded using an automated system (EMPT, Leica, Wetzlar, Germany). Before embedding the nerves were washed with 0.1 M phosphate buffer and placed into plastic chambers. The tissue was processed using the following protocol:

Solution	Incubation time	Temperature
Phosphate buffer	3x 10 min	4°C
2% [w/v] OsO_4	4 h	4°C
ddH_2O	3x 10 min	4°C
30% [v/v] Ethanol	20 min	4°C
50% [v/v] Ethanol	20 min	4°C
70% [v/v] Ethanol	20 min	4°C
90% [v/v] Ethanol	20 min	4°C
100% [v/v] Ethanol	4x 10 min	4°C
Propylenoxid	3x 10 min	RT°C
Propylenoxid/Epon 2:1	2 h	RT°C
Propylenoxid/Epon 1:1	2 h	RT°C
Propylenoxid/Epon 1:2	4 h	RT°C
Epon	4 h	RT°C

The tissue was then placed into molds filled with Epon. A label was put within the Epon for identification of the probe and left o/n at 60°C for Epon polymerization.

3.2.8.3 Sectioning of Epon embedded tissue

For semi-thin sectioning the embedded sciatic nerves were cut into 500 nm thin sections. This was done with a microtome (Ultracut S, Leica, Wetzlar, Germany) and a diamond knife (Diatome Ultra 45º). The sections were collected on water and then transferred onto an object slide (Marienfeld with help of a Pasteur pipette. The object slide was then put on a 60 °C hot plate to dry the sections.

To analyze the embedded optic and sciatic nerves on electron microscope level, 50 nm thin sections were cut using the same equipment as for the semi-thin sections. The sections were collected on formvar polyvinyl coated double sized slot grids (2 mm-1 mm, AGAR scientific, Essex, UK).

3.2.8.4 Staining of semi-thin sections

500 nm thin sections of sciatic nerves were stained with Methylene blue-Azure II solution (Richardson et al., 1960). On a 60°C hot plate, sections were incubated for 1 min in the staining solution and then extensively rinsed with ddH_2O. After drying, the tissue was mounted using Eukitt and imaged with a 100x oil objective of the Zeiss Axio Imager Z1 (Zeiss, Oberkochern, Germany).

3.2.8.5 Contrasting of ultra-thin sections

For proper contrasting of ultra-thin sections, the formvar polyvinyl coated double sized slot grids were placed upside-down on drops of the following solutions:

Solution	Incubation time
Uranyl acetate	30 min (kept dark)
ddH_2O	3x 1 min
Reynolds lead citrate	6 min
ddH_2O	6x 1 min

Alternatively, the sections carrying grids were placed upside-down on a drop of UranyLess (Electron Microscopy Science, Hatfield, Panama) for 30 min and then washed 6 times with ddH_2O.

3.2.8.6 Analysis of EM pictures

Ultra-thin sections were analyzed with the Zeiss EM900 (Zeiss, Oberkochen, Germany) and digital pictures were obtained using the wide-angle dual speed 2K-CCD-Camera (TRS, Moorenweis, Germany). g-ratio measurements and quantifications of myelin abnormalities were performed using the ImageJ software. Microsoft Excel 2013 was used for calculations of the g-ratio. Diagrams, quantification and statistical analysis were prepared with GraphPad Prism 6. All quantifications were performed blinded to the genotype. Presentation of pictures was prepared using Adobe Photoshop CS6 and Adobe Illustrator CS6.

The g-ratio was calculated as the ratio between the axonal Feret diameter and the Feret diameter of the corresponding myelin sheath (Figure 19A). To determine g-ratios, one quarter (55 µm²) of at least 15 images was quantified, yielding a minimum of 200 myelinated axons per animal. n=5 per genotype at 6 mo of age. The g-ratio was assessed using GraphPad Prism 6.0. For calculation, only normal appearing myelinated axons were

analyzed (Figure 8), to ensure that possible changes in myelin thickness could be related to the loss of ANLN and are not cause of other pathological effects.

For assessment of % of myelinated axons and % of degenerating/degenerated profiles, mice were analyzed at an age of 6 mo. 4-5 male mice were used per genotype. 15 randomly selected, non-overlapping images were taken per optic nerve at 7000× magnification (1 field = 220 µm²). Electron micrographs were analyzed using ImageJ. A minimum of 1600 axons per animal were assigned to one of three categories: healthy-appearing myelinated axons, healthy-appearing non-myelinated axons, and degenerating/degenerated axons (partially shown in Figure 8). Axons were counted as myelinated if ensheathed by at least one complete layer of compacted myelin. Degenerating/degenerated axons were identified by tubovesicular structures, amorphous cytoplasm, axonal spheroids or absence of an identifiable axon within a myelin sheath, respectively.

The area occupied by myelin outfoldings was quantified by a point counting method (Edgar et al., 2009) at different time points (P14, P75, 6 mo; n=4-6 per genotype). Briefly, a regular grid of 0.25 μm^2 was placed on the images. The number of intercepts coinciding with myelin outfoldings was related to the evaluated area. Significance was determined using GraphPad Prism 6.0.

To identify the axon diameter frequency distribution, one quarter (55 µm²) of at least 15 images was quantified, yielding the axon diameter of at least 200 up to 650 myelinated axons per animal. The images for *Cnp* heterozygous and SEPT8 deficient mice and their corresponding controls were kindly provided by Ulrike Gerwig (CNP) and Julia Patzig (SEPT8). n=5 for all genotypes and all time points. The diameter was calculated using ImageJ, therefore the axon was encircled and the Feret diameter was calculated by the software. The frequency distribution was visualized using GraphPad Prism 6.0, the bin size was set to 0.2 and each replicate was binned. Significance was determined using GraphPad Prism 6.0 (Kolmogorov-Smirnov Test). All quantifications were performed blinded to the genotype.

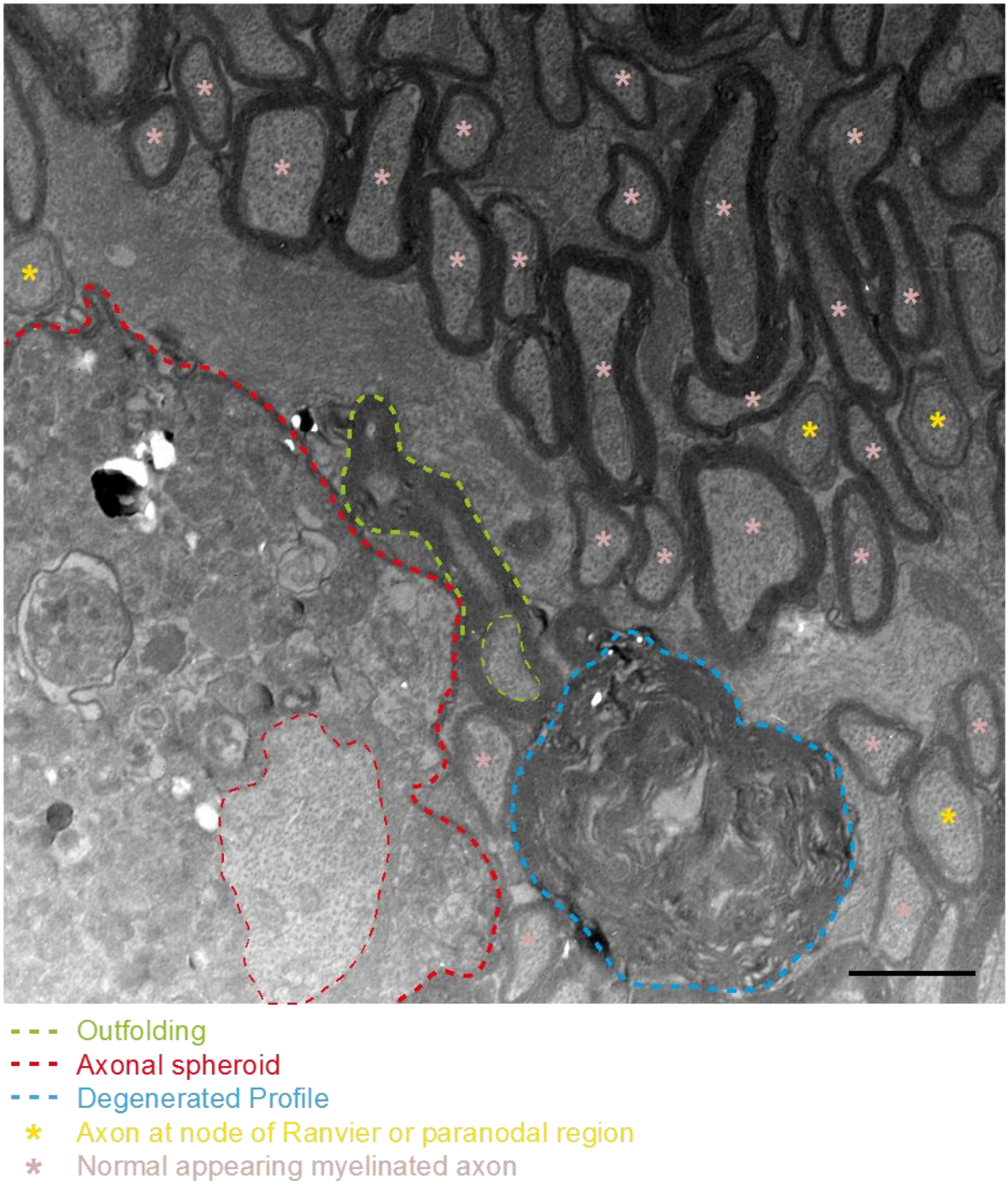

Figure 8: Overview of profiles found in electron micrographs. Electron micrograph of an *Anln* cKO optic nerve cross section at 6 mo of age. The image exemplifies different kinds of detected profiles within an optic nerve. The profile marked in red is showing an axonal spheroid, whereby the light line surrounds the axon and the bold line is marking the corresponding compact myelin. The blue marked profile surrounds redundant myelin, where no axon was identifiable within myelin sheaths. Green marks an axon with an outfolding, whereby the light line surrounds the axon and the bold line surrounds the outfolding. Axons marked with a yellow asterisk show axons that are likely at a node of Ranvier or paranodal region, as they are surrounded by a thin layer of compact myelin and in addition the axons are surrounded by a thicker layer of cytoplasm (King, 2013). Axons marked with a light red asterisk are classified as normal appearing myelinated axons, as they show no signs of pathology. Scale bare: 1 µm

3.2.9 Focused ion beam scanning electron microscopy (FIB SEM)

The following steps were done by the EM facility of the MPI EM. Anna Steyer prepared the samples and processed all steps to obtain images. Christos Nardis segmented the images for the 3D reconstruction.

3.2.9.1 Sample preparation

Mouse optic nerves were fixed in 4 % formaldehyde and 2.5 % glutaraldehyde (Science Services) in 0.1 M PB for at least 24 h. The samples were processed following a modified OTO (Deerinck et al., 2010) protocol. The samples were washed in 0.1 M PB (3 x 15 min) and then incubated for 3 h at 4 °C in 2 % OsO_4 (Electron Microscopy Sciences) and 0.25 % $K_4[Fe(CN)_6]$ (Electron Microscopy Sciences). The nerves were washed with H_2O (3 x 15 min) and were incubated with 0.1 % thiocarbohydrazide (Sigma-Aldrich) for 1 h at room temperature. To enhance the contrast further the tissue was treated with 2 % OsO_4 for 90 min at room temperature. The samples were washed with H_2O (3 x 15 min) and contrasted overnight with 2 % uranyl acetate (SPI-Chem) at 4 °C. The samples were washed again with H_2O (3 x 15 min), followed by dehydration in an increasing acetone series (30 %, 50 %, 75 %, 90 %, 3 x 100%). The tissue was infiltrated with increasing concentrations of Durcupan (Sigma-Aldrich, components A, B, C) 2 h each (25 %, 50 %, 75 % Durcupan in acetone) and then incubated in 100 % Durcupan o/n. Fresh Durcupan with accelerator (component D) was added to the samples for 5 h, before embedding the samples in resin blocks. The blocks were polymerized for 48 h at 60 °C.

3.2.9.2 FIB SEM procedure

Samples were trimmed with a 90° diamond trimming knife (Diatome AG, Biel, Switzerland). The blocks were attached to the SEM stub (Science Services GmbH, Pin 12.7 mm x 3.1 mm) by a silver filled epoxy (Epoxy Conductive Adhesive, EPO-TEK EE 129-4; EMS) and polymerized at 60° overnight. The samples were coated with a 10 nm platinum layer using the sputter coating machine EM ACE600 (Leica) at 35 mA current. Samples were placed into the Crossbeam 540 focused ion beam scanning electron microscope (Carl Zeiss Microscopy GmbH). To ensure even milling and to protect the surface, a 400 nm platinum layer was deposited on top of the region of interest. Atlas 3D (Atlas 5.1, Fibics, Canada) software was used to collect the 3D data. Samples were exposed with a 15 nA current and a 7 nA current was used to polish the surface. The images were acquired at 1.5 kV with the ESB detector (450 V ESB grid, pixel size x/y 2 nm) in a continuous mill and acquire mode using 700 pA for the milling aperture (z-step 50 nm).

3.2.9.3 Image analysis

Image alignments were done with TrakEM2 (Cardona et al., 2012), a plugin of Fiji (Schindelin et al., 2012). The following post-processing steps were performed in Fiji. The dataset was cropped, inverted and a local contrast enhancement (CLAHE) was applied. The images were manually segmented using IMOD (Kremer et al., 1996).

3.2.10 Electrophysiology

Nerve conduction velocity in the CNS was measured in vivo on 6 month old male mice (2 *Anln*$^{fl/fl}$, 9 controls (WT from (Patzig et al., 2016)), 7 *Anln* cKO). *Anln*$^{fl/fl}$ mice and controls were pooled after testing significance (not significant; two-tailed unpaired t-test; p= 0.8399). Measurements were performed by Dr. Payam Dibaj (MPI EM) essentially as described (Dibaj et al., 2012, Patzig et al., 2016).

3.2.11 PIP_2 measurement

Purified myelin of n=6 male mice at P75 were sent to Prof. Dr. Ingo Heilmann (Halle, Germany). Lipid extraction followed by combined thin layer chromatography and gas chromatography was used to measure PIP_2 levels (Goebbels et al., 2010, Konig et al., 2008).

4 Results

4.1 The ANLN/septin filament in CNS myelin

4.1.1 Anillin and septins co-localize in CNS white matter

To identify the localization of ANLN in relation to myelin septins, immunohistochemical triple-stainings were performed on cryosections of mouse optic nerves (longitudinal) and mouse brains (coronal). As reference, different known markers of myelin or axons were used. MAG (Cyan) is a known marker of the adaxonal myelin membrane (Trapp and Quarles, 1982, Trapp et al., 1989), where the septin filament is localized as well (Patzig et al., 2016). The markers NF (neurofilament) and TUJ1 (βIII-Tubulin) were used to visualize axons (Cyan). ANLN (red) was found to co-localize to SEPT8 (green) in longitudinal cryosections of optic nerves (Figure 9A), showing a similar filament-like labeling as SEPT8 (arrowheads). The same co-localization was detected in white matter tracts of coronal cryosections of mouse brains (Figure 9B). Filaments (arrowheads) along axons were found in the fimbria (b-b') as well as in the corpus callosum (b''). Images in A and B were obtained together with Dr. Julia Patzig.

For 3-dimensional (3D) reconstruction, z-stacks of fluorescent immunohistochemical stainings of longitudinal spinal cord cryosections were generated via confocal laser scanning microscopy (Figure 9C and D). To reconstruct the confocal z-stacks into 3D, the Imaris software was used. Figure 9C shows maximal projections of confocal z-stacks and a 3D reconstruction of SEPT7 (green) and an axonal marker (NF; red). The images display the known filament-like assembly of SEPT7 along the axon, as seen in Patzig et al. (2016). Figure 9D shows maximal projections of confocal z-stacks and a 3D reconstruction of ANLN and the axonal marker NF. The images illustrate a filament-like structure of ANLN along the axon, as well as a patchy pattern all over the axon.

Figure 9E shows the protein abundance of ANLN and SEPT8 in brain lysate and purified myelin. A myelin marker (MOG) and an axonal marker (TUJ1) were loaded as controls for the responsive fraction. The abundance of MOG is strongly enriched in purified myelin, whereas the abundance of TUJ1 is decreased. ANLN was only detectable in purified myelin, supporting the localization in mouse brain white matter.

Taken together, the results suggest a similar distribution of ANLN along the axon, as previously found for septins. Additionally, ANLN localizes to parts of the axon without SEPT8 co-localization.

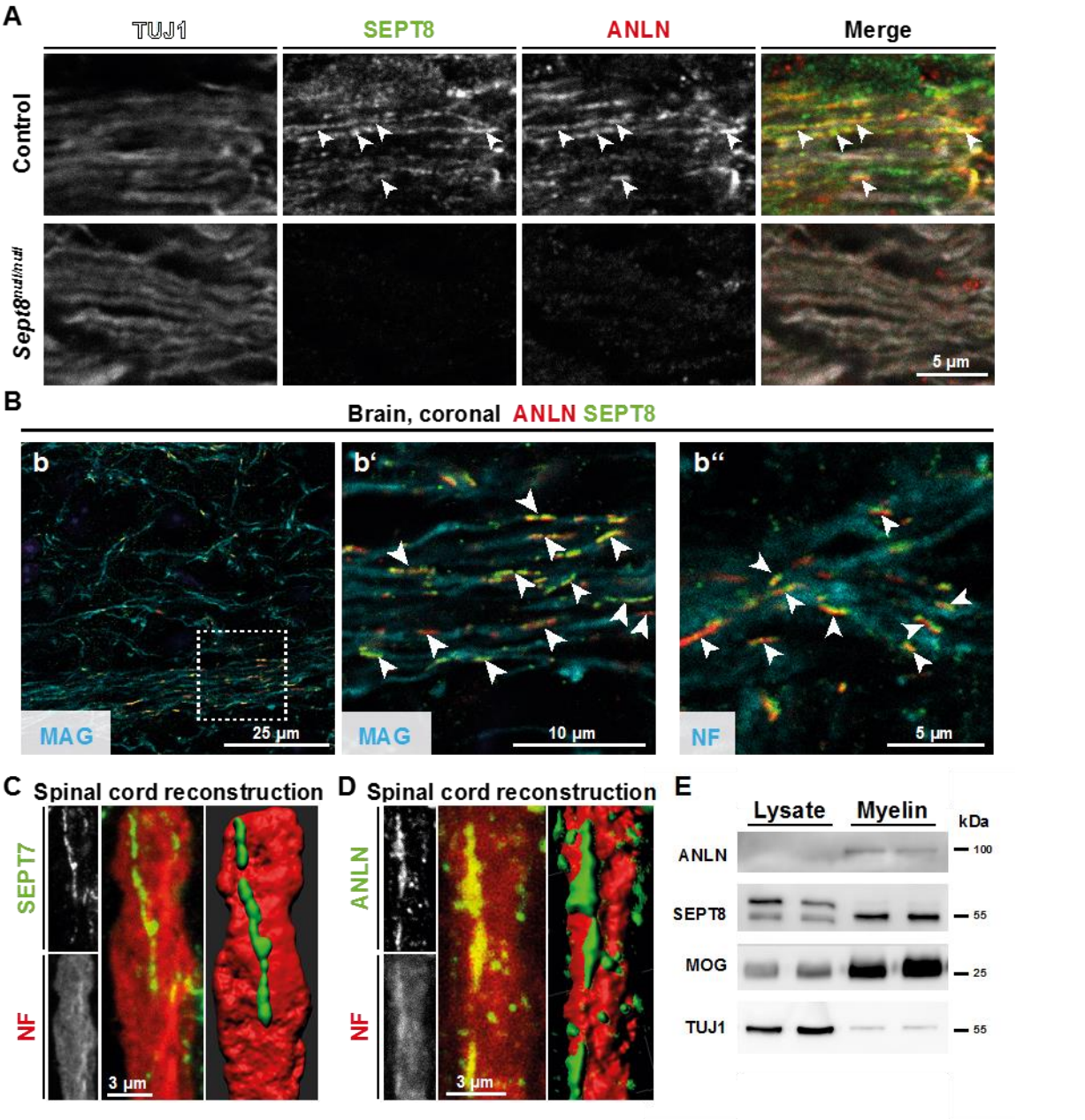

Figure 9: Localization of the ANLN/septin filaments in mouse CNS. (**A**) Immunolabeling validates close proximity (arrowheads) of ANLN (red) with SEPT8 (green) in myelinated fiber tracts of wild type (Wt) mice. Immunolabeling of *Sept8*$^{null/null}$ mice indicates diminishment of ANLN similar to SEPT8. Longitudinally sectioned optic nerves of P75 mice are shown. TUJ1 (white) was labeled as an axonal control. Images are representative of three independent experiments. (**B**) Immunolabeling of coronal brain sections of P75 Wt mice detects ANLN (red) and SEPT8 (green) filaments (arrowheads) in white matter tracts. **b-b'** shows labeling in the fimbria. In **b'** a blow up of the dashed square in **b** is shown. **b''** shows labeling in the corpus callosum. MAG/NF were labeled as control. (**C**) Immunofluorescent signal of SEPT7 (green) extends longitudinally along axons (neurofilament-labeling (red)). Images display maximal projections of confocal z-stacks and a 3-dimensional reconstruction of longitudinally sectioned spinal cord of P75 Wt mice. Images are representative of three animals. (**D**) Immunofluorescent signal of ANLN (green) partially extends longitudinally and partially patchy along axons (neurofilament-labeling (red)). Images display maximal projections of confocal z-stacks and a 3-dimensional reconstruction of longitudinally sectioned spinal cord of P75 control mice (*Anln*$^{fl/fl}$). Images are representative of three animals. (E) Immunoblot analysis of brain lysates and myelin purified from P75 control mice (*Anln*$^{fl/fl}$). It is of note that ANLN is only detectable in purified myelin. MOG and TUJ1 were detected as controls. Images in A and B were obtained together with Dr. Julia Patzig.

4.1.2 ANLN and septins appear similar in development

To possibly discover the chronology of appearance of ANLN and septins, the abundances of these proteins were analyzed in mice at different developmental states. Immunohistochemical triple-stainings were performed on longitudinal cryosections of mouse optic nerves at P15, P21, and P28 (Figure 10A, Images were obtained together with Dr. Julia Patzig). ANLN and SEPT8 were found to appear around P21. Each filament-like labeling was positive for both, ANLN and SEPT8. At P28 the filament-like labeling was seen more often compared to P21. In Figure 10B, immunoblots on mouse brain myelin illustrate the abundance of ANLN and CNS myelin septins at P15, P18, P21, and P24. ANLN appears in the same pattern as septins, showing an increasing abundance up to P21.

Taken together, every filament-like labeling shows both, ANLN and septin labeling. Further, the abundance of ANLN and septins increases in the same pattern, suggesting that both, ANLN and septins are needed to form a cytoskeletal structure.

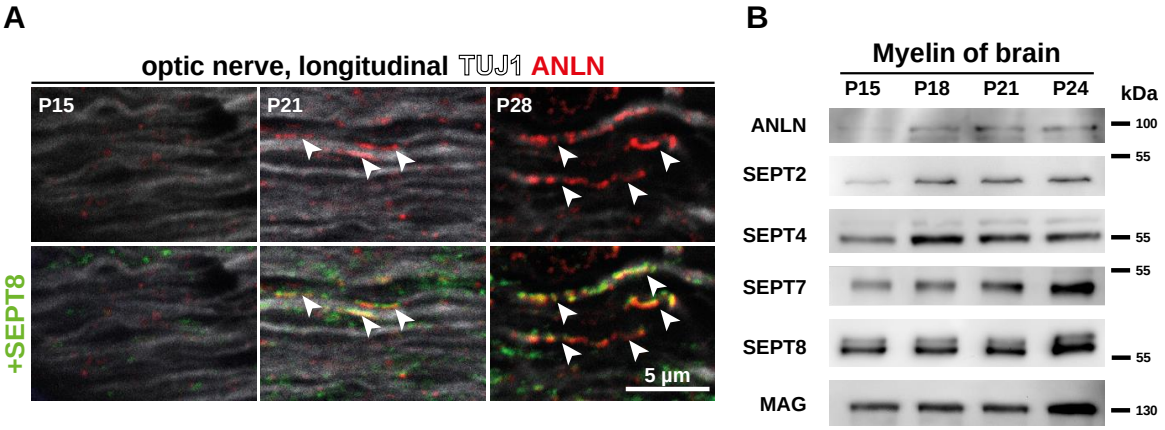

Figure 10: ANLN and septins in development. (**A**) Immunolabeling of wild type optic nerves detects ANLN (red) partially at P21 and at P28 but not at P15. Note that every filamentous ANLN labeling is in close proximity to SEPT8 (green) labeling, indicated by arrowheads. TUJ1 was labeled as an axonal marker. Images are representative of three experiments. Images were obtained together with Dr. Julia Patzig (**B**) Immunoblotting indicates that the abundance of ANLN and septins (SEPT2, SEPT4, SEPT7, SEPT8) increases with age in myelin purified from wild type brains at P15, P18, P21, and P24, reflecting the maturation of myelin. L-MAG was detected as control.

4.2 Characterization of *Anln*$^{fl/fl}$;*Cnp*$^{Cre/Wt}$ mice

4.2.1 Generation of mice lacking ANLN from myelinating glia cells

As described in 3.2.2, *Anln* cKO mice were generated (Ramona Jung (MPI EM) and Ursula Fünfschilling (MPI EM, transgenic service)). The scheme in Figure 11A depicts the ordered construct (ES cells ordered from EUCOMM) and the conditional deletion of the *Anln* gene. Figure 11B illustrates the results of the genotyping PCR (described in 3.2.4). The upper row depicts that only in presence of the Cre recombinase a product of about 350 bp is present. In the middle row, it is depicted that the loxP sites increase the PCR product arising from

primer 1 (P1) and primer 2 (P2). In the lower row, a product from P1 and primer 4 (P4) arises solely in the *Anln* cKO mice. The binding site of each primer is depicted in Figure 11A.

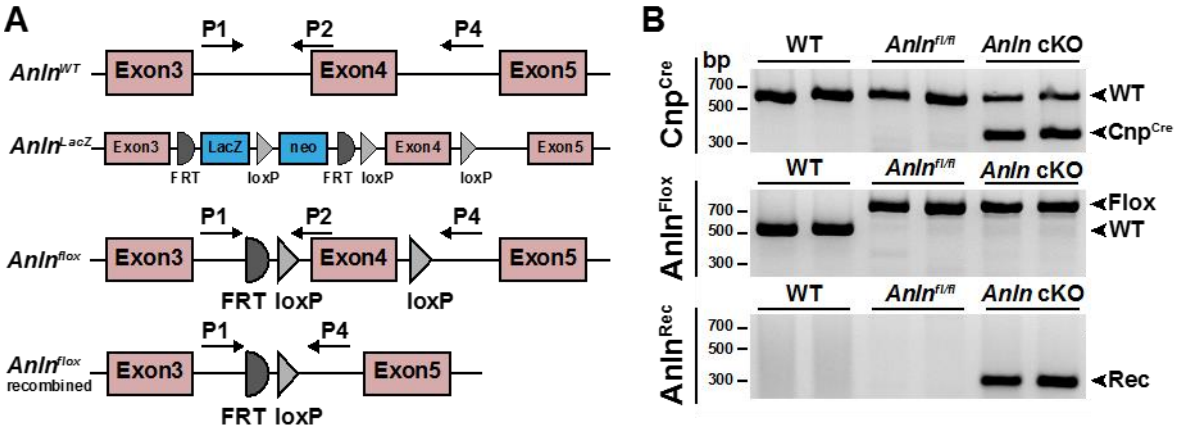

Figure 11: Generation of *Anln*$^{fl/fl}$;*Cnp*$^{Cre/Wt}$ mice. (**A**) Scheme for conditional inactivation of the *Anln* gene. Exon 4 of the *Anln* allele is flanked by loxP-sites for Cre-mediated recombination. Positions of PCR primers (P1, P2, P4) are indicated. (**B**) Genotyping PCR of DNA isolated from mouse tail tips at P21. Upper row depicts Cre-specific PCR product in *Anln* cKO mice. Middle row depicts PCR product of primer P1 and P2 in controls (Wt and *Anln*$^{fl/fl}$) and *Anln* cKO mice. Note that the loxP-sites increase the PCR product as expected. Lower row depicts PCR product of primer P1 and P4 after recombination. Note that the recombination band is specific for *Anln* cKO mice.

4.2.2 Mass spectrometric comparison of *Anln* cKO mice and controls

For quantitative analysis of protein abundances, myelin of controls and *Anln* cKO mice were compared using mass spectrometry (MS) (Olaf Jahn, MPI EM; proteomics unit). In total, 446 proteins were identified using a HD-MS^E approach. In Figure 12A, the data for all identified proteins are plotted as $\log_2$ fold change ($\log_2$ FC) versus the −log10 of the modified p-value (q-value) in a Volcano plot. The dashed lines indicate the applied threshold of +1 and -1 $\log_2$ FC, indicative of a halved or doubled abundance of a protein in myelin, respectively. Only CNS myelin septins are reduced below the applied threshold. CDC42 and RHOB are also significantly reduced regarding the q-value, but not below the fold change threshold. These proteins are also known to be involved in ANLN/septin filament formation (light red dots, Figure 12A). As ANLN is not detected by MS in myelin of *Anln* cKO mice (Figure 12B) it is not included in the Volcano plot (Figure 12A). However, the genotype dependent reduction of CNP is detected by MS (Figure 12B). Figure 12C displays the comparison between myelin of controls and *Anln* cKO mice of ANLN/septin filament formation related proteins (SEPT4, SEPT2, SEPT8, SEPT7, RHOB, CDC42) (Joberty et al., 2001, Renshaw et al., 2014, Mendoza et al., 2002). The proteins are sorted from highest decrease in *Anln* cKO mice to lowest decrease in abundance of the 6 selected proteins. All CNS myelin septins are reduced more than 50% (p-value <0.0001), RHOB and CDC42 are also significantly reduced (ROHB p=0.0022; CDC42 p=0.0368). Within the 446 identified

proteins, classical myelin markers were selected and compared between genotypes (Figure 12D). Throughout all identified myelin marker proteins (except CNP; see above), no significant change was detectable. Since anillin is known to interact with other cytoskeletal components (Piekny and Glotzer, 2008, Straight et al., 2005, Piekny and Maddox, 2010, Versele and Thorner, 2005), all cytoskeleton related proteins within the dataset were identified and compared between the genotypes. There was no significant change in abundance throughout all identified cytoskeletal markers.

To summarize, the results support the efficient depletion of ANLN from oligodendrocytes in *Anln* cKO mice. Further, the loss of ANLN in myelinating glia cells leads to a strong reduction of CNS myelin septins but has no effect on other detected proteins. These results further strengthen the expected interaction of anillin and septins in CNS myelin.

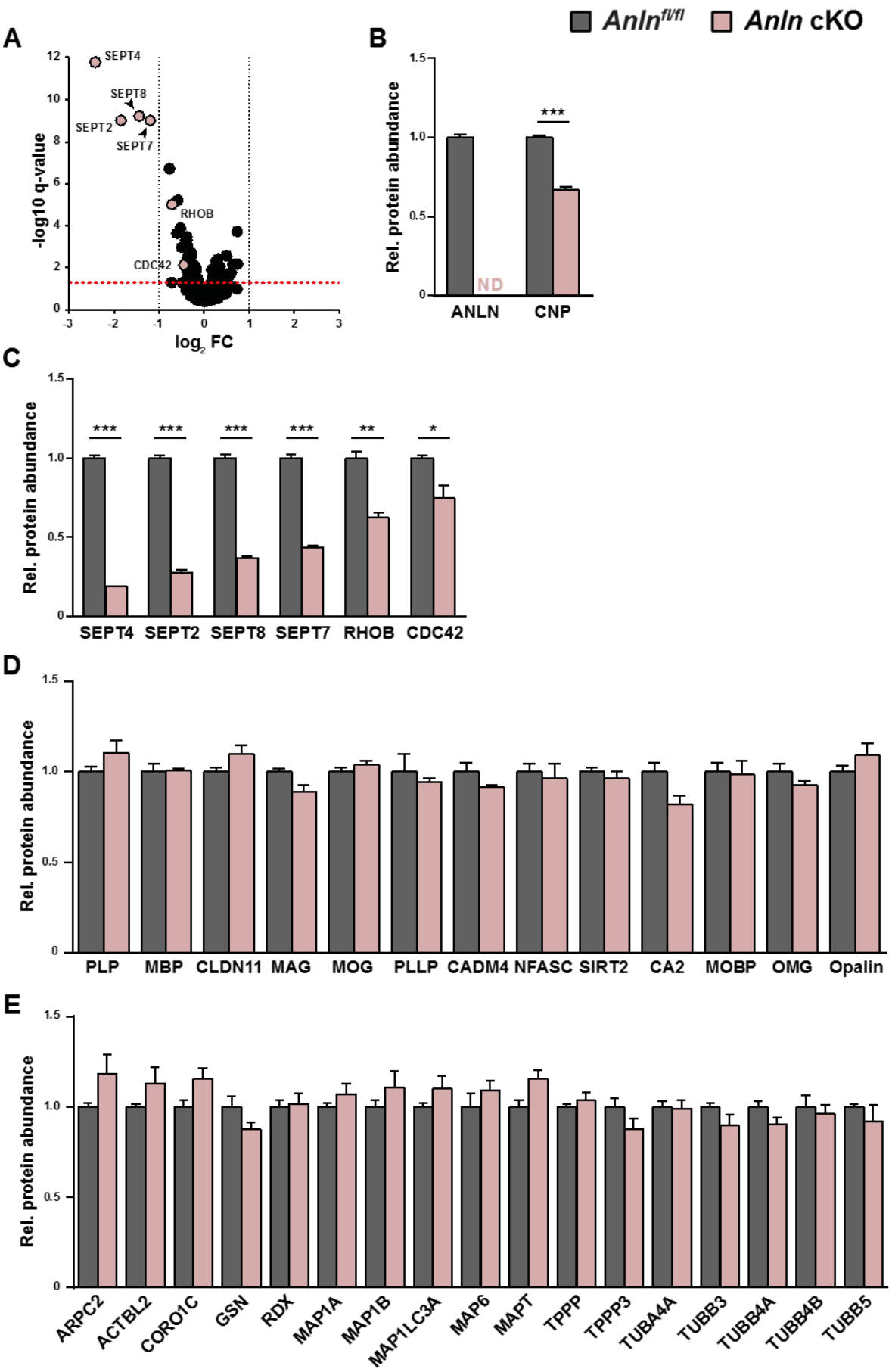
A
SEPT4
SEPT8
SEPT2
SEPT7
RHOB
CDC42
-log10 q-value
log2 FC
B
Anln fl/fl
Anln cKO
Rel. protein abundance
***
ND
ANLN
CNP
C
Rel. protein abundance
***
***
***
***
**
*
SEPT4
SEPT2
SEPT8
SEPT7
RHOB
CDC42
D
Rel. protein abundance
PLP
MBP
CLDN11
MAG
MOG
PLLP
CADM4
NFASC
SIRT2
CA2
MOBP
OMG
Opalin
E
Rel. protein abundance
ARPC2
ACTBL2
CORO1C
GSN
RDX
MAP1A
MAP1B
MAP1LC3A
MAP6
MAPT
TPPP
TPPP3
TUBA4A
TUBB3
TUBB4A
TUBB4B
TUBB5

Figure 12: Mass spectrometric analysis of purified myelin. (**A**) Volcano plot of proteome data comparing proteins of purified myelin of *Anln* cKO to *Anln*$^{fl/fl}$. The data for all identified proteins are plotted as log_2 fold change (log_2 FC) versus the −log10 of the modified p-value (q-value). Black dashed lines indicate the applied threshold of +/- 1 log_2 FC. Red dashed line indicates a q-value of 0.05. Proteins with relation to septin/anillin filament formation are highlighted as light red dots and labeled with protein names. It is of note that all myelin septins (SEPT2, SEPT4, SEPT7, SEPT8) are reduced in myelin of *Anln* cKO mice compared to *Anln*$^{fl/fl}$ mice. ANLN is not depicted, as it is not detected in myelin of *Anln* cKO mice. (B) Differential myelin proteome analysis confirms genotype dependent expression of ANLN and CNP in myelin purified from *Anln*$^{fl/fl}$;*Cnp*$^{Cre/Wt}$-mice (*Anln* cKO) at P75. Note that ANLN was not detectable. Mean +/ SEM. n=3 animals per genotype; two-tailed unpaired t-test CNP p <0.0001. (**C**) Differential myelin proteome analysis reveals that septins (SEPT2, SEPT4, SEPT7, SEPT8) are more than 50% diminished in myelin purified from *Anln* cKO mice at P75 compared to *Anln*$^{fl/fl}$ mice. Further, RHOB and CDC42 are significantly reduced in myelin purified from *Anln* cKO-mice at P75. Mean +/ SEM. n=3 animals per genotype; two-tailed unpaired t-test SEPT4 p<0.0001; SEPT2 p<0.0001; SEPT8 p<0.0001; SEPT7 p<0.0001; ROHB p=0.0022; CDC42 p=0.0368. (**D**) Differential myelin proteome analysis reveals that classical myelin proteins are not affected. Mean +/ SEM. n=3 animals per genotype; two-tailed unpaired t-test. (**E**) Differential myelin proteome analysis reveals that all identified cytoskeletal proteins are not affected. Mean +/ SEM. n=3 animals per genotype; two-tailed unpaired t-test. Mass spectrometry was performed by Dr. Olaf Jahn and the proteomics unit of the MPI EM.

4.2.3 Loss of myelin septins upon conditional depletion of ANLN

To validate the results of the MS analysis, immunoblots were performed. Comparing lysate and purified myelin (Figure 13A), ANLN was only detectable in myelin and absent in *Anln* cKO mice. The smaller isoforms of SEPT8 are enriched in the myelin fraction and reduced in abundance in myelin of *Anln* cKO mice. MOG is loaded as a control for the myelin fraction and therefore, shows an increase in abundance in the myelin fraction. TUJ1, as an axonal marker, is strongly reduced in the myelin fraction. The abundance of CNS myelin septins was then further analyzed on purified myelin (Figure 13B). As expected, ANLN was not detectable in *Anln* cKO mice. Furthermore, all CNS myelin septins (SEPT2, SEPT4, SEPT7, SEPT8) were strongly reduced in abundance. ATP1A3 was loaded as control and exhibited no difference in abundance between controls (*Anln*$^{fl/fl}$) and *Anln* cKO mice. In a next step, classical myelin proteins were analyzed (Figure 13C). *Anln* cKO mice display a genotype dependent reduction of CNP of about 50%. All other tested myelin proteins (PLP, SIRT2, CD9, CA2) were unchanged. ATP1A1 was loaded as control and displayed no difference in abundance between controls (*Anln*$^{fl/fl}$) and *Anln* cKO mice.

Taken together, the results validate the data of the MS analysis. The genotype dependent depletion of ANLN is functional and results in a strong reduction of septins within the myelin fraction, whereas the abundance of myelin proteins is not affected.

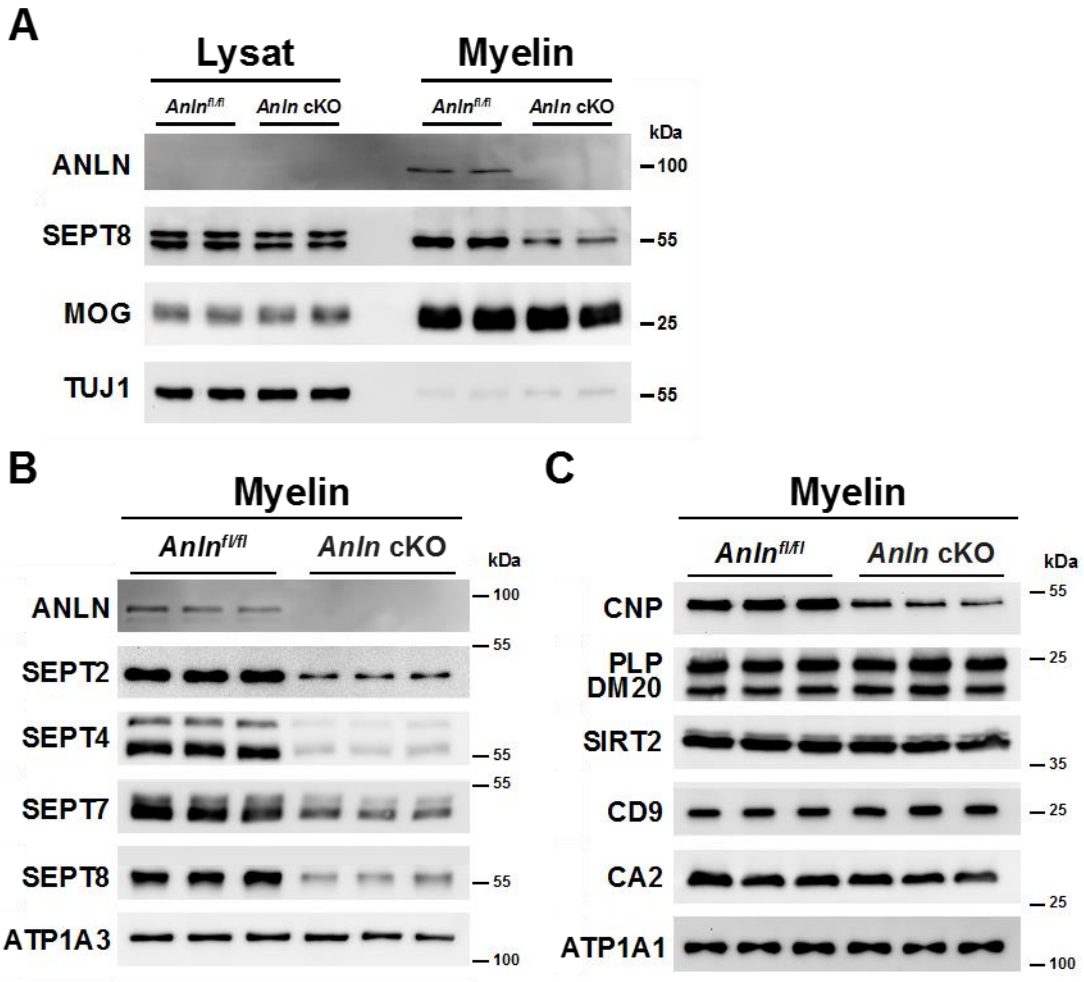

Figure 13: Abundance of ANLN, septins, and classical myelin proteins. (**A**) Immunoblot analysis of brain lysates and myelin purified from P75 control mice (*Anln*$^{fl/fl}$). ANLN is just detectable in purified myelin. MOG and TUJ1 were detected as controls. (**B**) Immunoblotting validates the lack of anillin (ANLN) and the strong reduction of myelin septins (SEPT2, SEPT4, SEPT7, SEPT8) in myelin purified from brains of *Anln* cKO mice. ATPase Na+/K+ transporting subunit alpha 3 (ATP1A3) was detected as a control. (**C**) Immunoblotting validates that classical myelin proteins are not affected in myelin purified from brains of *Anln* cKO mice. Of note is that CNP is reduced, genotype dependent, about 50%. ATPase Na+/K+ transporting subunit alpha 1 (ATP1A1) was detected as a control.

4.2.4 mRNA abundance of regulated proteins

To analyze whether proteins that were found to be downregulated on immunoblot level and/or downregulated within the MS data are also regulated on gene level or post-transcriptional, mRNA abundances were quantified using qRT-PCR (Figure 14). To do so, corpus callosi of control and *Anln* cKO (male and female) mice were dissected (n=6 per genotype) and analyzed. The quantification shows that the mRNAs of *Anln* (>98%) and *Cnp* (~50%) are downregulated depending on the genotype. Other quantified mRNAs (*Sept2, Sept4, Sept7, Sept8, RhoB, Cdc42*) were not altered, indicating that the reduction on protein level of these genes was due to post-transcriptional modifications. qRT PCRs were performed by Ursula Kutzke (MPI EM).

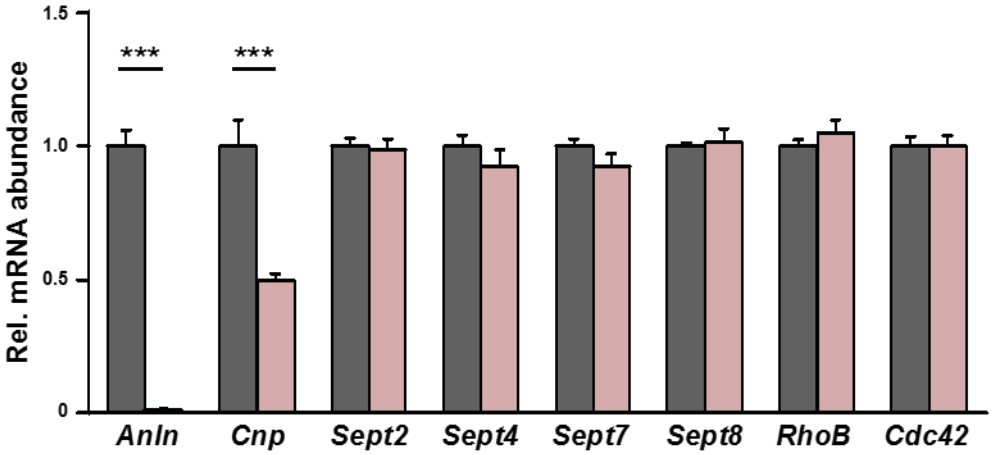

Figure 14: qRT-PCR analysis of regulated proteins. qRT-PCR to determine the abundance of *Anln*, myelin septins, *RhoB*, and *Cdc42* mRNAs in white matter (corpus callosum) of control (*Anln*$^{fl/fl}$) and *Anln* cKO mice. *Anln* and *Cnp* mRNA is significantly downregulated as expected due to the genotype. Note that myelin septins and *Cdc42* mRNAs were unaltered in abundance in *Anln* cKO mice compared to control mice (*Anln*$^{fl/fl}$). Mean +/ SEM. n=6 animals per genotype; two-way ANOVA; *Anln* p<0.0001; *Cnp* p<0.0001. qRT PCRs performed by Ursula Kutzke (MPI EM).

4.2.5 Myelin abnormalities

As it was previously shown that lack of the septin cytoskeleton in oligodendrocytes cause myelin outfoldings (Patzig et al., 2016), it was analyzed whether the detected reduction of ANLN and septins in *Anln* cKO mice lead to pathological myelin outfoldings. For analysis, electron micrographs of optic nerve cross sections at different time points (P14, P75, 6 mo, 8 mo) were analyzed. Figure 15A illustrates examples of myelin outfoldings in both, controls and *Anln* cKO mice, highlighted by dashed lines. The images already indicate that outfoldings in *Anln* cKO mice are more severe than in controls. The quantification (Figure 15B) reveals, that from P75 on, the % of area covered by myelin outfoldings is significantly higher in *Anln* cKO mice compared to controls. The area increases with age, suggesting a worsening of the phenotype.

To summarize, the results indicate that the loss of ANLN/septin filaments lead to the formation of myelin outfoldings.

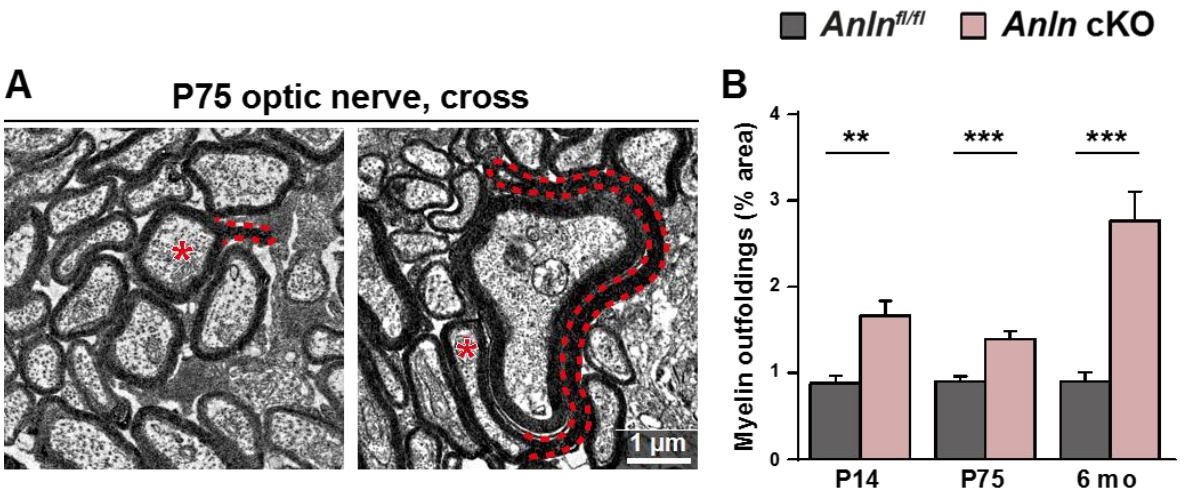

Figure 15: Lack of ANLN/septin filament causes myelin outfoldings. (**A**) Electron micrographs of optic nerves exemplify myelin outfoldings at P75. Dashed lines highlight myelin outfoldings; associated axons are marked with asterisks. (**B**) Quantitative evaluation of optic nerve electron micrographs reveals progressive myelin outfoldings in adult *Anln*$^{fl/fl}$;*Cnp*$^{Cre/Wt}$ mice (*Anln* cKO). Mean +/ SEM. n=4–6 animals per condition; two-tailed unpaired t-test P14 p=0.0076; P75 p=0.0009; 6mo p=0.0007.

4.2.6 Structure of myelin outfoldings

To get an overview of the structure and the size of myelin outfoldings, a 3D reconstruction of this pathological phenotype was generated from optic nerves of *Anln* cKO mice and respective controls at 5.5 mo of age by using FIB SEM (see also materials and methods section 3.2.9, performed by Dr. Anna Steyer (EM facility; MPI EM)). Figure 16A and 16A' illustrate 3D reconstructions of an *Anln*$^{fl/fl}$ optic nerve. Figure 16A depicts the reconstruction of one axon (blue), whereas A' also depicts the myelin (yellow) surrounding the axon. Figure 16B and 16C illustrate reconstructions of *Anln* cKO optic nerves. In the column B only one axon, which exhibits an outfolding is depicted, whereas in column C all axons exhibiting outfoldings are shown. In B' the length of the reconstructed outfolding was exemplary calculated, revealing a length of ~12 µm. In C' it can be seen that several axons exhibit myelin outfoldings and that these outfoldings occupy a considerable space.

The 3D reconstructions exhibit that the quantified outfoldings are neither hairpins, nor are they present along the whole internode. Furthermore, the reconstructions illustrate that myelin outfoldings occupy a considerable space, and therefore may have further impact on the functionality of axons.

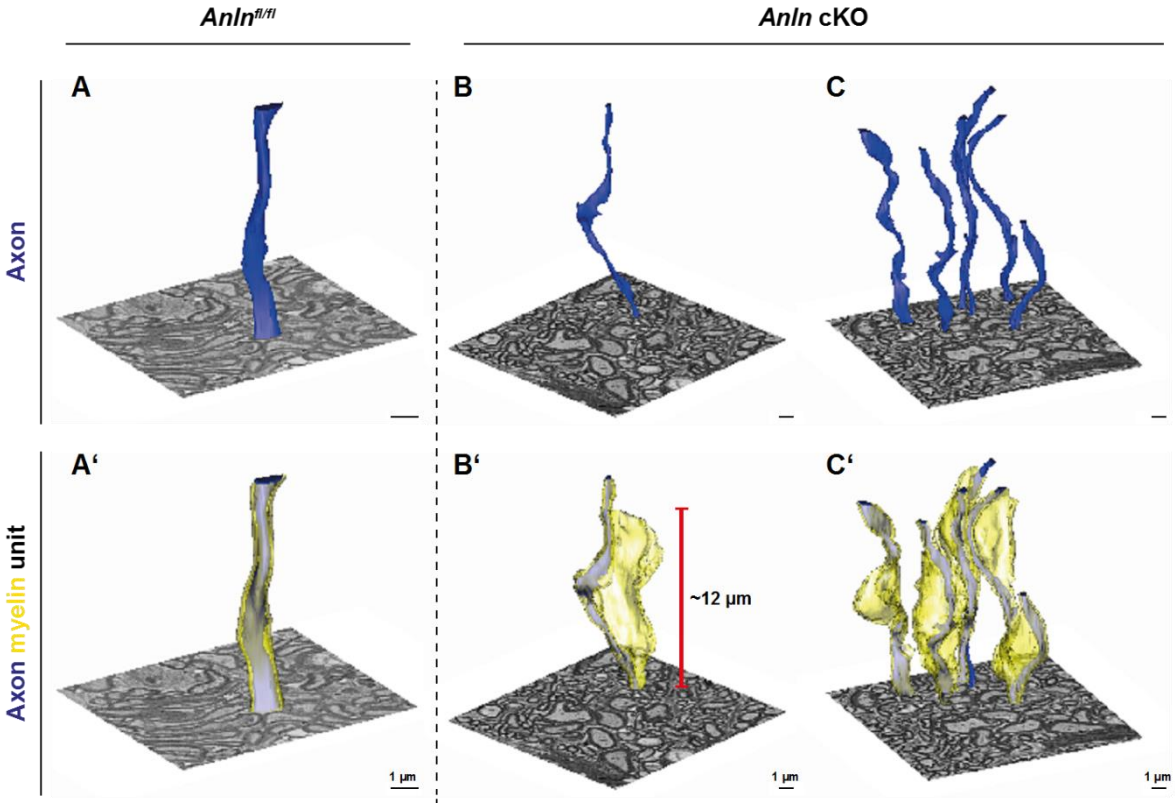

Figure 16: 3D reconstruction of myelin outfoldings. (**A-C**) 3D reconstructions of focused ion beam-scanning electron microscopy (FIB-SEM) micrographs displaying the plasma membrane of myelinated axonal segments (blue) and respective myelin sheaths (yellow) in the optic nerve of control (*Anln*$^{fl/fl}$) (**A, A'**) and *Anln* cKO (**B, B', C, C'**) mice at ~5.5 mo. The myelin sheath reconstructed in **A'** is tightly associated with the corresponding axon (**A, A'**) in the control nerve. An individual myelin outfolding (**B')** and the corresponding axon are reconstructed in **B,B'**. All myelin outfoldings in that same block (as in **B, B'**) were reconstructed in **C** with their corresponding axons (in **C, C'**)**.** It is of note that myelin outfoldings represent large sheets of compacted multilayered membrane stacks that extend considerably away from their respective myelinated axon, displaying longitudinal dimension of about 12 µm (indicated in **B'**). n=1 for each genotype. FIB SEM reconstructions were performed by Dr. Anna Steyer.

4.2.7 Decelerated nerve conduction velocity in *Anln* cKO mice

As described above, myelin outfoldings occupy a considerable space, which might result in a disrupted insulation of axons and thereby influencing nerve conduction velocity. To analyze, whether outfoldings might have an effect on the insulation and therefore on signal propagation, *in vivo* nerve conduction velocity measurements at the spinal cord were performed (Dr. Payam Dibaj, MPI EM). The measurements show a significantly decelerated nerve conduction velocity of about 15% in *Anln* cKO mice compared to controls (Figure 17A). As changes in nerve conduction velocity can also arise due to changes in the nodal structure (Arancibia-Carcamo et al., 2017), the nodal and paranodal organization was visualized by immunohistochemistry on longitudinal sectioned spinal cord cryosections and quantified using ImageJ (Figure 17B-G). The nodal density was quantified in Figure 17B, displaying equal amounts of nodes per µm² in controls and *Anln* cKO mice. In Figure 17C, an example of a node is depicted for each genotype. CASPR (green) is labeled to visualize the paranodes, whereas $Na_v1.6$ (red) is labeled to visualize the node. The images of the nodes display no structural changes in the nodal and paranodal organization in *Anln* cKO mice compared to controls. In the merge of the control, the measured parameters for the quantification are indicated. To quantify possible nodal changes, the nodal length was measured using ImageJ (Figure 17D). The quantification shows no difference between controls and *Anln* cKO mice in node length. For the paranode length quantification, both paranodes contacting a node were measured and the average was calculated for comparison of controls and *Anln* cKO mice. The quantification shows no difference between controls and *Anln* cKO mice (Figure 17E). Additionally, the ratio of node length to diameter (Figure 17F) and the ratio of paranode length to diameter (Figure 17G) were calculated and not found significantly altered between genotypes.

Accordingly, these results indicate a healthy and normal organization of the nodes, supporting the possible direct impact of myelin outfoldings on the nerve conduction velocity.

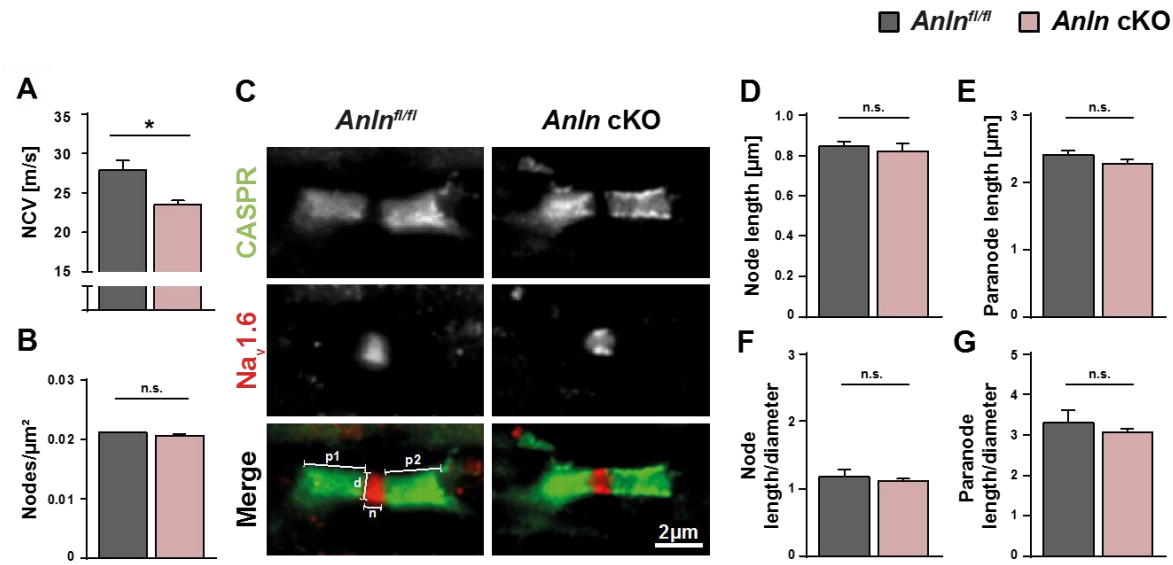

Figure 17: Nerve conduction velocity and node structure. (**A**) Electrophysiological measurement reveals decelerated nerve conduction in spinal cords of *Anln* cKO mice compared to controls (*Anln*$^{fl/fl}$) at 6 month of age. Mean +/ SEM. n=7-11 animals per genotype; two-tailed unpaired t-test (p= 0.0149). Nerve conduction velocity measurements were performed by Dr. Payam Dibaj (MPI EM). (**B**) Quantitative analysis of node density on longitudinal spinal cord sections of control (*Anln*$^{fl/fl}$) and *Anln* cKO mice at P75. Density of nodes is unchanged; not significant (n.s.) according to unpaired two-tailed t-test; n=4 animals per genotype; p= 0.1985. (**C**) Immunohistochemical detection of a marker of the nodes of Ranvier ($Na_v1.6$; sodium channels, red) and a paranodal marker (CASPR, green) on longitudinal spinal cord sections of control (*Anln*$^{fl/fl}$) and *Anln* cKO mice at P75. Merge of control depicts measured parameters for D-G. Note that the node organization is well preserved. p1 = paranode length1; p2 = paranode length2; d = diameter; n = node length. (**D**) Quantitative analysis of node length indicates a normal node structure control (*Anln*$^{fl/fl}$) and *Anln* cKO mice at P75. Not significant (n.s.) according to unpaired two-tailed t-test; n=4-5 animals per genotype; p= 0.6324. (**E**) Quantitative analysis of paranode length indicates a normal paranode structure in control (*Anln*$^{fl/fl}$) and *Anln* cKO mice at P75. Not significant (n.s.) according to unpaired two-tailed t-test; n=4-5 animals per genotype; p= 0.1927. (**F**) Quantitative analysis of the ratio of node length and diameter shows no difference between control (*Anln*$^{fl/fl}$) and *Anln* cKO mice at P75. Not significant (n.s.) according to unpaired two-tailed t-test; n=4-5 animals per genotype; p= 0.5966. (**G**) Quantitative analysis of the ratio of paranode length and diameter shows no difference between control (*Anln*$^{fl/fl}$) and *Anln* cKO mice at P75. Not significant (n.s.) according to unpaired two-tailed t-test; n=4-5 animals per genotype; p= 0.4603.

4.2.8 Unaltered brain structure and myelination in *Anln* cKO mice

Since myelin proteins within the MS data remained unchanged, the brain structure and overall myelination were analyzed. On paraffin embedded coronal brain sections (Figure 18A) and sagittal cerebellum sections (Figure 18A'), the overall myelination was visualized using Gallyas silver impregnation (performed by Annette Fahrenholz). In Figure 18A and A' it can be seen that the brain structure is unchanged between controls and Anln cKO mice. Furthermore, there are no changes in the overall myelination. To closer analyze the myelin ultrastructure, electron micrographs of control and *Anln* cKO optic nerve cross sections were compared (Figure 18B). Each image illustrates an axon and the corresponding compact myelin layers. The black lines indicate no difference in myelin periodicity between genotypes.

Taken together, the results indicate that oligodendrocytes, which lack ANLN, are capable of forming functional myelin.

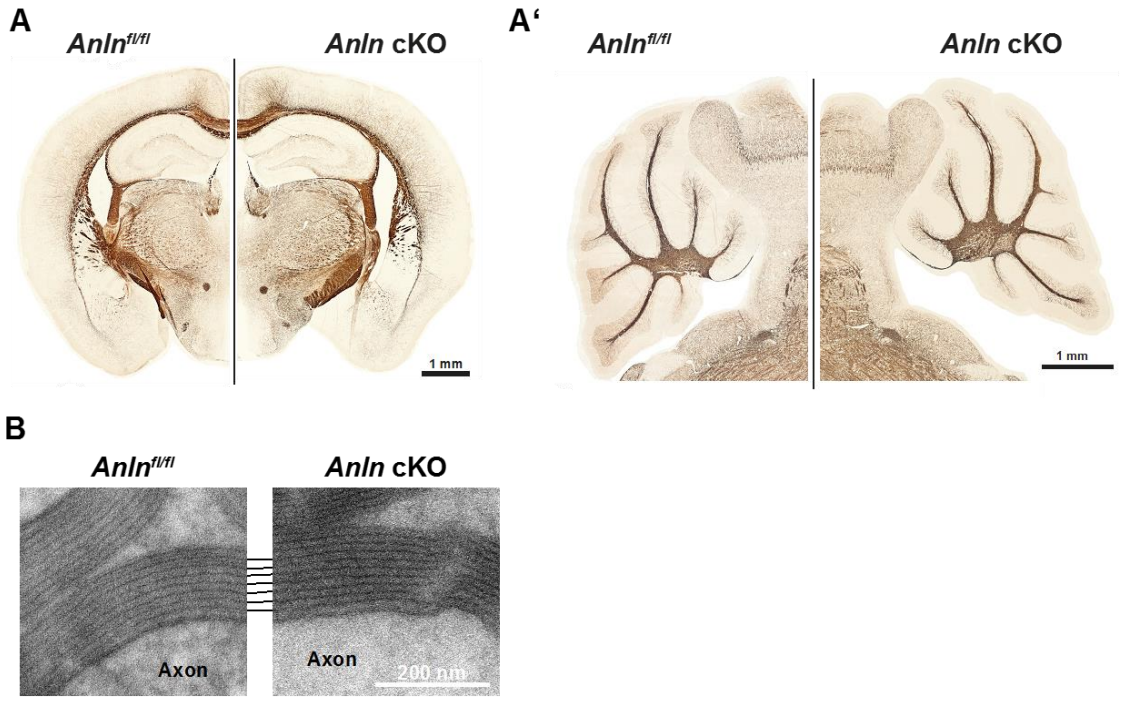

Figure 18: CNS myelination and myelin periodicity. (**A-A’**) Silver impregnation visualizes myelinated fiber tracts in mice lacking ANLN from myelinating cells (*Anln*$^{fl/fl}$;*Cnp*$^{Cre/Wt}$(*Anln* cKO)). In **A,** coronal sections are shown, whereas **A’** illustrates sagittal sections through the cerebellum. There are no changes in myelination in *Anln* cKO mice at P75 compared to control mice (*Anln*$^{fl/fl}$). Images are representative of three animals per genotype. (**B**) Electron micrographs of 8 month optic nerves display normal myelin periodicity and compaction in *Anln*$^{fl/fl}$ and *Anln* cKO mice. The two respective axons are indicated (Axon). Images are representative of three animals per genotype.

4.2.9 The loss of ANLN has no impact on myelin thickness

To further assess the ultrastructure of myelin in *Anln* cKO mice, the g-ratio was calculated. In this calculation, the Feret axonal diameter is divided by the Feret myelin diameter to assess the ratio of axon to myelin (Figure 19A; see also 3.2.8.6). The g-ratio analysis of axons in 6 mo optic nerve cross sections shows normal values in optic nerves of control animals as well as in *Anln* cKO mice (Figure 19A’), revealing normal myelin thickness throughout all axon diameters. In Figure 19A’’ every single g-ratio of each measured axon is depicted. It can be seen that there is no difference between genotypes.

To quantify the number of myelinated axons and percentage of degenerated/degenerating axons, electron micrographs of 6 mo optic nerve cross sections were analyzed. Figure 19B displays the mean number of myelinated axons per field (field = 220 µm²). The analysis depicts, that there is no difference in the number of myelinated axons between genotypes. The percentage of degenerated/degenerating profiles (Figure 19C) also exhibits no difference between genotypes.

The results indicate that oligodendrocytes lacking ANLN are able to myelinate axons in a normal state and that the lack of ANLN in oligodendrocytes has no effect on the integrity of axons.

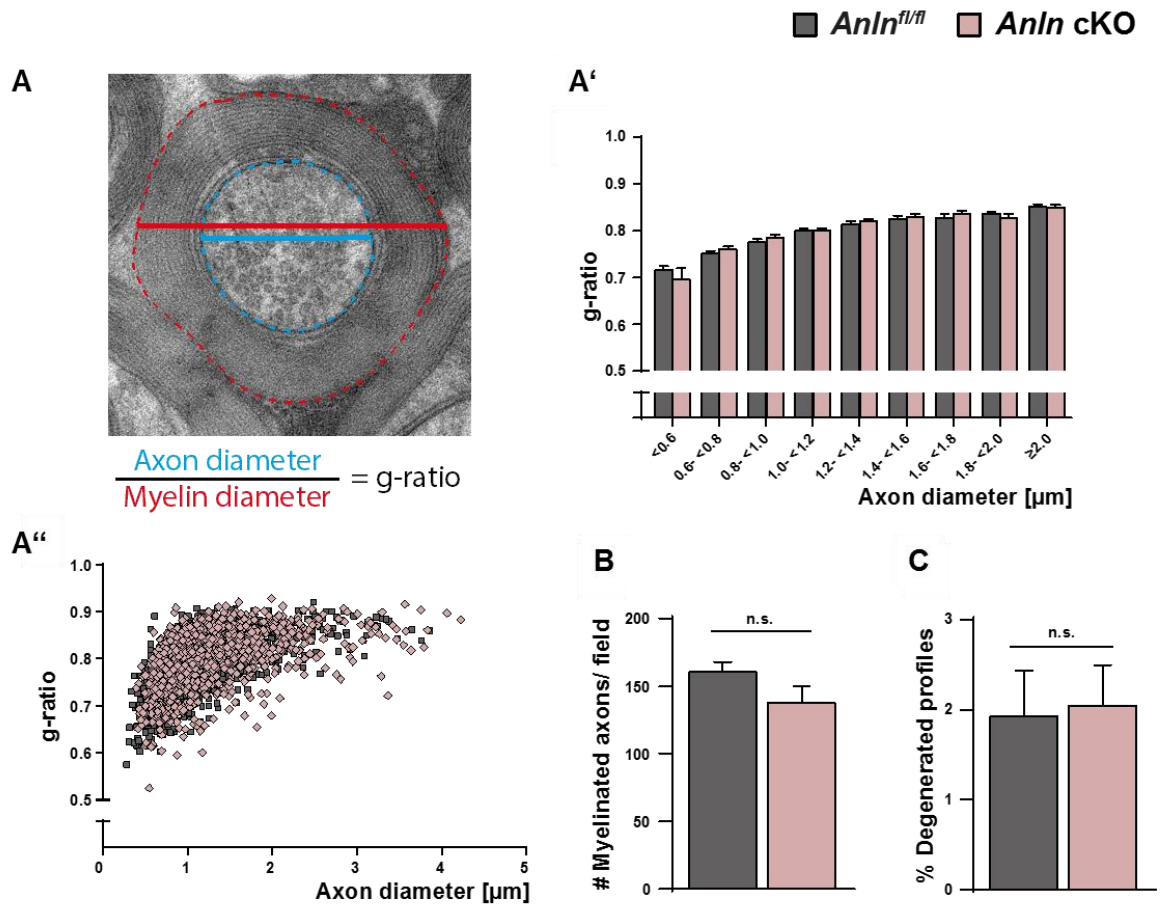

Figure 19: g-ratio and axon integrity. (**A**) Electron micrograph with schematic lines indicating the circumference (dashed line) and diameter (continuous line). Scheme illustrates the diameter of the axon (blue continuous line) and the diameter of the corresponding myelin (red continuous line), which are taken to calculate the g-ratio. (**A’-A’’**) g-ratio analysis of electron micrographs of optic nerves at 6 mo indicates normal myelin sheath thickness in *Anln* cKO mice. Mean +/ SEM. Not significant according to two-way ANOVA (p= 0.9279). (**B**) Quantitative evaluation of electron micrographs of optic nerves at 6 mo reveals a normal frequency of myelinated axons in *Anln* cKO mice. Mean +/ SEM. n=4-5 animals per genotype; not significant (n.s.) according to two-tailed unpaired t-test (p= 0.1827). (**C**) Quantitative evaluation of electron micrographs of optic nerves at 6 mo indicates the absence in *Anln* cKO mice of other myelin-related pathology such as degenerated axons. Mean +/ SEM. n=4-5 animals per genotype; not significant (n.s.) according to two-tailed unpaired t-test (p= 0.8664).

4.2.10 No signs of secondary neuropathology in CNS white matter

As mice, which lack ANLN from oligodendrocytes, develop myelin outfoldings and display decelerated nerve conduction velocity, it was analyzed if these alterations also affect the health of axons and other brain tissue. For this purpose, mice were perfused at P75 and coronal brain sections were labeled with neuropathological markers (labeling performed by Annette Fahrenholz). The analysis was performed in the fimbria, as described in the materials and methods section 3.2.7.7. In healthy conditions, amyloid beta precursor protein

(APP) is expressed in neurons and then further transported along the axon (Zheng and Koo, 2006). In pathological conditions of the axon, APP can accumulate and thereby indicates axonal degeneration (Coleman, 2005; Saxena and Caroni, 2007). In Figure 20A, the quantification of APP positive spheroids is shown as well as example images depicting a close up of the fimbria. Arrowheads indicate APP positive spheroids. There was no difference detectable between controls and *Anln* cKO mice. In pathological conditions of brains, it is also seen that astrocytes get activated microglia-dependent, as well as the other way around (Liddelow, 2017; Jo, 2017; Skripuletz, 2013). To test for possible astrogliosis, coronal brain sections were labeled with a glial fibrillary acidic protein (GFAP) antibody and the positive area was analyzed (Figure 20B). Figure 20B depicts respective images of the staining (GFAP) in the fimbria. It can be seen that there is no difference between control and *Anln* cKO mice at P75. Additional to astrogliosis, microgliosis is a commonly seen phenotype in pathological brains. Microglia react to changes in brain tissue and are able to phagocytose myelin debris (Cuzner, 1988; Mosley and Cuzner, 1996). Activated microglia that changed their morphology into amoeboid cells express the surface antigen MAC3 (Ho and Springer, 1983; Giulian and Baker, 1986). To assess the area covered by activated microglia, coronal brain sections were labeled with a MAC3 antibody (Figure 20C). There were no signs of increased numbers of activated microglia in *Anln* cKO mice compared to controls. Further, all microglia were labeled with an antibody against IBA1 (Figure 20D). Although the area positive for IBA1 was slightly increased in *Anln* cKO mice, the difference was not significant.

To sum up, the results show no signs for axonopathy, astrogliosis, and microgliosis, when oligodendrocytes lack ANLN. These observations indicate, that the loss of the ANLN/septin filament, coinciding with myelin outfoldings and decelerated nerve conduction velocity, do not cause further neuropathological abnormalities.

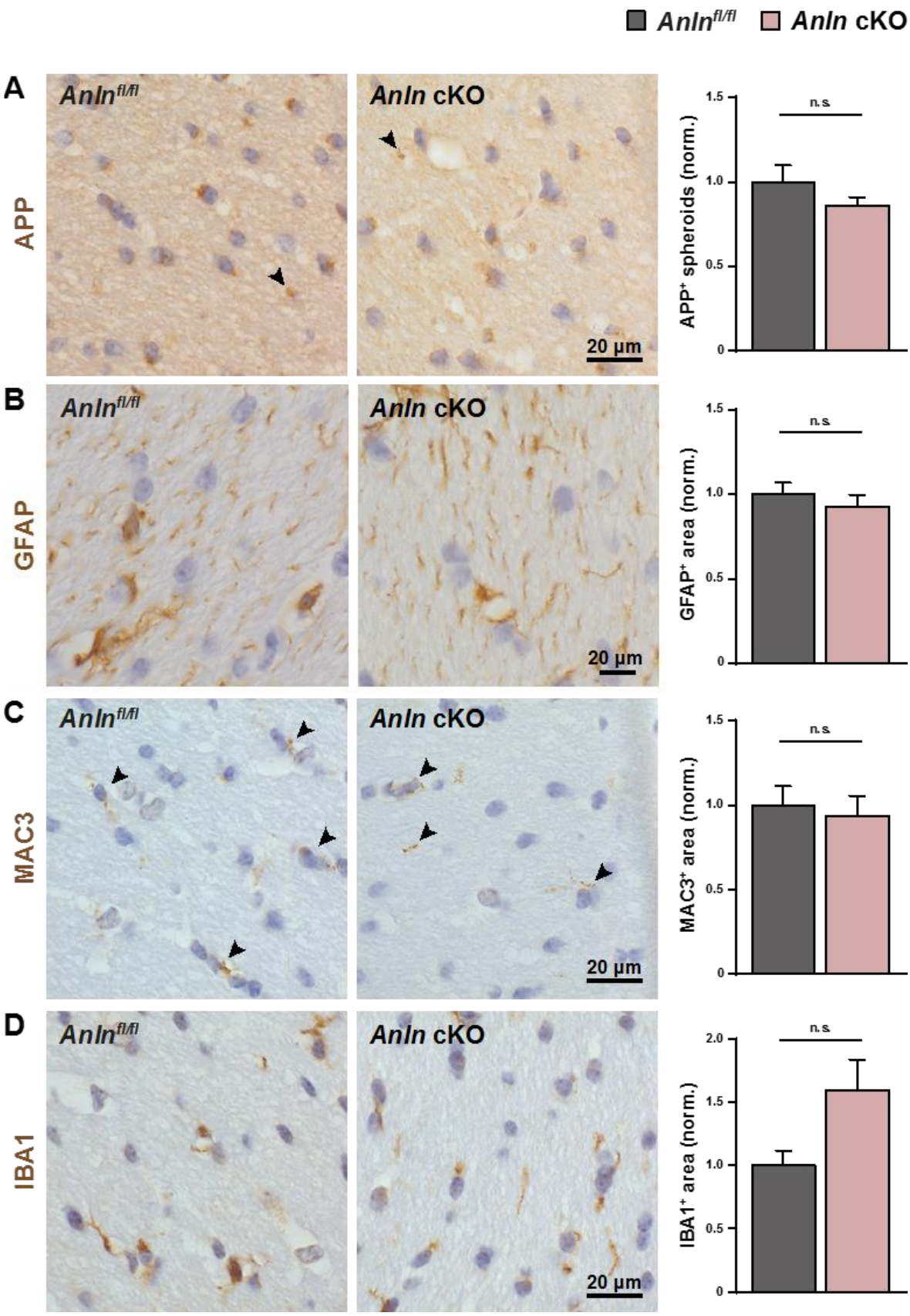

Figure 20: Lack of ANLN in oligodendrocytes does not lead to secondary neuropathology. (**A**) Immunohistochemical analysis of APP positive spheroids in the white matter (hippocampal fimbria) of control (*Anln*$^{fl/fl}$) and *Anln*$^{fl/fl}$;*Cnp*$^{Cre/Wt}$ mice (*Anln* cKO) at P75. The labeling is similar in control and *Anln* cKO mice. Not significant (n.s.) according to unpaired two-tailed t-test; n=5 animals per genotype; p= 0.2418. (**B**) Immunohistochemical analysis of GFAP-immunopositivity in the white matter (hippocampal fimbria) of control

(*Anln*$^{fl/fl}$) and *Anln* cKO mice at P75. The labeling is similar in control and *Anln* cKO mice. Not significant (n.s.) according to unpaired two-tailed t-test; n=5 animals per genotype; p= 0.4704. (**C**) Immunohistochemical analysis of MAC3-immunopositivity in the white matter (hippocampal fimbria) of control (*Anln*$^{fl/fl}$) and *Anln* cKO mice at P75. The labeling is similar in control and *Anln* cKO mice. Not significant (n.s.) according to unpaired two-tailed t-test; n=5 animals per genotype; p= 0.7047. (**D**) Immunohistochemical analysis of IBA1-immunopositivity in the white matter (hippocampal fimbria) of control (*Anln*$^{fl/fl}$) and *Anln* cKO mice at P75. The labeling is similar in control and *Anln* cKO mice. Not significant (n.s.) according to unpaired two-tailed t-test; n=5 animals per genotype; p= 0.0593.

4.2.11 *Anln* cKO mice display reduced PIP_2 levels

It is known that ANLN is able to bind PIP_2 via a PH (pleckstrin homology) domain at the C-terminal. Furthermore, it was shown that binding of ANLN to PIP_2 promotes septin filament assembly *in vitro* (Kinoshita et al., 2002, Liu et al., 2012). To see, if the loss of ANLN in oligodendrocytes also affects the PIP_2 levels, purified myelin was analyzed in collaboration with Prof. Dr. Ingo Heilmann (Halle, Germany). The gas chromatographic analysis reveals a significant reduction of about 50% in purified myelin of *Anln* cKO mice compared to controls at P75. The result suggests that ANLN may also has a stabilizing effect on PIP_2.

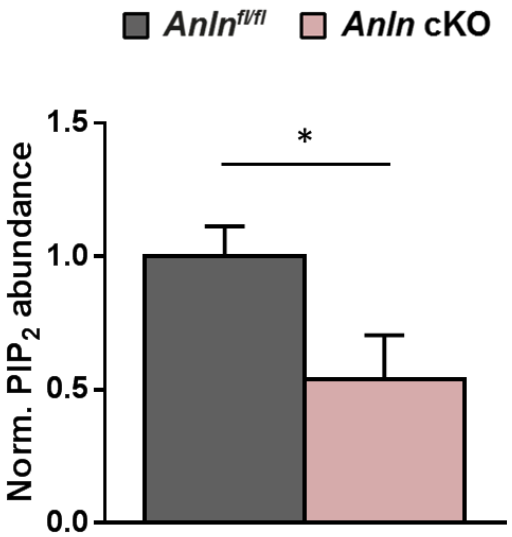

Figure 21: PIP_2 analysis in *Anln* cKO and control mice. Quantification of PIP_2 in purified myelin. The analysis indicates decreased levels of PIP_2 in *Anln* cKO mice compared to controls (*Anln*$^{fl/fl}$) at P75. Mean +/ SEM. n=6 animals per genotype; two-tailed unpaired t-test; p=0.0435. Gas chromatography was performed by Prof. Dr. Ingo Heilmann (Halle, Germany).

4.2.12 Axon diameter frequency distribution

The loss of the ANLN/septin filament leads to an instability of myelin sheaths in the CNS, resulting in myelin outfoldings. To see whether the loss of myelin stability and the altered PIP_2 levels lead to axonal changes, axon diameters were analyzed at P75 and 6 mo of age in control and *Anln* cKO optic nerves (Figure 22). Quantification was done on EM images using ImageJ as described in the materials and methods section 3.2.8.6. Figure 22A depicts the relative frequency of indicated axon diameter at P75 in optic nerves of controls and *Anln* cKO mice. The bar graph indicates a trend towards larger axon diameters, but

statistical comparison of all axon diameters with the Kolmogorov Smirnov test shows no significant difference. Since the myelin outfolding phenotype is aggravated by aging, the axon diameter frequency distribution was also analyzed at 6 mo of age (Figure 22B). The relative frequency of indicated axon diameters, again, depicts larger axon diameters in *Anln* cKO mice. By comparing all axon diameters, the Kolmogorov Smirnov test shows a highly significant shift towards larger axon diameters.

This result raises the possibility that the loss of the ANLN/septin filament in CNS myelin has an effect on axon diameters, suggesting that the stability of intact myelin restricts axon diameters.

For further analysis, axon diameters were also quantified in *Sept8*$^{null/null}$ and *Sept8*$^{fl/fl}$*;Cnp*$^{Cre/Wt}$ mice at 6 mo of age (Figure 23A and B). As these mice also lack the ANLN/septin filament, the same phenotype should be present. Figure 23A displays the relative frequency of indicated axon diameters for *Sept8*$^{null/null}$ mice. In these mice, no difference between controls and *Sept8*$^{null/null}$ mice was observed. By statistical evaluation of all axon diameters using the Kolmogorov Smirnov test, the whole distribution exhibits no significant difference. Moreover, in *Sept8*$^{fl/fl}$*;Cnp*$^{Cre/Wt}$ mice the axon diameter frequency distribution was analyzed (Figure 23B). The bar graph illustrates the relative frequency of indicated axon diameters. Similar to *Anln* cKO mice, a shift towards larger axon diameters can be seen. Using the Kolmogorov Smirnov test, the axon diameters distribution exhibits a highly significant shift towards larger axon diameters.

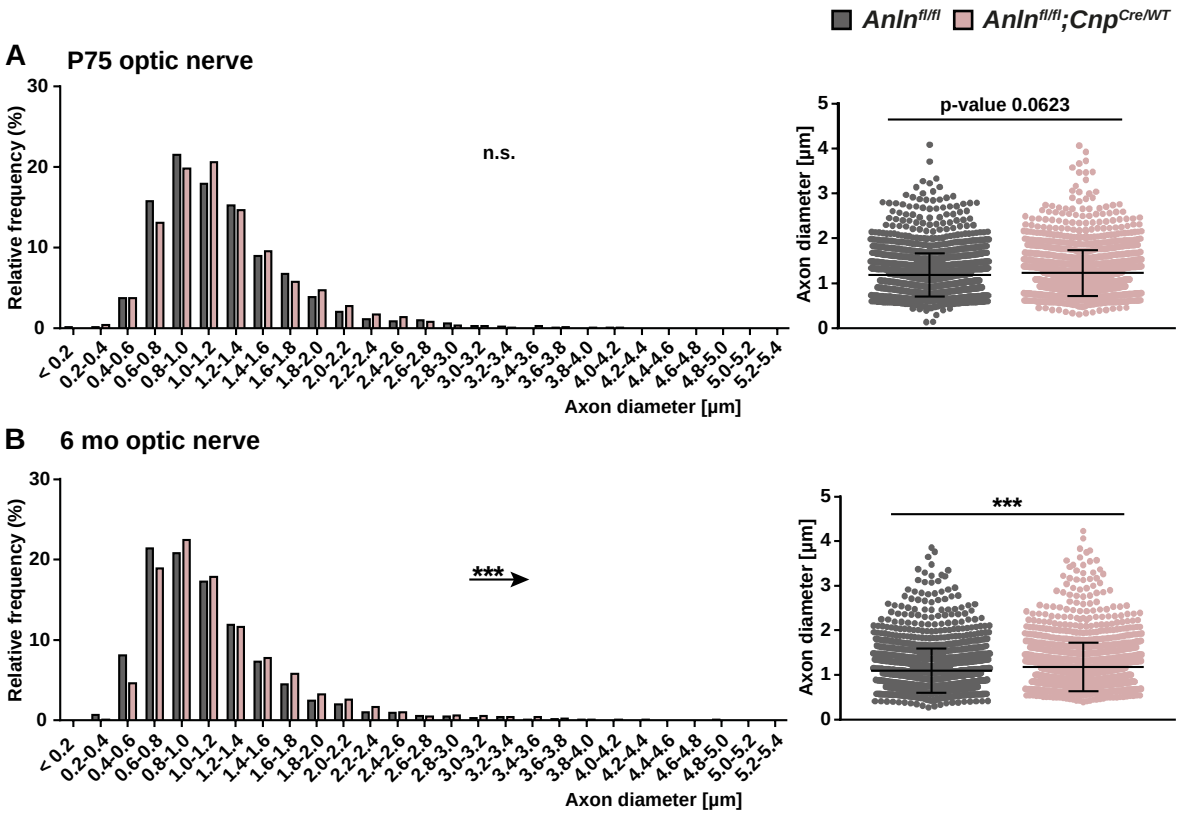

Figure 22: Axon diameter frequency distribution in *Anln* cKO mice. (**A**) Frequency distribution analysis of optic nerve myelinated axons of electron micrographs at P75 indicates a slight trend towards larger axon diameter in *Anln* cKO mice. n=5 animals per genotype. Not significant according to Kolmogorov Smirnov test (p= 0.0623). (**B**) Frequency distribution analysis of optic nerve myelinated axons of electron micrographs at 6 mo of age indicates a shift towards larger axon diameter in *Anln* cKO mice. n=5 animals per genotype. Significant according to Kolmogorov Smirnov test (p= 0.0008).

The results depict only a shift towards larger axon diameters in conditional mutants, which harbor half of the CNP dosage. To clarify if the observed phenotype is due to CNP heterozygosity, $Cnp^{Cre/Wt}$ mice were analyzed at 6 mo of age (Figure 23C). The axon diameter distribution shows no difference between controls and $Cnp^{Cre/Wt}$ mice, also indicated by the analysis of all axon diameters with the Kolmogorov Smirnov test.

The results presented in Figure 23C indicate that the lack of the ANLN/septin filament from CNS myelin possibly results in larger axon diameters, and not the CNP heterozygosity alone. Furthermore, the results display a possible new role of myelin in axon diameter restriction.

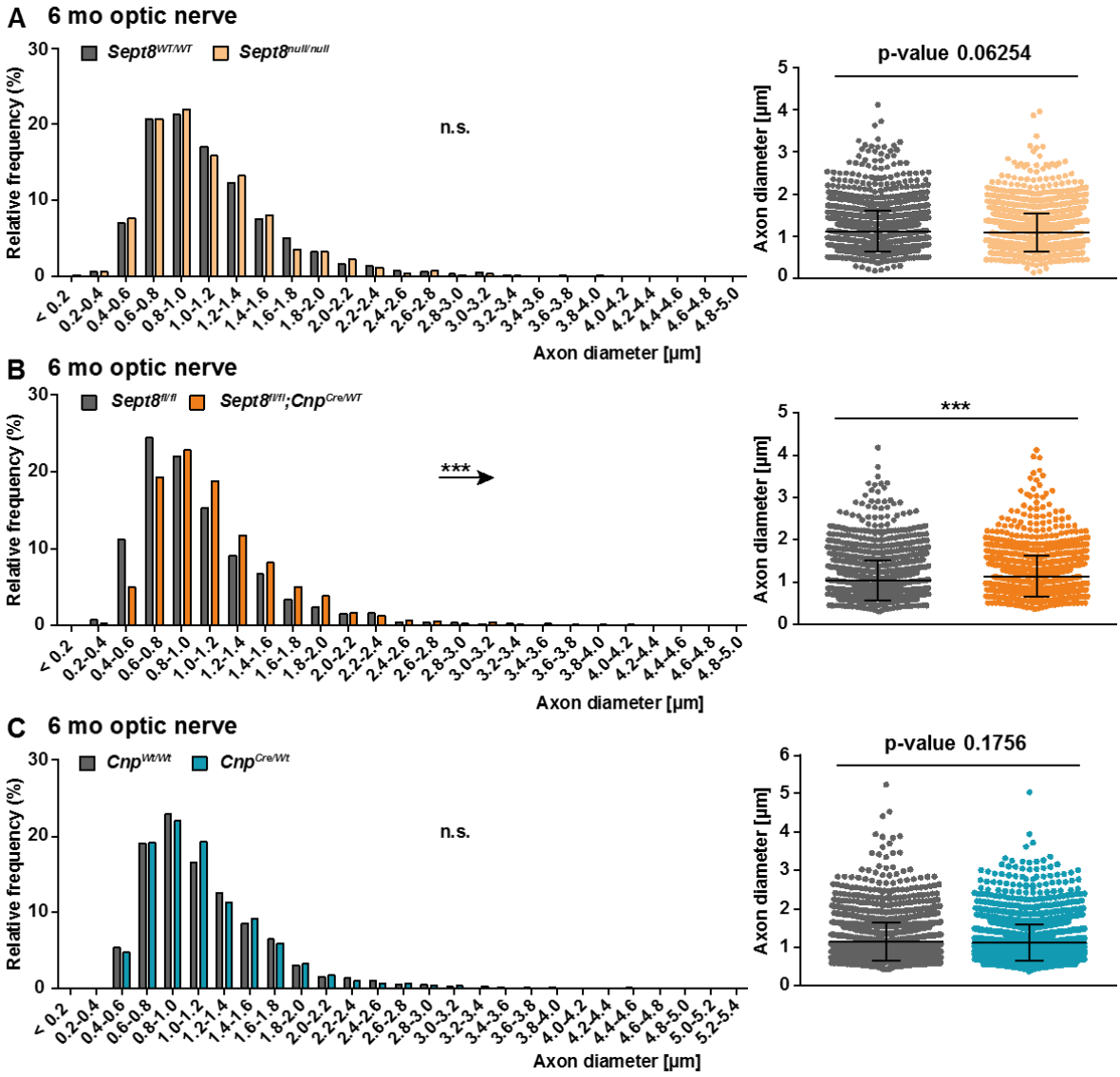

Figure 23: Axon diameter frequency distribution in SEPT8 deficient and *Cnp*$^{Cre/Wt}$ mice. (**A**) Frequency distribution analysis of optic nerve myelinated axons of electron micrographs at 6 mo of age indicate a slight trend towards larger axon diameter in *Sept8*$^{null/null}$ mice. n=5 animals per genotype. Not significant according to Kolmogorov Smirnov test (p= 0.06254). (**B**) Frequency distribution analysis of optic nerve myelinated axons of electron micrographs at 6 mo of age indicate a shift towards larger axon diameter in *Sept8*$^{fl/fl}$;*Cnp*$^{Cre/Wt}$ mice. n=5 animals per genotype. Significant according to Kolmogorov Smirnov test (p= <0.0001). (**C**) Frequency distribution analysis of optic nerve myelinated axons of electron micrographs at 6 mo of age indicate no shift towards larger axon diameter in *Cnp*$^{Cre/Wt}$ mice. n=5 animals per genotype. Not significant according to Kolmogorov Smirnov test (p= 0.1756).

5 Discussion

5.1 Is ANLN influencing septin filament assembly?

In previous studies, septin filaments and anillin were shown to be associated with each other. For example, studies in yeast have shown that ANLN and septins co-localize within the cleavage furrow and thereby, enable proper cell division (Maddox et al., 2007, Oegema et al., 2000, Renshaw et al., 2014). Furthermore, *in vitro* studies have shown that ANLN acts as an adaptor to recruit septins onto membranes and that ANLN enhances PIP_2-mediated septin filament formation (Kinoshita et al., 2002, Liu et al., 2012), suggesting that septin filament formation relies on anillin. *In vivo*, it was shown that anillin also relies on septins, as the loss of septin filaments in CNS myelin led to a reduction of ANLN on protein level (Patzig et al., 2016). The reduction of ANLN was also seen in other tested mutants, which show reduced levels of myelin septins (Patzig et al., 2016). These results indicate that ANLN not only promotes septin filament formation, but also interacts with the filament to stabilize adaxonal myelin. To test whether ANLN serves a crucial function in myelin septin filament assembly *in vivo*, beyond its mere association with myelin septins, a novel line of mouse mutants (*Anln*$^{flox/flox}$;*Cnp*$^{Cre/Wt}$ mice) was generated and analyzed. The presented results illustrate that the loss of ANLN from mature oligodendrocytes leads to a strong reduction of septins on protein level (Figure 12C and 13B). Moreover, as the mRNA abundance of septins is unaltered in *Anln* cKO mice (Figure 14), it is unlikely that the reduction is due to transcriptional regulation. It was shown that ANLN has a stabilizing function during cytogenesis (Liu et al., 2012), suggesting that ANLN could also stabilize the septin filament, thereby probably preventing its degradation. Another possibility is that ANLN facilitates septin filament formation, as it was shown that anillin enhances PIP_2-mediated septin filament formation *in vitro* (Kinoshita et al., 2002, Liu et al., 2012). Septin monomers and ANLN likely get degraded, if they are not incorporated into a filament (Patzig et al., 2016). The presented results suggest that the reduced septin abundance is caused by degradation of septin monomers. This could be either due to a loss of stability of the filament, or due to a hindered filament assembly.

To further test the influence of ANLN on septin filaments, it would be interesting to immunohistochemically visualize septin filaments in *Anln* cKO mice. By this, it could be analyzed if the septin filaments are altered in abundance or length due to the lack of ANLN. Based on the assumption that ANLN stabilizes the septin filament or facilitates septin filament assembly, it is likely that the abundance and length of the septin filaments are altered. The effect of ANLN on septin filament assembly could also be investigated by generating an ANLN overexpressing mouse line. It would be also interesting to analyze if ANLN would further enhance/stabilize the septin filament assembly, possibly leading to more abundant and longer filaments, which might further stabilize the myelin.

It was reported that the loss of CNS myelin septin filaments lead to myelin outfoldings (Patzig et al., 2016). This could be confirmed in the presented study, as it is illustrated in Figure 15. As septins are also less abundant upon aging (Patzig et al., 2016), it would be interesting to test in ANLN overexpressing mice if the overexpression of ANLN could rescue the loss of the ANLN/septin filament in old mice. As the loss of the ANLN/septin filament coincides with myelin outfoldings and reduced nerve conduction velocity (Patzig et al., 2016) (Figure 17A), a rescue of the ANLN/septin filament might prevent these pathological phenotypes in aging.

5.2 ANLN/septin filaments in development - who comes first?

In several studies, it was shown that ANLN interacts with septins (Patzig et al., 2016, Liu et al., 2012, Renshaw et al., 2014, Kinoshita, 2003), but so far there is less known about the (developmental) expression chronology of these proteins. In *Candida albicans*, it was shown that the anillin-related Int1 and the Sep7 septin interact with each other during cytokinesis (Orellana-Munoz et al., 2018). Interestingly, the authors have presented, that the septin ring assembly occurred before the incorporation of Int1, suggesting that possibly the septin filament is build first and then stabilized by ANLN. In the presented data, it could be shown in immunoblots of P15, P18, P21, and P24 purified myelin that the abundance of ANLN and myelin septins have a similar chronology (Figure 10B). These results are in accordance with the immunoblot analysis in Patzig et al. (2016), where similar increasing abundances of septins were detected. Furthermore, in the results regarding the immunohistochemical analysis of P15, P21, and P28 optic nerves, it was shown that ANLN and SEPT8 are similar distributed and show a similar protein expression chronology (Figure 10A). It was seen that each filament-like labeling was positive for ANLN and SEPT8, and that the number of labeled filament-like structures increased from P21 to P28. Interestingly, filament-like labeling was detectable at P21, whereas in Patzig et al. (2016) no labeling was detectable at this time point. This result suggests, that the protein expression of septins is probably adjusted to the local needs of the axon and that there is a longer time frame of ANLN/septin arising. Unfortunately, the results did not shed light on the question whether ANLN or septins evolve first. To further analyze this question, it would be necessary to look at smaller time intervals like P19, P20, P21, and P22 in optic nerve longitudinal sections. Also, the immunoblot analysis of purified myelin could be adjusted, and earlier time points could be analyzed. Another possibility would be the usage of microfluidic chambers to model CNS myelination (Vaquie et al., 2018). In this system, the protein expression chronology of ANLN and septins could be analyzed in more detail using live-cell imaging techniques. In this experiment, it has to be considered that in oligodendroglial cultures, it was not possible to detect the formation of filament-like

structures of septins (unpublished data). This could be due to too short incubation time, but also due to using an *in vitro* system, as it was detected that the adaxonal myelin layer, to which septins localize, is not modeled in oligodendroglial cultures. Furthermore, it was shown that septin filament formation arises in late stages of myelination. This mature state of an oligodendrocyte might not be reached in an *in vitro* system.

5.3 Do myelin outfoldings decrease nerve conduction velocity?

Myelin is known to increase nerve conduction velocity by blocking internodal current leakage and decreasing the transverse capacitance between the inside and outside of a nerve fiber (Hartline and Colman, 2007). The increased membrane resistance enables an increased velocity of signal propagation. With the so-called saltatory signal propagation, the NCV is increased from 10 m/sec up to 150 m/sec. It is proposed that electrical sealing through two opposed membranes is playing a crucial role in decreasing the transverse capacitance and proportionately speeds impulse propagation along it. It is suggested that the sealing can be achieved by narrowing the conductive space between adjacent axonal and glial membranes, which means the cytoplasmic or extracytoplasmic space (Hartline and Colman, 2007). As depicted in Figure 17A, *Anln* cKO mice exhibit a decelerated nerve conduction velocity of about 15% in spinal cord compared to controls. Moreover, these mutants display specifically myelin outfoldings due to the lack of the ANLN/septin filament. 3D reconstruction of *Anln* cKO optic nerves illustrated that several axons exhibit myelin outfoldings (Figure 16C'). Another study estimates that if 6.5% of myelinated axons display myelin outfoldings of an average 10 µm length, at least half of the myelinated segments probably have myelin outfoldings (Snaidero et al., 2014). Other studies showed similar results of reduced NCV in other mouse mutants, which exhibit myelin outfoldings and lack the ANLN/septin filament. For example, $Sept8^{fl/fl};Cnp^{Cre/Wt}$ mice showed a decelerated nerve conduction velocity of about 20% in the spinal cord and depicted specifically myelin outfoldings (Patzig et al., 2016). Further, NCV measurements in mice showing more complex pathology ($Cnp^{null/null}$, $Mag^{null/null}$, and $Plp^{null/null}$), including reduced ANLN/septin filament abundance and therefore also myelin outfoldings, indicated decelerated NCV in the spinal cord (unpublished data). In Patzig et al. (2016), it was suggested that myelin outfoldings impede the current flow along myelinated fibers and thereby, leading to the identified deceleration, keeping in mind that other unidentified secondary effects could also contribute to the deceleration. Moreover, it was shown that in optic nerves of PLP mutants the NCV is also reduced (Gutierrez et al., 1995). There it was suggested that the loosely packed myelin sheaths of PLP mutants lead to a functional deficit in conduction velocities of central fibers. The authors have shown that the measured NCV in developmental nerves is also reduced. This leads to the assumption that only complete myelination gives the basis

for normal NCV (Gutierrez et al., 1995). Keeping in mind that also other factors could have an influence on NCV (Wu et al., 2012, Arancibia-Carcamo et al., 2017), the nodal structure and density was analyzed in the presented study (Figure 17B-G). The results display no alterations in the nodal structure, as well as in the node density, which is associated with the internode length (Ford et al., 2015). Thus, according to the presented data, decelerated NCV may be caused by myelin outfoldings, as the nodal and internodal structure is normal. Hypothetically, myelin outfoldings could provoke the lack of proper insulation and reduced membrane resistance along the axon, due to more cytoplasm along the space where the myelin folds out. This would lead to a partially lower membrane resistance where an increased transmembrane current could take place. That would result in a regional cation leak out, so that less cations would be available to depolarize other parts of the membrane. This would mean a slowdown of signal propagation. Considering the estimation that half of the myelinated segments display myelin outfoldings, the presented results strengthen the possibility of myelin outfoldings impeding signal propagation, even though other unidentified secondary effects could possibly contribute to the decelerated NCV. To directly test whether outfoldings reduce NCV, it would be necessary to patch an axon with an outfolding and record NCV. It is possible to measure NCV *ex vivo* in optic nerves, but it would be necessary to identify a single axon with a myelin outfolding and directly measure its NCV. Although it is possible to patch single axons, the identification of a myelin outfolding is not feasible, as in light microscopic applications, it was not possible to identify myelin outfoldings by labeling myelin. Up until now, the available techniques are not feasible to record NCV from single axons with previously identified myelin outfoldings.

5.4 Does loss of ANLN lead to altered PIP_2 levels in CNS myelin?

Several studies report that ANLN, PIP_2, and septins are associated with each other (Liu et al., 2012, Zhang et al., 1999, Bertin et al., 2010, Joberty et al., 2001, Patzig et al., 2016). It was shown that PIP_2 head groups bind ANLN to recruit it to the cleavage furrow *in vitro* (Liu et al., 2012). Another *in vitro* study reported that PIP_2 recruits mammalian SEPT4 onto the plasma membrane (Zhang et al., 1999). Furthermore, it was shown that PIP_2 mediates submembranous septin filament polymerization in yeast (Bertin et al., 2010). In an *in vivo* model, it was shown that lack of PTEN in oligodendrocytes results in reduced PIP_2 levels. This leads to reduced protein abundance of septins and ANLN, including increased myelin outfoldings besides other pathologies (Patzig et al., 2016, Goebbels et al., 2010). So far, PIP_2 seems to affect myelin septin assembly via ANLN. The results illustrated in Figure 21 show reduced PIP_2 levels in purified myelin of *Anln* cKO mice compared to controls. This leads to the assumption that ANLN also has a role in PIP_2 stabilization, possibly by binding to the head groups and thereby hindering modifications of PIP_2. A possible modification is

the conversion of PIP_2 to PIP_3 via PI3K. Thus, it would be interesting to analyze PIP_3 levels in *Anln* cKO mice. As high levels of PIP_3 induce active net growth of myelin sheaths via the Akt/mTOR pathway, it would be of further interest to analyze the pathway in more detail. One possibility would be an immunoblot analysis of purified myelin, testing the phosphorylation state of Akt and Erk, which are downstream effectors of PI3K.

5.5 Myelin stability; a novel effector of axon diameter restriction?

It is known that the axon diameter is influenced by several factors, e.g. radial growth of axons is promoted by myelination due to modulation of the phosphorylation of neurofilaments (NF) at internodes (Hsieh et al., 1994). The modulation leads to larger interfilament spacing, which coincides with an increased number of neurofilaments, resulting in larger axon diameters. The phosphorylation of NF-medium and NF-heavy, was also shown to play an important role in axonal diameter regulation (Garcia et al., 2003). Furthermore, it was shown that *MBP*$^{null/null}$ (shiverer) mice, in which oligodendrocytes only wrap loose layers around axons, resulting in little or no compact myelin (Readhead et al., 1987), exhibit smaller axon diameters. This reduction in axon diameters is caused by changes in microtubule stability and density (Kirkpatrick et al., 2001). In the illustrated results, it was shown that *Anln* cKO and *Sept8*$^{fl/fl}$*;Cnp*$^{Cre/Wt}$ mice display increased axon diameter at 6 mo of age (Figure 22B and 23B). Interestingly, this phenotype was only present in combination with CNP heterozygosity. CNP was reported to prevent premature closure of cytoplasmic channels in CNS myelin (Snaidero et al., 2014). These channels could provide transport routes, for example, for metabolites into the adaxonal myelin layer (Nave and Werner, 2014). The result leads to the suggestion that impairment of the ANLN/septin filament in CNS myelin together with premature closure of cytoplasmic channels leads to altered axon diameters. So far, the mechanism behind the increase is unclear. One speculative suggestion would be that oligodendrocytes form compact myelin, which is stabilized by the ANLN/septin filament, around axons and thereby give a spatial limitation due to the stable and robust ensheathment. To test if the CNP heterozygosity plays a role in this hypothesis, it would be needed to analyze *Sept8*$^{null/null}$*;Cnp*$^{Cre/Wt}$ mice, as *Sept8*$^{null/null}$ mice did not display enlarged axon diameters (Figure 23A and C). This indicates that the loss of the ANLN/septin filament and consequently also the loss of myelin stability alone does not lead to increased diameter. Further taking into account that mice lacking compact myelin (shiverer) show a decrease in axon diameter, although they face no spatial limitation through compact myelin, indicates that the regulation is much more complex. This coincides with the finding that the maturation of the axonal cytoskeleton is not functional in shiverer mice as compact myelin plays a crucial role in this maturation (Brady et al., 1999). Additionally, it was shown that phosphatidylinositol phosphates, including PIP_2, interact with

neurofilaments (Kim et al., 2011), which are known to regulate axon diameter (Garcia et al., 2003). This suggests that the identified altered PIP_2 levels in *Anln* cKO mice (Figure 21) could also contribute to the observed increase in axonal diameter. To further analyze this, it would be interesting to analyze PIP_2 levels in $Sept8^{null/null}$, $Sept8^{fl/fl};Cnp^{Cre/Wt}$, and $Cnp^{Cre/Wt}$ mice, to see if there is a correlation between enlarged axon diameters and altered PIP_2 levels. Another important analysis would include an assessment of neurofilaments in mutants, which display altered axon diameter, as neurofilaments are involved in axon diameter regulation. Taken together, the *Anln* cKO mouse might not be the perfect model to study axon diameter regulations, but may provide a new possible functionality of oligodendrocyte compact myelin for axons. To see whether stability provided by the ANLN/septin filament contributes to the axon growth via a spatial limitation, it would be interesting to analyze axon diameter in mice which express ANLN and septins earlier in development, to see if an earlier gained stability would restrict axonal growth to a certain extend.

6 References

ALBERTS, B. 2002. *Molecular Biology of the Cell, 4th edition* [Online]. New York: Garland Science.

ARANCIBIA-CARCAMO, I. L., FORD, M. C., COSSELL, L., ISHIDA, K., TOHYAMA, K. & ATTWELL, D. 2017. Node of Ranvier length as a potential regulator of myelinated axon conduction speed. *Elife,* 6.

ARROYO, E. J. & SCHERER, S. S. 2000. On the molecular architecture of myelinated fibers. *Histochem Cell Biol,* 113**,** 1-18.

BAI, Y., ZHANG, X., KATONA, I., SAPORTA, M. A., SHY, M. E., O'MALLEY, H. A., ISOM, L. L., SUTER, U. & LI, J. 2010. Conduction block in PMP22 deficiency. *J Neurosci,* 30**,** 600-8.

BAUMANN, N. & PHAM-DINH, D. 2001. Biology of oligodendrocyte and myelin in the mammalian central nervous system. *Physiol Rev,* 81**,** 871-927.

BENDER, L., LO, H. S., LEE, H., KOKOJAN, V., PETERSON, V. & BENDER, A. 1996. Associations among PH and SH3 domain-containing proteins and Rho-type GTPases in Yeast. *J Cell Biol,* 133**,** 879-94.

BENNETT, V. 2013. *Functional organization of vertebrate plasma membrane,* Current topics in membranes.

BERGHS, S., AGGUJARO, D., DIRKX, R., JR., MAKSIMOVA, E., STABACH, P., HERMEL, J. M., ZHANG, J. P., PHILBRICK, W., SLEPNEV, V., ORT, T. & SOLIMENA, M. 2000. betaIV spectrin, a new spectrin localized at axon initial segments and nodes of ranvier in the central and peripheral nervous system. *J Cell Biol,* 151**,** 985-1002.

BERTIN, A., MCMURRAY, M. A., THAI, L., GARCIA, G., 3RD, VOTIN, V., GROB, P., ALLYN, T., THORNER, J. & NOGALES, E. 2010. Phosphatidylinositol-4,5-bisphosphate promotes budding yeast septin filament assembly and organization. *J Mol Biol,* 404**,** 711-31.

BLACK, J. A. & WAXMAN, S. G. 1988. The perinodal astrocyte. *Glia,* 1**,** 169-83.

BOYLE, M. E., BERGLUND, E. O., MURAI, K. K., WEBER, L., PELES, E. & RANSCHT, B. 2001. Contactin orchestrates assembly of the septate-like junctions at the paranode in myelinated peripheral nerve. *Neuron,* 30**,** 385-97.

BRADY, S. T., WITT, A. S., KIRKPATRICK, L. L., DE WAEGH, S. M., READHEAD, C., TU, P. H. & LEE, V. M. 1999. Formation of compact myelin is required for maturation of the axonal cytoskeleton. *J Neurosci,* 19**,** 7278-88.

BRINKMANN, B. G., AGARWAL, A., SEREDA, M. W., GARRATT, A. N., MULLER, T., WENDE, H., STASSART, R. M., NAWAZ, S., HUMML, C., VELANAC, V., RADYUSHKIN, K., GOEBBELS, S., FISCHER, T. M., FRANKLIN, R. J., LAI, C., EHRENREICH, H., BIRCHMEIER, C., SCHWAB, M. H. & NAVE, K. A.

2008. Neuregulin-1/ErbB signaling serves distinct functions in myelination of the peripheral and central nervous system. *Neuron,* 59**,** 581-95.

CANTLEY, L. C. & NEEL, B. G. 1999. New insights into tumor suppression: PTEN suppresses tumor formation by restraining the phosphoinositide 3-kinase/AKT pathway. *Proc Natl Acad Sci U S A,* 96**,** 4240-5.

CAO, L., DING, X., YU, W., YANG, X., SHEN, S. & YU, L. 2007. Phylogenetic and evolutionary analysis of the septin protein family in metazoan. *FEBS Lett,* 581**,** 5526-32.

CARDONA, A., SAALFELD, S., SCHINDELIN, J., ARGANDA-CARRERAS, I., PREIBISCH, S., LONGAIR, M., TOMANCAK, P., HARTENSTEIN, V. & DOUGLAS, R. J. 2012. TrakEM2 software for neural circuit reconstruction. *PLoS One,* 7**,** e38011.

CHOMIAK, T. & HU, B. 2009. What is the optimal value of the g-ratio for myelinated fibers in the rat CNS? A theoretical approach. *PLoS One,* 4**,** e7754.

CHOU, C. C. & BUEHLER, M. J. 2012. Structure and mechanical properties of human trichocyte keratin intermediate filament protein. *Biomacromolecules,* 13**,** 3522-32.

COOPER, G. 2000. *Structure and Organization of Actin Filaments,* Sunderland (MA): Sinauer Associates.

DE WAEGH, S. M., LEE, V. M. & BRADY, S. T. 1992. Local modulation of neurofilament phosphorylation, axonal caliber, and slow axonal transport by myelinating Schwann cells. *Cell,* 68**,** 451-63.

DECHAT, T., ADAM, S. A., TAIMEN, P., SHIMI, T. & GOLDMAN, R. D. 2010. Nuclear lamins. *Cold Spring Harb Perspect Biol,* 2**,** a000547.

DEERINCK, T. J., BUSHONG, E. A., THOR, A. & ELLISMAN, M. H. 2010. NCMIR METHODS FOR 3D EM: A NEW PROTOCOL FOR PREPARATION OF BIOLOGICAL SPECIMENS FOR SERIAL BLOCKFACE SCANNING ELECTRON MICROSCOPY - SBEM Protocol v7_01_10'. NCMIR. Available at: https://www.ncmir.ucsd.edu/sbem-protocol.

DIBAJ, P., ZSCHUNTZSCH, J., STEFFENS, H., SCHEFFEL, J., GORICKE, B., WEISHAUPT, J. H., LE MEUR, K., KIRCHHOFF, F., HANISCH, U. K., SCHOMBURG, E. D. & NEUSCH, C. 2012. Influence of methylene blue on microglia-induced inflammation and motor neuron degeneration in the SOD1(G93A) model for ALS. *PLoS One,* 7**,** e43963.

EINHEBER, S., ZANAZZI, G., CHING, W., SCHERER, S., MILNER, T. A., PELES, E. & SALZER, J. L. 1997. The axonal membrane protein Caspr, a homologue of neurexin IV, is a component of the septate-like paranodal junctions that assemble during myelination. *J Cell Biol,* 139**,** 1495-506.

FIELD, C. M. & ALBERTS, B. M. 1995. Anillin, a contractile ring protein that cycles from the nucleus to the cell cortex. *J Cell Biol,* 131**,** 165-78.

FIELDS, R. D. & STEVENS-GRAHAM, B. 2002. New insights into neuron-glia communication. *Science,* 298**,** 556-62.

FORD, M. C., ALEXANDROVA, O., COSSELL, L., STANGE-MARTEN, A., SINCLAIR, J., KOPP-SCHEINPFLUG, C., PECKA, M., ATTWELL, D. & GROTHE, B. 2015. Tuning of Ranvier node and internode properties in myelinated axons to adjust action potential timing. *Nat Commun,* 6**,** 8073.

FUCHTBAUER, A., LASSEN, L. B., JENSEN, A. B., HOWARD, J., QUIROGA ADE, S., WARMING, S., SORENSEN, A. B., PEDERSEN, F. S. & FUCHTBAUER, E. M. 2011. Septin9 is involved in septin filament formation and cellular stability. *Biol Chem,* 392**,** 769-77.

FUNFSCHILLING, U., SUPPLIE, L. M., MAHAD, D., BORETIUS, S., SAAB, A. S., EDGAR, J., BRINKMANN, B. G., KASSMANN, C. M., TZVETANOVA, I. D., MOBIUS, W., DIAZ, F., MEIJER, D., SUTER, U., HAMPRECHT, B., SEREDA, M. W., MORAES, C. T., FRAHM, J., GOEBBELS, S. & NAVE, K. A. 2012. Glycolytic oligodendrocytes maintain myelin and long-term axonal integrity. *Nature,* 485**,** 517-21.

GALLYAS, F. 1979. Silver staining of myelin by means of physical development. *Neurol Res,* 1**,** 203-9.

GARCIA, M. L., LOBSIGER, C. S., SHAH, S. B., DEERINCK, T. J., CRUM, J., YOUNG, D., WARD, C. M., CRAWFORD, T. O., GOTOW, T., UCHIYAMA, Y., ELLISMAN, M. H., CALCUTT, N. A. & CLEVELAND, D. W. 2003. NF-M is an essential target for the myelin-directed "outside-in" signaling cascade that mediates radial axonal growth. *J Cell Biol,* 163**,** 1011-20.

GILDEN, J. & KRUMMEL, M. F. 2010. Control of cortical rigidity by the cytoskeleton: emerging roles for septins. *Cytoskeleton (Hoboken),* 67**,** 477-86.

GOEBBELS, S., OLTROGGE, J. H., KEMPER, R., HEILMANN, I., BORMUTH, I., WOLFER, S., WICHERT, S. P., MOBIUS, W., LIU, X., LAPPE-SIEFKE, C., ROSSNER, M. J., GROSZER, M., SUTER, U., FRAHM, J., BORETIUS, S. & NAVE, K. A. 2010. Elevated phosphatidylinositol 3,4,5-trisphosphate in glia triggers cell-autonomous membrane wrapping and myelination. *J Neurosci,* 30**,** 8953-64.

GOEBBELS, S., WIESER, G. L., PIEPER, A., SPITZER, S., WEEGE, B., YAN, K., EDGAR, J. M., YAGENSKY, O., WICHERT, S. P., AGARWAL, A., KARRAM, K., RENIER, N., TESSIER-LAVIGNE, M., ROSSNER, M. J., KARADOTTIR, R. T. & NAVE, K. A. 2017. A neuronal PI(3,4,5)P3-dependent program of oligodendrocyte precursor recruitment and myelination. *Nat Neurosci,* 20**,** 10-15.

GOLLAN, L., SABANAY, H., POLIAK, S., BERGLUND, E. O., RANSCHT, B. & PELES, E. 2002. Retention of a cell adhesion complex at the paranodal junction requires the cytoplasmic region of Caspr. *J Cell Biol,* 157**,** 1247-56.

GRIFFITHS, I., KLUGMANN, M., ANDERSON, T., YOOL, D., THOMSON, C., SCHWAB, M. H., SCHNEIDER, A., ZIMMERMANN, F., MCCULLOCH, M.,

NADON, N. & NAVE, K. A. 1998. Axonal swellings and degeneration in mice lacking the major proteolipid of myelin. *Science,* 280**,** 1610-3.

GUTIERREZ, R., BOISON, D., HEINEMANN, U. & STOFFEL, W. 1995. Decompaction of Cns Myelin Leads to a Reduction of the Conduction-Velocity of Action-Potentials in Optic-Nerve. *Neuroscience Letters,* 195**,** 93-96.

HALL, P. A. & RUSSELL, S. E. 2004. The pathobiology of the septin gene family. *J Pathol,* 204**,** 489-505.

HALL, P. A. & RUSSELL, S. E. 2012. Mammalian septins: dynamic heteromers with roles in cellular morphogenesis and compartmentalization. *J Pathol,* 226**,** 287-99.

HANISCH, U. K. 2002. Microglia as a source and target of cytokines. *Glia,* 40**,** 140-55.

HANISCH, U. K. & KETTENMANN, H. 2007. Microglia: active sensor and versatile effector cells in the normal and pathologic brain. *Nat Neurosci,* 10**,** 1387-94.

HARTLINE, D. K. & COLMAN, D. R. 2007. Rapid conduction and the evolution of giant axons and myelinated fibers. *Curr Biol,* 17**,** R29-35.

HERRMANN, H., BAR, H., KREPLAK, L., STRELKOV, S. V. & AEBI, U. 2007. Intermediate filaments: from cell architecture to nanomechanics. *Nat Rev Mol Cell Biol,* 8**,** 562-73.

HILDEBRAND, C. & HAHN, R. 1978. Relation between myelin sheath thickness and axon size in spinal cord white matter of some vertebrate species. *J Neurol Sci,* 38**,** 421-34.

HIROKAWA, N. & TAKEMURA, R. 2005. Molecular motors and mechanisms of directional transport in neurons. *Nat Rev Neurosci,* 6**,** 201-14.

HSIEH, S. T., KIDD, G. J., CRAWFORD, T. O., XU, Z., LIN, W. M., TRAPP, B. D., CLEVELAND, D. W. & GRIFFIN, J. W. 1994. Regional modulation of neurofilament organization by myelination in normal axons. *J Neurosci,* 14**,** 6392-401.

JAEGLE, M., GHAZVINI, M., MANDEMAKERS, W., PIIRSOO, M., DRIEGEN, S., LEVAVASSEUR, F., RAGHOENATH, S., GROSVELD, F. & MEIJER, D. 2003. The POU proteins Brn-2 and Oct-6 share important functions in Schwann cell development. *Genes Dev,* 17**,** 1380-91.

JOBERTY, G., PERLUNGHER, R. R., SHEFFIELD, P. J., KINOSHITA, M., NODA, M., HAYSTEAD, T. & MACARA, I. G. 2001. Borg proteins control septin organization and are negatively regulated by Cdc42. *Nat Cell Biol,* 3**,** 861-6.

JUNG, M., SOMMER, I., SCHACHNER, M. & NAVE, K. A. 1996. Monoclonal antibody O10 defines a conformationally sensitive cell-surface epitope of proteolipid protein (PLP): evidence that PLP misfolding underlies dysmyelination in mutant mice. *J Neurosci,* 16**,** 7920-9.

KETTENMANN, H., HANISCH, U. K., NODA, M. & VERKHRATSKY, A. 2011. Physiology of microglia. *Physiol Rev,* 91**,** 461-553.

KETTENMANN, H. & RANSOM, B. R. 2005. *Neuroglia*, Oxford University Press.

KIM, S. K., KIM, H., YANG, Y. R., SUH, P. G. & CHANG, J. S. 2011. Phosphatidylinositol phosphates directly bind to neurofilament light chain (NF-L) for the regulation of NF-L self assembly. *Exp Mol Med,* 43**,** 153-60.

KING, R. 2013. Microscopic anatomy: normal structure. *Handb Clin Neurol,* 115**,** 7-27.

KINOSHITA, M. 2003. Assembly of Mammalian Septins. *Journal of Biochemistry,* 134**,** 491-496.

KINOSHITA, M., FIELD, C. M., COUGHLIN, M. L., STRAIGHT, A. F. & MITCHISON, T. J. 2002. Self- and actin-templated assembly of Mammalian septins. *Dev Cell,* 3**,** 791-802.

KIRCHHOFF, F., DRINGEN, R. & GIAUME, C. 2001. Pathways of neuron-astrocyte interactions and their possible role in neuroprotection. *Eur Arch Psychiatry Clin Neurosci,* 251**,** 159-69.

KIRKPATRICK, L. L., WITT, A. S., PAYNE, H. R., SHINE, H. D. & BRADY, S. T. 2001. Changes in microtubule stability and density in myelin-deficient shiverer mouse CNS axons. *J Neurosci,* 21**,** 2288-97.

KISSEL, H., GEORGESCU, M. M., LARISCH, S., MANOVA, K., HUNNICUTT, G. R. & STELLER, H. 2005. The Sept4 septin locus is required for sperm terminal differentiation in mice. *Dev Cell,* 8**,** 353-64.

KLUGMANN, M., SCHWAB, M. H., PUHLHOFER, A., SCHNEIDER, A., ZIMMERMANN, F., GRIFFITHS, I. R. & NAVE, K. A. 1997. Assembly of CNS myelin in the absence of proteolipid protein. *Neuron,* 18**,** 59-70.

KONIG, S., HOFFMANN, M., MOSBLECH, A. & HEILMANN, I. 2008. Determination of content and fatty acid composition of unlabeled phosphoinositide species by thin-layer chromatography and gas chromatography. *Anal Biochem,* 378**,** 197-201.

KREMER, J. R., MASTRONARDE, D. N. & MCINTOSH, J. R. 1996. Computer visualization of three-dimensional image data using IMOD. *J Struct Biol,* 116**,** 71-6.

KUHLENBAUMER, G., HANNIBAL, M. C., NELIS, E., SCHIRMACHER, A., VERPOORTEN, N., MEULEMAN, J., WATTS, G. D., DE VRIENDT, E., YOUNG, P., STOGBAUER, F., HALFTER, H., IROBI, J., GOOSSENS, D., DEL-FAVERO, J., BETZ, B. G., HOR, H., KURLEMANN, G., BIRD, T. D., AIRAKSINEN, E., MONONEN, T., SERRADELL, A. P., PRATS, J. M., VAN BROECKHOVEN, C., DE JONGHE, P., TIMMERMAN, V., RINGELSTEIN, E. B. & CHANCE, P. F. 2005. Mutations in SEPT9 cause hereditary neuralgic amyotrophy. *Nat Genet,* 37**,** 1044-6.

KWITNY, S., KLAUS, A. V. & HUNNICUTT, G. R. 2010. The annulus of the mouse sperm tail is required to establish a membrane diffusion barrier that is engaged during the late steps of spermiogenesis. *Biol Reprod,* 82**,** 669-78.

LAPPE-SIEFKE, C., GOEBBELS, S., GRAVEL, M., NICKSCH, E., LEE, J., BRAUN, P. E., GRIFFITHS, I. R. & NAVE, K. A. 2003. Disruption of Cnp1 uncouples oligodendroglial functions in axonal support and myelination. *Nat Genet,* 33**,** 366-74.

LAROCCA, J. N. & NORTON, W. T. 2007. Isolation of myelin. *Curr Protoc Cell Biol,* Chapter 3**,** Unit3 25.

LEE, J. C., SHIN, J. H., PARK, B. W., KIM, G. S., KIM, J. C., KANG, K. S. & CHA, C. I. 2012. Region-specific changes in the immunoreactivity of SIRT1 expression in the central nervous system of SOD1(G93A) transgenic mice as an in vivo model of amyotrophic lateral sclerosis. *Brain Res,* 1433**,** 20-8.

LEE, J. Y., KIM, M. J., LI, L., VELUMIAN, A. A., AUI, P. M., FEHLINGS, M. G. & PETRATOS, S. 2017. Nogo receptor 1 regulates Caspr distribution at axo-glial units in the central nervous system. *Sci Rep,* 7**,** 8958.

LEITE, S. C., SAMPAIO, P., SOUSA, V. F., NOGUEIRA-RODRIGUES, J., PINTO-COSTA, R., PETERS, L. L., BRITES, P. & SOUSA, M. M. 2016. The Actin-Binding Protein alpha-Adducin Is Required for Maintaining Axon Diameter. *Cell Rep,* 15**,** 490-498.

LINNINGTON, C., WEBB, M. & WOODHAMS, P. L. 1984. A novel myelin-associated glycoprotein defined by a mouse monoclonal antibody. *J Neuroimmunol,* 6**,** 387-96.

LIU, J., FAIRN, G. D., CECCARELLI, D. F., SICHERI, F. & WILDE, A. 2012. Cleavage Furrow Organization Requires PIP(2)-Mediated Recruitment of Anillin. *Curr Biol,* 22**,** 64-9.

LOW, C. & MACARA, I. G. 2006. Structural analysis of septin 2, 6, and 7 complexes. *J Biol Chem,* 281**,** 30697-706.

MACARA, I. G., BALDARELLI, R., FIELD, C. M., GLOTZER, M., HAYASHI, Y., HSU, S. C., KENNEDY, M. B., KINOSHITA, M., LONGTINE, M., LOW, C., MALTAIS, L. J., MCKENZIE, L., MITCHISON, T. J., NISHIKAWA, T., NODA, M., PETTY, E. M., PEIFER, M., PRINGLE, J. R., ROBINSON, P. J., ROTH, D., RUSSELL, S. E., STUHLMANN, H., TANAKA, M., TANAKA, T., TRIMBLE, W. S., WARE, J., ZELEZNIK-LE, N. J. & ZIEGER, B. 2002. Mammalian septins nomenclature. *Mol Biol Cell,* 13**,** 4111-3.

MADDOX, A. S., LEWELLYN, L., DESAI, A. & OEGEMA, K. 2007. Anillin and the septins promote asymmetric ingression of the cytokinetic furrow. *Dev Cell,* 12**,** 827-35.

MENDOZA, M., HYMAN, A. A. & GLOTZER, M. 2002. GTP binding induces filament assembly of a recombinant septin. *Curr Biol,* 12**,** 1858-63.

MICHAILOV, G. V., SEREDA, M. W., BRINKMANN, B. G., FISCHER, T. M., HAUG, B., BIRCHMEIER, C., ROLE, L., LAI, C., SCHWAB, M. H. & NAVE, K. A. 2004. Axonal neuregulin-1 regulates myelin sheath thickness. *Science,* 304**,** 700-3.

MIESCHER, G. C., LUTZELSCHWAB, R., ERNE, B., FERRACIN, F., HUBER, S. & STECK, A. J. 1997. Reciprocal expression of myelin-associated glycoprotein splice variants in the adult human peripheral and central nervous systems. *Brain Res Mol Brain Res,* 52**,** 299-306.

MILLER, K. G., FIELD, C. M. & ALBERTS, B. M. 1989. Actin-binding proteins from Drosophila embryos: a complex network of interacting proteins detected by F-actin affinity chromatography. *J Cell Biol,* 109**,** 2963-75.

MOSTOWY, S. & COSSART, P. 2012. Septins: the fourth component of the cytoskeleton. *Nat Rev Mol Cell Biol*.

NAVE, K. A. 2010. Myelination and support of axonal integrity by glia. *Nature,* 468**,** 244-52.

NAVE, K. A. & WERNER, H. B. 2014. Myelination of the nervous system: mechanisms and functions. *Annu Rev Cell Dev Biol,* 30**,** 503-33.

NIMMERJAHN, A., KIRCHHOFF, F. & HELMCHEN, F. 2005. Resting microglial cells are highly dynamic surveillants of brain parenchyma in vivo. *Science,* 308**,** 1314-8.

NORTON, W. T. & PODUSLO, S. E. 1973. Myelination in rat brain: method of myelin isolation. *J Neurochem,* 21**,** 749-57.

ODA, T., IWASA, M., AIHARA, T., MAEDA, Y. & NARITA, A. 2009. The nature of the globular- to fibrous-actin transition. *Nature,* 457**,** 441-5.

OEGEMA, K., SAVOIAN, M. S., MITCHISON, T. J. & FIELD, C. M. 2000. Functional analysis of a human homologue of the Drosophila actin binding protein anillin suggests a role in cytokinesis. *J Cell Biol,* 150**,** 539-52.

OGAWA, Y., OSES-PRIETO, J., KIM, M. Y., HORRESH, I., PELES, E., BURLINGAME, A. L., TRIMMER, J. S., MEIJER, D. & RASBAND, M. N. 2010. ADAM22, a Kv1 channel-interacting protein, recruits membrane-associated guanylate kinases to juxtaparanodes of myelinated axons. *J Neurosci,* 30**,** 1038-48.

OH, Y. & BI, E. 2011. Septin structure and function in yeast and beyond. *Trends Cell Biol,* 21**,** 141-8.

ORELLANA-MUNOZ, S., DUENAS-SANTERO, E., ARNAIZ-PITA, Y., DEL REY, F., CORREA-BORDES, J. & VAZQUEZ DE ALDANA, C. R. 2018. The anillin-related Int1 protein and the Sep7 septin collaborate to maintain cellular ploidy in Candida albicans. *Sci Rep,* 8**,** 2257.

PALANDRI, A., SALVADOR, V. R., WOJNACKI, J., VIVINETTO, A. L., SCHNAAR, R. L. & LOPEZ, P. H. 2015. Myelin-associated glycoprotein modulates

apoptosis of motoneurons during early postnatal development via NgR/p75(NTR) receptor-mediated activation of RhoA signaling pathways. *Cell Death Dis,* 6**,** e1876.

PATZIG, J., ERWIG, M. S., TENZER, S., KUSCH, K., DIBAJ, P., MOBIUS, W., GOEBBELS, S., SCHAEREN-WIEMERS, N., NAVE, K. A. & WERNER, H. B. 2016. Septin/anillin filaments scaffold central nervous system myelin to accelerate nerve conduction. *Elife,* 5.

PIEKNY, A. J. & GLOTZER, M. 2008. Anillin is a scaffold protein that links RhoA, actin, and myosin during cytokinesis. *Curr Biol,* 18**,** 30-6.

PIEKNY, A. J. & MADDOX, A. S. 2010. The myriad roles of Anillin during cytokinesis. *Semin Cell Dev Biol,* 21**,** 881-91.

POLIAK, S. & PELES, E. 2003. The local differentiation of myelinated axons at nodes of Ranvier. *Nat Rev Neurosci,* 4**,** 968-80.

POLLARD, T. D. 2017. Tribute to Fumio Oosawa the pioneer in actin biophysics. *Cytoskeleton (Hoboken),* 74**,** 446-449.

RASBAND, M. N. 2011. Composition, assembly, and maintenance of excitable membrane domains in myelinated axons. *Semin Cell Dev Biol,* 22**,** 178-84.

READHEAD, C., POPKO, B., TAKAHASHI, N., SHINE, H. D., SAAVEDRA, R. A., SIDMAN, R. L. & HOOD, L. 1987. Expression of a myelin basic protein gene in transgenic shiverer mice: correction of the dysmyelinating phenotype. *Cell,* 48**,** 703-12.

RENSHAW, M. J., LIU, J., LAVOIE, B. D. & WILDE, A. 2014. Anillin-dependent organization of septin filaments promotes intercellular bridge elongation and Chmp4B targeting to the abscission site. *Open Biol,* 4**,** 130190.

RICHARDSON, K. C., JARETT, L. & FINKE, E. H. 1960. Embedding in epoxy resins for ultrathin sectioning in electron microscopy. *Stain Technol,* 35**,** 313-23.

RIVEST, S. 2009. Regulation of innate immune responses in the brain. *Nat Rev Immunol,* 9**,** 429-39.

RUSHTON, W. A. 1951. A theory of the effects of fibre size in medullated nerve. *J Physiol,* 115**,** 101-22.

SALZER, J. L. 2003. Polarized domains of myelinated axons. *Neuron,* 40**,** 297-318.

SALZER, J. L., BROPHY, P. J. & PELES, E. 2008. Molecular domains of myelinated axons in the peripheral nervous system. *Glia,* 56**,** 1532-40.

SCHINDELIN, J., ARGANDA-CARRERAS, I., FRISE, E., KAYNIG, V., LONGAIR, M., PIETZSCH, T., PREIBISCH, S., RUEDEN, C., SAALFELD, S., SCHMID, B., TINEVEZ, J. Y., WHITE, D. J., HARTENSTEIN, V., ELICEIRI, K., TOMANCAK, P. & CARDONA, A. 2012. Fiji: an open-source platform for biological-image analysis. *Nat Methods,* 9**,** 676-82.

SEIDL, A. H. 2014. Regulation of conduction time along axons. *Neuroscience,* 276**,** 126-34.

SHARMA, K. Z., GUIXIN; LI, SHUXIN 2015. *Astrogliosis and Axonal Regeneration,* Academic Press.

SHERMAN, D. L., TAIT, S., MELROSE, S., JOHNSON, R., ZONTA, B., COURT, F. A., MACKLIN, W. B., MEEK, S., SMITH, A. J., COTTRELL, D. F. & BROPHY, P. J. 2005. Neurofascins are required to establish axonal domains for saltatory conduction. *Neuron,* 48**,** 737-42.

SIRAJUDDIN, M., FARKASOVSKY, M., HAUER, F., KUHLMANN, D., MACARA, I. G., WEYAND, M., STARK, H. & WITTINGHOFER, A. 2007. Structural insight into filament formation by mammalian septins. *Nature,* 449**,** 311-5.

SNAIDERO, N., MOBIUS, W., CZOPKA, T., HEKKING, L. H., MATHISEN, C., VERKLEIJ, D., GOEBBELS, S., EDGAR, J., MERKLER, D., LYONS, D. A., NAVE, K. A. & SIMONS, M. 2014. Myelin Membrane Wrapping of CNS Axons by PI(3,4,5)P3-Dependent Polarized Growth at the Inner Tongue. *Cell,* 156**,** 277-90.

STILES, B., GROSZER, M., WANG, S., JIAO, J. & WU, H. 2004. PTENless means more. *Dev Biol,* 273**,** 175-84.

STRAIGHT, A. F., FIELD, C. M. & MITCHISON, T. J. 2005. Anillin binds nonmuscle myosin II and regulates the contractile ring. *Mol Biol Cell,* 16**,** 193-201.

STREIT, W. J., CONDE, J. R., FENDRICK, S. E., FLANARY, B. E. & MARIANI, C. L. 2005. Role of microglia in the central nervous system's immune response. *Neurol Res,* 27**,** 685-91.

SUZUKI, A., NAKANO, T., MAK, T. W. & SASAKI, T. 2008. Portrait of PTEN: messages from mutant mice. *Cancer Sci,* 99**,** 209-13.

TADA, T., SIMONETTA, A., BATTERTON, M., KINOSHITA, M., EDBAUER, D. & SHENG, M. 2007. Role of Septin cytoskeleton in spine morphogenesis and dendrite development in neurons. *Curr Biol,* 17**,** 1752-8.

TANAKA-TAKIGUCHI, Y., KINOSHITA, M. & TAKIGUCHI, K. 2009. Septin-mediated uniform bracing of phospholipid membranes. *Curr Biol,* 19**,** 140-5.

THURNHERR, T., BENNINGER, Y., WU, X., CHROSTEK, A., KRAUSE, S. M., NAVE, K. A., FRANKLIN, R. J., BRAKEBUSCH, C., SUTER, U. & RELVAS, J. B. 2006. Cdc42 and Rac1 signaling are both required for and act synergistically in the correct formation of myelin sheaths in the CNS. *J Neurosci,* 26**,** 10110-9.

TOOLEY, A. J., GILDEN, J., JACOBELLI, J., BEEMILLER, P., TRIMBLE, W. S., KINOSHITA, M. & KRUMMEL, M. F. 2009. Amoeboid T lymphocytes require the septin cytoskeleton for cortical integrity and persistent motility. *Nat Cell Biol,* 11**,** 17-26.

TOWBIN, H., STAEHELIN, T. & GORDON, J. 1979. Electrophoretic transfer of proteins from polyacrylamide gels to nitrocellulose sheets: procedure and some applications. *Proc Natl Acad Sci U S A,* 76**,** 4350-4.

TOYA, M., IINO, Y. & YAMAMOTO, M. 1999. Fission yeast Pob1p, which is homologous to budding yeast Boi proteins and exhibits subcellular localization close to actin patches, is essential for cell elongation and separation. *Mol Biol Cell,* 10**,** 2745-57.

TRAPP, B. D., ANDREWS, S. B., COOTAUCO, C. & QUARLES, R. 1989. The myelin-associated glycoprotein is enriched in multivesicular bodies and periaxonal membranes of actively myelinating oligodendrocytes. *J Cell Biol,* 109**,** 2417-26.

TRAPP, B. D. & QUARLES, R. H. 1982. Presence of the myelin-associated glycoprotein correlates with alterations in the periodicity of peripheral myelin. *J Cell Biol,* 92**,** 877-82.

TSANG, C. W., ESTEY, M. P., DICICCIO, J. E., XIE, H., PATTERSON, D. & TRIMBLE, W. S. 2011. Characterization of presynaptic septin complexes in mammalian hippocampal neurons. *Biol Chem,* 392**,** 739-49.

VALE, R. D. 2003. The molecular motor toolbox for intracellular transport. *Cell,* 112**,** 467-80.

VAQUIE, A., SAUVAIN, A. & JACOB, C. 2018. Modeling PNS and CNS Myelination Using Microfluidic Chambers. *Methods Mol Biol,* 1791**,** 157-168.

VERSELE, M. & THORNER, J. 2005. Some assembly required: yeast septins provide the instruction manual. *Trends Cell Biol,* 15**,** 414-24.

WALKER, R. A., O'BRIEN, E. T., PRYER, N. K., SOBOEIRO, M. F., VOTER, W. A., ERICKSON, H. P. & SALMON, E. D. 1988. Dynamic instability of individual microtubules analyzed by video light microscopy: rate constants and transition frequencies. *J Cell Biol,* 107**,** 1437-48.

WANG IP, C., KRONER, A., FISCHER, S., BERGHOFF, M., KOBSAR, I., MAURER, M. & MARTINI, R. 2006. Role of immune cells in animal models for inherited peripheral neuropathies. *Neuromolecular Med,* 8**,** 175-90.

WANG, K. C., KIM, J. A., SIVASANKARAN, R., SEGAL, R. & HE, Z. 2002. P75 interacts with the Nogo receptor as a co-receptor for Nogo, MAG and OMgp. *Nature,* 420**,** 74-8.

WU, L. M., WILLIAMS, A., DELANEY, A., SHERMAN, D. L. & BROPHY, P. J. 2012. Increasing internodal distance in myelinated nerves accelerates nerve conduction to a flat maximum. *Curr Biol,* 22**,** 1957-61.

XIE, Y., VESSEY, J. P., KONECNA, A., DAHM, R., MACCHI, P. & KIEBLER, M. A. 2007. The GTP-binding protein Septin 7 is critical for dendrite branching and dendritic-spine morphology. *Curr Biol,* 17**,** 1746-51.

YIN, X., CRAWFORD, T. O., GRIFFIN, J. W., TU, P., LEE, V. M., LI, C., RODER, J. & TRAPP, B. D. 1998. Myelin-associated glycoprotein is a myelin signal that modulates the caliber of myelinated axons. *J Neurosci,* 18**,** 1953-62.

YUAN, A., SASAKI, T., KUMAR, A., PETERHOFF, C. M., RAO, M. V., LIEM, R. K., JULIEN, J. P. & NIXON, R. A. 2012. Peripherin is a subunit of peripheral nerve neurofilaments: implications for differential vulnerability of CNS and peripheral nervous system axons. *J Neurosci,* 32**,** 8501-8.

ZHANG, J., KONG, C., XIE, H., MCPHERSON, P. S., GRINSTEIN, S. & TRIMBLE, W. S. 1999. Phosphatidylinositol polyphosphate binding to the mammalian septin H5 is modulated by GTP. *Curr Biol,* 9**,** 1458-67.

ZHANG, Y., CHEN, K., SLOAN, S. A., BENNETT, M. L., SCHOLZE, A. R., O'KEEFFE, S., PHATNANI, H. P., GUARNIERI, P., CANEDA, C., RUDERISCH, N., DENG, S., LIDDELOW, S. A., ZHANG, C., DANEMAN, R., MANIATIS, T., BARRES, B. A. & WU, J. Q. 2014. An RNA-sequencing transcriptome and splicing database of glia, neurons, and vascular cells of the cerebral cortex. *J Neurosci,* 34**,** 11929-47.

ZHOU, D., LAMBERT, S., MALEN, P. L., CARPENTER, S., BOLAND, L. M. & BENNETT, V. 1998. AnkyrinG is required for clustering of voltage-gated Na channels at axon initial segments and for normal action potential firing. *J Cell Biol,* 143**,** 1295-304.

7 Addendum

7.1 Abstract

Septins are a family of highly conserved filament-forming GTP-binding proteins. Some members of this protein family were identified to be abundant in myelin (e.g. SEPT2, SEPT7, SEPT8, SEPT9), in which they support long-term stability, at least in the CNS. In humans, mutations of the *SEPT9* gene cause hereditary neuralgic amyotrophy (HNA), an autosomal dominant disorder, which predominantly affects the peripheral brachial plexus. Mice carrying a point mutation in the *Sept9* gene, which is often seen in human HNA, and mice conditionally lacking SEPT9 or SEPT2 in Schwann cells were analyzed to possibly generate the first mouse model of HNA and to further investigate the biology of septins *in vivo*. Sequencing of the mutated gene region confirmed the point mutation in experimental animals. Immunoblots, and immunohistochemical labeling of teased fibers were used to analyze possible alterations in SEPT9 abundance and localization. By immunohistochemical labeling, septins were found to localize to paranodal segments adjacent to the nodes of Ranvier, the outer rim of Schmidt-Lanterman incisures, and the bands of Cajal. In all analyzed regions, no alterations of septin localization or abundance were detectable. Furthermore, $Sept9^{R88W/Wt}$ mice showed unaltered numbers of myelinated axons, as well as unaltered myelin ultrastructure in sciatic nerves at P75. Mice lacking SEPT2 or SEPT9 from Schwann cells were analyzed on electron microscopic level at P4, P14, and 6 mo of age. No signs of impaired developmental myelination or pathology were identifiable. According to the analyses, *Sept9* or *Sept2* mutant mice, as well as mice carrying the point mutation showed no HNA-related abnormalities. This may reflect that a second impact, such as nerve constriction or inflammation might be necessary to trigger the onset of pathology. Taken together, the investigation of mice lacking SEPT2 or SEPT9 from Schwann cells or carrying a point mutation provide a valuable basis for further analysis aiming to understand the pathology of HNA.

7.2 Introduction

7.2.1 Septins in the peripheral nervous system

Mass spectrometry of purified myelin of sciatic nerves showed that in the peripheral nervous system (PNS), SEPT2, SEPT7, and SEPT11 are the most abundant septins. SEPT9 was found in a comparatively low abundance (Patzig *et al.*, 2011). With immunohistochemical analysis of sciatic nerve teased fibers, SEPT2, SEPT7, SEPT8, SEPT9, and SEPT11 were detected. All of them localized to the paranodal myelin compartment (flanking the nodes of Ranvier) and also abaxonally in the outermost rim of Schmidt-Lanterman incisures and the bands of Cajal (Buser *et al.*, 2009; Ogawa and Rasband, 2009; Patzig *et al.*, 2011). Previous experiments showed that in PNS myelin SEPT2 is essential for the presence of other PNS

myelin septins, as mice lacking SEPT2 from Schwann cells have strongly reduced protein abundances of all other PNS myelin septins (unpublished data).

7.2.2 Hereditary neuralgic amyotrophy

Hereditary neuralgic amyotrophy (HNA) is an autosomal dominant disorder characterized by recurrent episodes of focal neuropathy of the brachial plexus (Meuleman *et al.*, 2001). The majority of HNA cases are caused by mutations affecting the *SEPT9* gene on chromosome 17q25, thereby a point mutation of Arginine 88 to Tryptophan (R88W) is often seen (Kuhlenbäumer, *et al*., 2005; PMID 16186812; Meulemann *et al.*, 2001; PMID 10602368). Owing to the lack of biopsy material and a rodent model, the pathobiology of HNA caused by SEPT9 mutations, has remained largely unknown at the molecular, cellular, and histological level.

The onset of the disease occurs usually in the 2nd to 3rd decade, whereby a single episode typically starts with pain in the affected arm. Weakness and sensory disturbances, which develop within days after onset of the pain, are also characteristic for this phenotype. Often, early in an episode, prominent atrophy of the affected muscles develops. The recover begins weeks to month after onset and can take months to years. There are different degrees of recovery, which vary from moderate to excellent. The next episode then can affect the same limb as well as the opposite one. Recurrent episodes in the same limb can lead to incomplete recovery. In HNA, any part of the brachial plexus can be affected, with a predilection for the upper trunk which enervates the proximal upper limb muscle. All in all, the classical course of the disease can be described as relapsing-remitting (Chance, 2006; van Alfen, 2011).

7.3 Results

7.3.1 Analysis of *Sept9$^{R88W/Wt}$* mice

7.3.1.1 Point mutation has no effect on septin protein abundances

As SEPT9 mutations are often seen in HNA patients, especially the R88W point mutation, *Sept9$^{R88W/Wt}$* mice were analyzed at P75. When breeding heterozygous with heterozygous mice, it was noticed that no homozygous mice were born (Addendum Figure 1A) indicating that carrying the point mutation on both *Sept9* alleles is embryonic lethal. Consequently, only *Sept9$^{R88W/Wt}$* mice could have been analyzed. In a next step, the abundance of SEPT9 in sciatic nerve lysates at P75 was analyzed on immunoblot level. In Addendum Figure 1B it is displayed, that the point mutation has no effect on the abundance of SEPT9. In the PNS the essential septin to form a filament is SEPT2. Accordingly, the abundance of SEPT2 was analyzed and revealed no difference between controls (*Sept9$^{Wt/Wt}$*) and *Sept9$^{R88W/Wt}$* mice.

Taken together, the results suggest that the point mutation does not interfere with the presence of septins in PNS myelin.

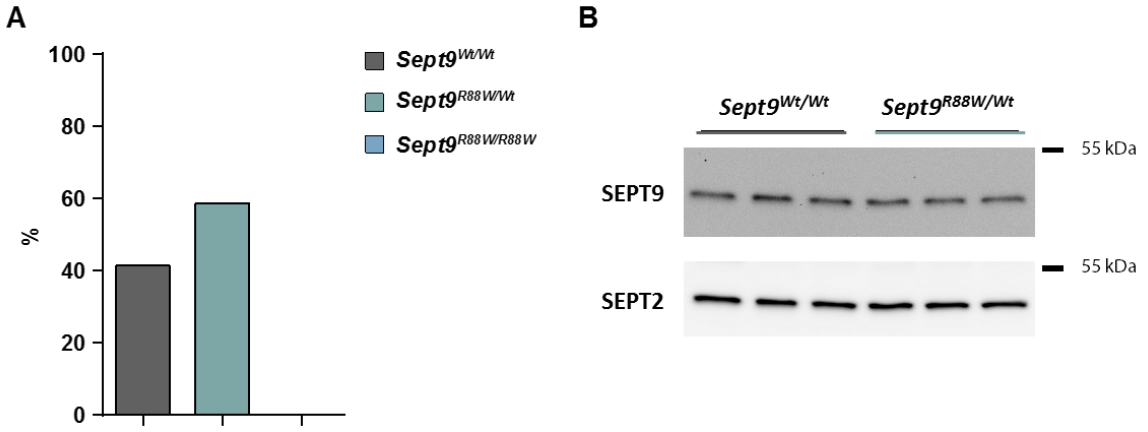

Addendum Figure 1: Offspring analysis and abundance of SEPT9 and SEPT2 in *Sept9*$^{R88W/Wt}$ mice. (**A**) Offspring analysis of breedings with *Sept9*$^{R88W/Wt}$ males and *Sept9*$^{R88W/Wt}$ females, depicts that no homozygous animals were born (Statistical expectation: 25% WT; 50% heterozygous; 25% homozygous). In total, 121 pups were analyzed. (**B**) Immunoblot analysis of sciatic nerve lysates at P75 from control (*Sept9*$^{Wt/Wt}$) and *Sept9*$^{R88W/Wt}$ mice. SEPT9 and SEPT2 are not altered in *Sept9*$^{R88W/Wt}$ mice.

7.3.1.2 No changes in localization of SEPT9

To assess whether the R88W point mutation has an effect on the localization of SEPT9, immunohistochemical stainings were performed on teased fibers of sciatic nerves at P75. There was no difference in SEPT9 localization detectable between *Sept9*$^{Wt/Wt}$ and *Sept9*$^{R88W/Wt}$ mice (Addendum Figure 2). In both genotypes, SEPT9 is located at nodes of Ranvier, bands of Cajal, and Schmidt-Lanterman incisures (SLI).

The results suggest that the point mutation has no effect on the localization of SEPT9 in sciatic nerves.

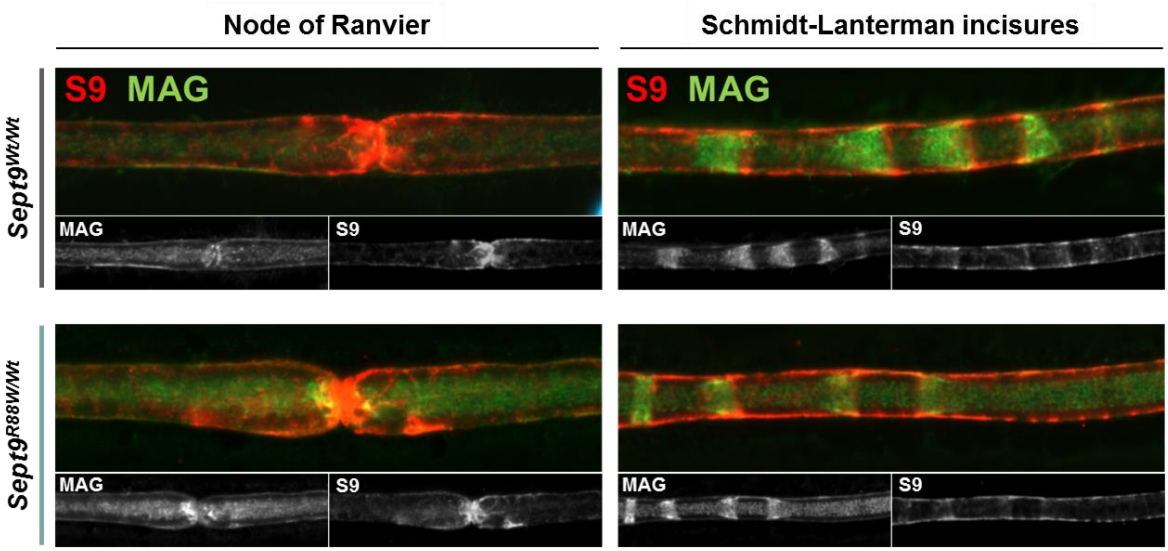

Addendum Figure 2: Localization of SEPT9 in sciatic nerves. Immunolabeling validates normal distribution and localization of SEPT9 (red) in teased fibers of sciatic nerves at P75. MAG (green) is stained as control, labeling the abaxonal and adaxonal myelin and SLIs. Labeling of SEPT9 reveals localization to nodes of

Ranvier, abaxonal myelin, bands of Cajal, and SLIs. Images are representative of three independent experiments.

7.3.1.3 Unaltered nerve structure

To analyze the effect of the point mutation on the PNS, sciatic nerves were analyzed on semi-thin sections. Images were taken with a 100x oil objective of the Zeiss Axio Imager Z1 and stitched using the ZEN 2011 software (Addendum Figure 3A). Reconstruction reveals normal sciatic nerve structure at P75. Squares highlight respective regions within the sciatic nerves and indicate normal myelination. To further analyze whether the point mutation has an impact on myelination, myelinated axons were quantified and normalized to the nerve area (Addendum Figure 3B). The evaluation reveals normal numbers of myelinated axons within sciatic nerves of *Sept9*$^{R88W/Wt}$ mice compared to controls at P75.

The results indicate that the point mutation has no impact on the ability of Schwann cells to myelinate axons and therefore is also not altering the overall nerve structure.

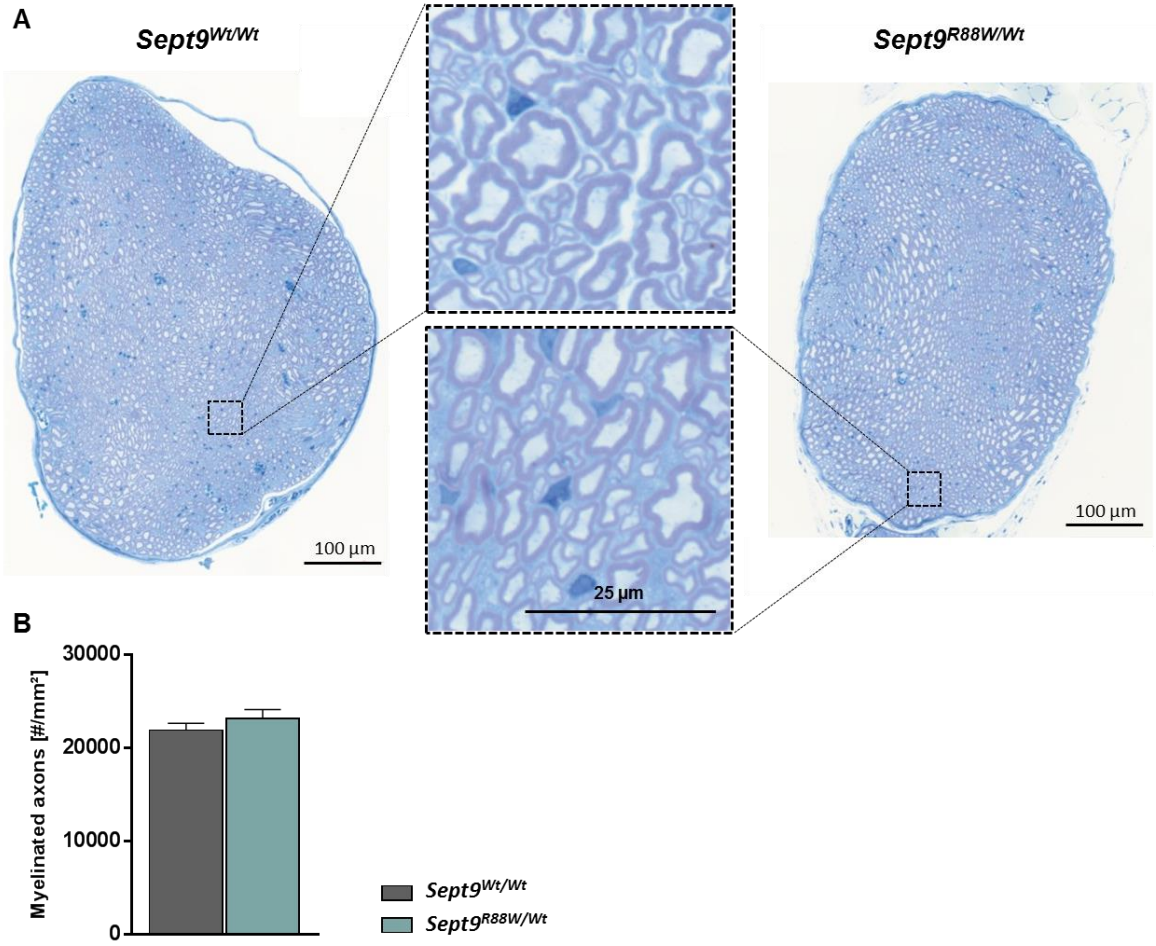

Addendum Figure 3: Nerve structure and myelinated axons. (**A**) Light microscopic images of *Sept9*$^{Wt/Wt}$ and *Sept9*$^{R88W/Wt}$ sciatic nerves at P75. Squares highlight respective region. Images depict no sign of structural alterations in *Sept9*$^{R88W/Wt}$ mice. Images are representative for n=4 animals per genotype. (**B**) Quantitative evaluation of all myelinated axons of light microscopic images of sciatic nerves at P75. Quantification reveals normal numbers of myelinated axons normalized to nerve area in *Sept9*$^{R88W/Wt}$ mice compared to controls. Mean +/ SEM. n=4 animals per genotype; not significant according to two-tailed unpaired t-test (p= 0.3311).

7.3.1.4 Normal myelin ultrastructure

Sciatic nerves were also analyzed on electron microscopic level, to identify possible effects of the R88W point mutation on myelin ultrastructure or Remak bundle appearance. Electron micrographs (Addendum Figure 4) reveal normal myelinated axons and no alterations in myelin ultrastructure at P75 in *Sept9*$^{R88W/Wt}$ sciatic nerves. Additionally, the axons show no signs of pathology. Moreover, the images illustrate a normal size of Remak bundles. Within the Remak bundles, no alterations in axon numbers and axon size were found.

To sum these findings up, *Sept9*$^{R88W/Wt}$ mice are able to form myelin in a normal state as control animals. There were no obvious ultrastructural changes detectable in Schwann cells of mice carrying the point mutation. Neither in myelinating Schwann cells, nor in Remak bundles.

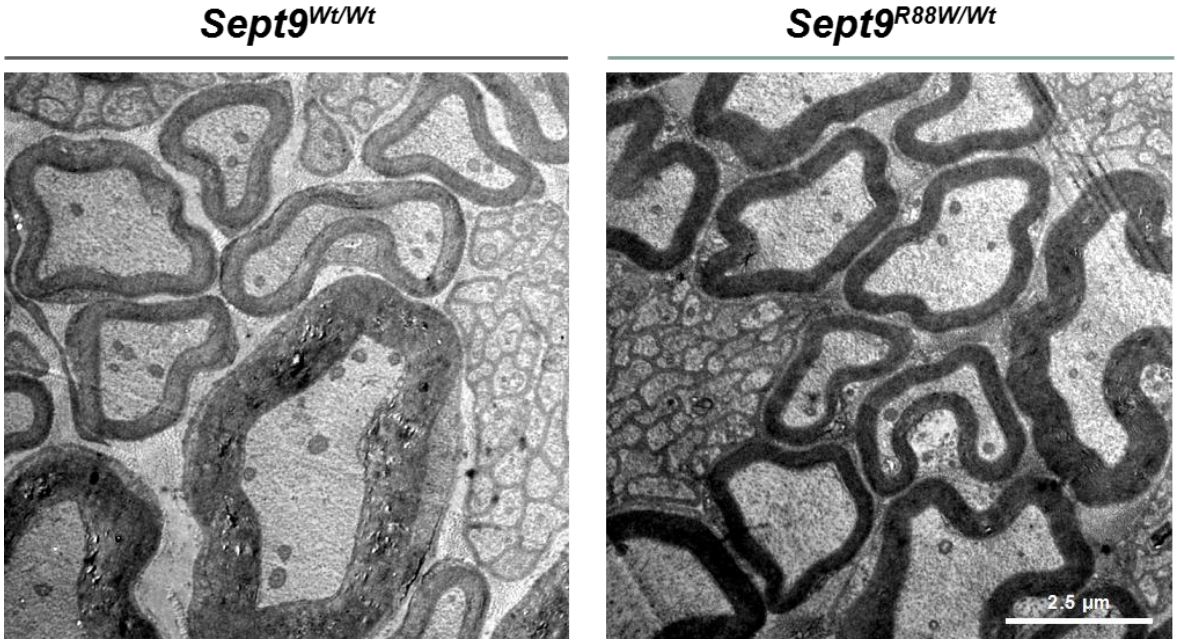

Addendum Figure 4: Myelin ultrastructure. Electron micrographs of control and *Sept9*$^{R88W/Wt}$ sciatic nerves at P75. Images illustrate normal myelination and healthy axons for both, controls (*Sept9*$^{Wt/Wt}$) and *Sept9*$^{R88W/Wt}$ mice. Remak bundles appear normal in axon numbers and axon size. Images are representative for n=4 animals per genotype.

7.3.2 Analysis of *Sept9*$^{fl/fl}$**Dhhc*+ and *Sept2*$^{fl/fl}$**Dhhc*+ mice

7.3.2.1 No alterations in axon sorting at P4

To analyze the role of SEPT9 specifically for Schwann cells, *Sept9*$^{fl/fl}$**Dhhc*+ mice were analyzed. Additionally, *Sept2*$^{fl/fl}$**Dhhc*+ mice were analyzed to identify the effect of the septin filament for Schwann cells. In Addendum Figure 5A, myelinated axons were analyzed at P4 in both, *Sept9*$^{fl/fl}$**Dhhc*+ and *Sept2*$^{fl/fl}$**Dhhc*+ sciatic nerves. The electron micrograph illustrates exemplary myelinated axons, which were considered for quantification. Axons that were enwrapped by at least one complete layer of compact myelin were considered myelinated. The quantification shows no difference in number of myelinated axons

normalized to the analyzed area, neither by comparing *Sept9*$^{fl/fl}$**Dhhc*+ sciatic nerves to controls, nor comparing *Sept2*$^{fl/fl}$**Dhhc*+ sciatic nerves to controls. As also non-myelinating Schwann cells lose the targeted gene upon recombination with *Dhh*-Cre, the impact on axon sorting out of Remak bundles was analyzed in *Sept9*$^{fl/fl}$**Dhhc*+ and *Sept2*$^{fl/fl}$**Dhhc*+ sciatic nerves (Addendum Figure 5B). The electron micrograph illustrates exemplary out-sorted axons, which were considered for quantification. Axons that were enwrapped by a Schwann cell in a one to one ratio, and axons that were partially enwrapped by compact myelin, were considered out-sorted. The quantification reveals no difference in number of out-sorted axons normalized to the analyzed area, between mutants and their respective controls.
The results indicate that both, SEPT9 and the presence of all septins, are not required to properly myelinate and out-sort axons in young mice.

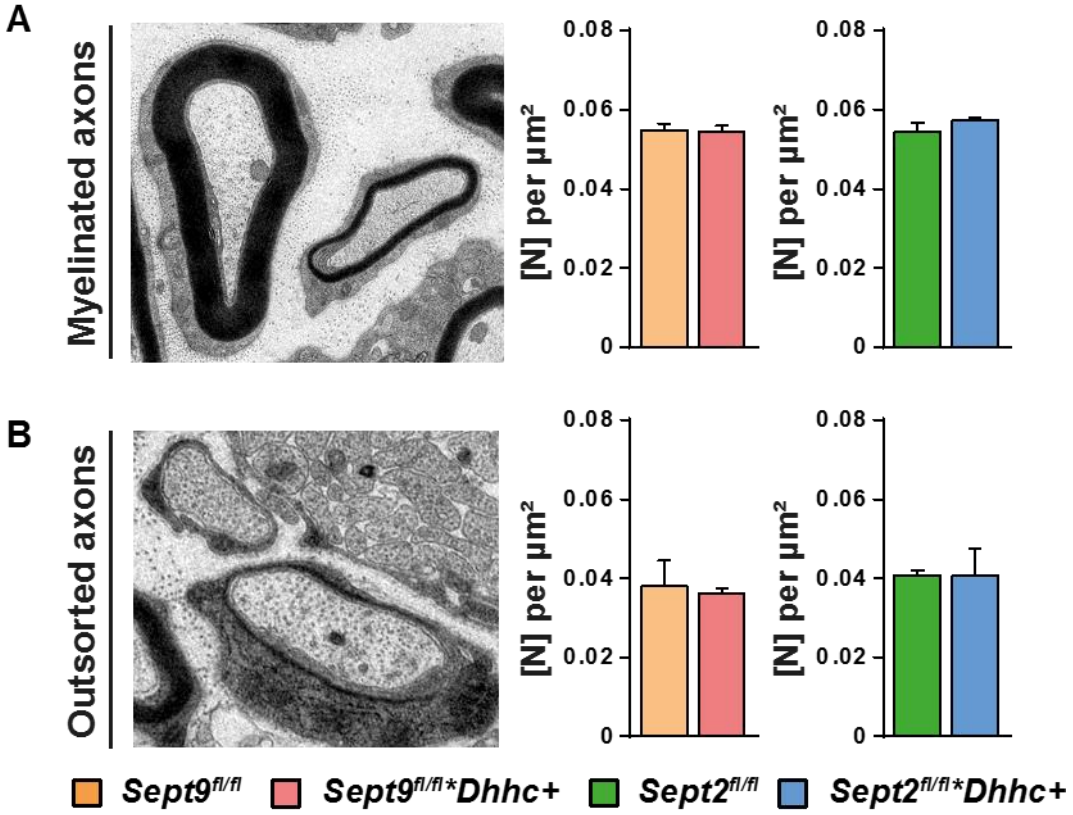

Addendum Figure 5: Sorting and myelination in *Sept9*$^{fl/fl}$Dhhc*+ and *Sept2*$^{fl/fl}$**Dhhc*+ mice at P4.** (**A**) Quantitative evaluation of myelinated axons of *Sept9*$^{fl/fl}$**Dhhc*+ and *Sept2*$^{fl/fl}$**Dhhc*+ sciatic nerves at P4. Electron micrograph illustrates examples of quantified myelinated axons. Mean +/ SEM. n= 3-4 animals per genotype; not significant according to two-tailed unpaired t-test. (**B**) Quantitative evaluation of out-sorted axons of *Sept9*$^{fl/fl}$**Dhhc*+ and *Sept2*$^{fl/fl}$**Dhhc*+ sciatic nerves at P4. Electron micrograph illustrates examples of quantified out-sorted axons. Mean +/ SEM. n= 3-4 animals per genotype; not significant according to two-tailed unpaired t-test.

7.3.2.2 Number of myelinated axons are unchanged at P14

The myelination status at P14 was analyzed in *Sept9*$^{fl/fl}$**Dhhc*+ and *Sept2*$^{fl/fl}$**Dhhc*+ sciatic nerves (Addendum Figure 6) to see whether the loss of SEPT9 or all septins lead to any impairments. All myelinated axons in sciatic nerves were analyzed and normalized to the respective nerve size. The upper row of Addendum Figure 6 depicts the quantification for SEPT9 conditional mutants and a light microscopic image of a mutant nerve. The highlighted square indicates an area of higher magnification of the sciatic nerve semi-thin section, which reveals normal appearing myelinated axons. The quantification of myelinated axons per µm² shows no difference between *Sept9*$^{fl/fl}$**Dhhc*+ mice and their respective controls. The lower row reveals the quantification for SEPT2 conditional mutants and a light microscopic image of a mutant nerve. The highlighted square indicates an area of higher magnification of the sciatic nerve semi-thin section, depicting normal appearing myelinated axons. The quantification of myelinated axons per µm² displays no difference between *Sept2*$^{fl/fl}$**Dhhc*+ mice and their respective controls.

The results suggest that neither the loss of SEPT9, nor the loss of all Schwann cell septins lead to impaired myelination at P14. Moreover, it is indicated that septins in the PNS have no effect on the developmental myelination.

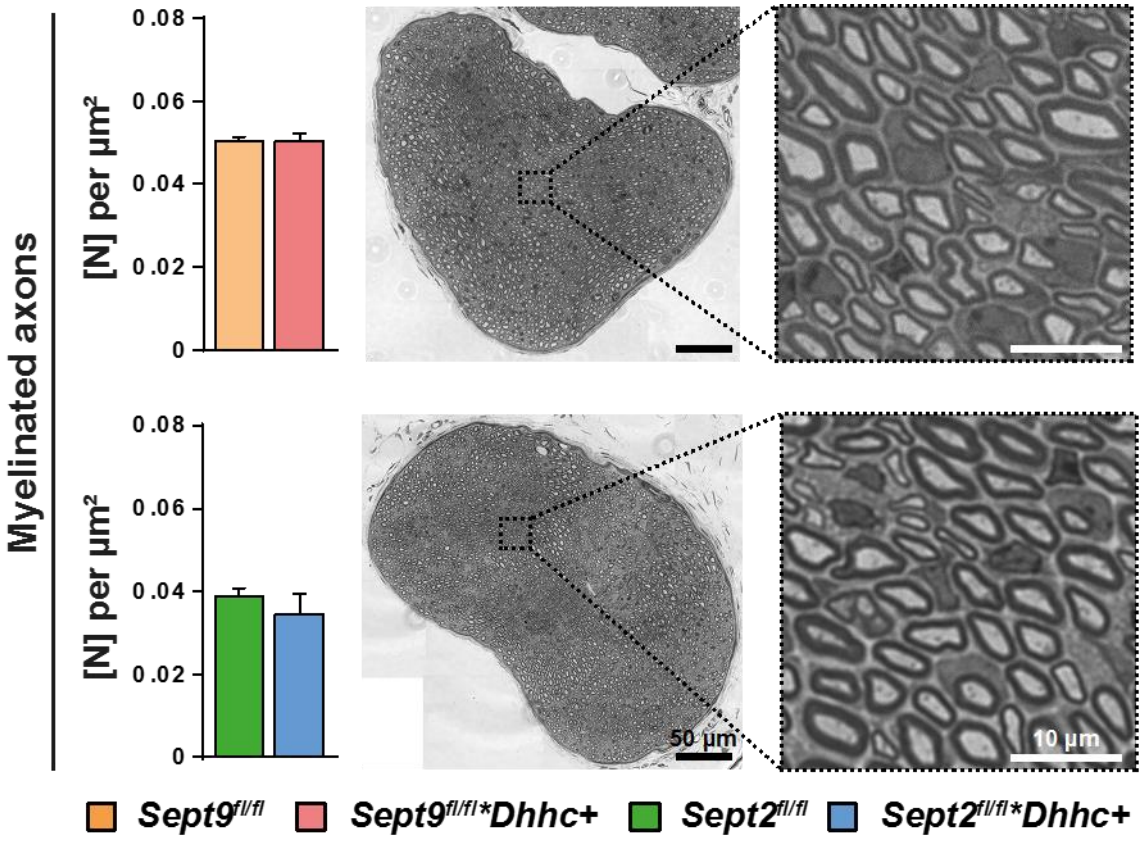

Addendum Figure 6: Myelinated axons at P14. Quantitative evaluation of myelinated axons of *Sept9*$^{fl/fl}$**Dhhc*+ and *Sept2*$^{fl/fl}$**Dhhc*+ sciatic nerves at P14. Light micrograph illustrates example of a mutant sciatic nerve (*Sept9*$^{fl/fl}$**Dhhc*+ upper row; *Sept2*$^{fl/fl}$**Dhhc*+ lower row) and a magnified image. Mean +/ SEM. n= 2-3 animals per genotype; not significant according to two-tailed unpaired t-test.

7.3.2.3 Normal myelination state at 6 mo of age

To assess the myelination status in adult *Sept9$^{fl/fl}$*Dhhc+* and *Sept2$^{fl/fl}$*Dhhc+* mice, the g-ratio was analyzed at 6 mo of age in sciatic nerves (Addendum Figure 7). The quantitative analysis reveals no differences in g-ratio between *Sept9$^{fl/fl}$*Dhhc+*, *Sept2$^{fl/fl}$*Dhhc+*, and their respective controls, suggesting that the loss of SEPT9 or PNS myelin septins have no effect on the maintenance of myelin.

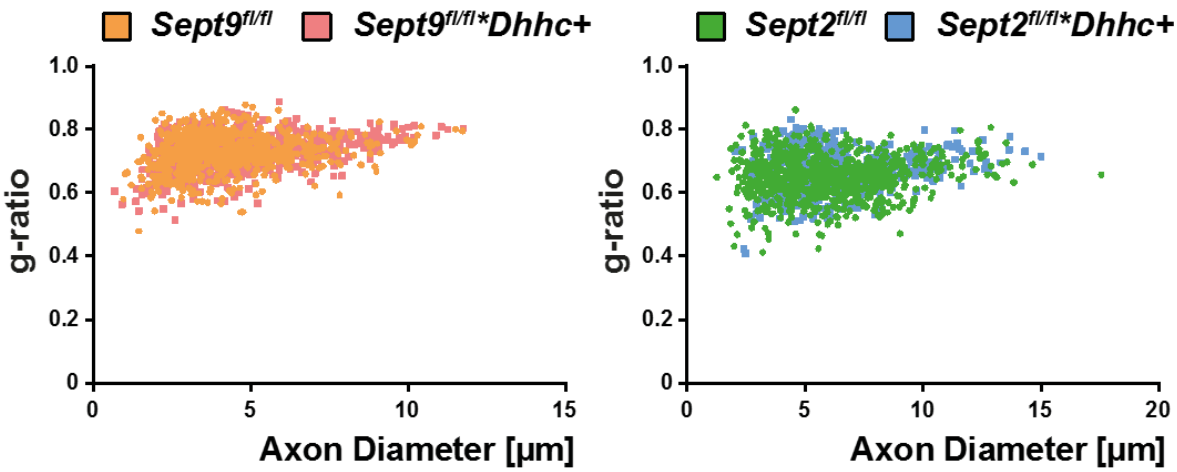

Addendum Figure 7: g-ratio in *Sept9$^{fl/fl}$*Dhhc+* and *Sept2$^{fl/fl}$*Dhhc+* mice. g-ratio analysis of electron micrographs of sciatic nerves at 6 mo of age indicates normal myelin sheath thickness in *Sept9$^{fl/fl}$*Dhhc+* and *Sept2$^{fl/fl}$*Dhhc+* mice. n=4 animals per genotype.

7.3.2.4 No changes in axon diameters *Sept9$^{fl/fl}$*Dhhc+* mice

As it was shown that septin deficient mice depict increased axon diameters in the CNS, the axon diameter frequency distribution in *Sept9$^{fl/fl}$*Dhhc+* mice was analyzed (Addendum Figure 8). For the analysis, the brachial plexus was chosen, because this nerve is mostly affected in human patients. No difference in the axon diameter distribution were found between controls and *Sept9$^{fl/fl}$*Dhhc+* mice. This was also indicated by the analysis of all axon diameters with the Kolmogorov Smirnov test.

To summarize these results, loss of SEPT9 in Schwann cells does not lead to alterations of axon diameters, which suggests that the loss of SEPT9 does not lead to alterations in axon diameter in the PNS.

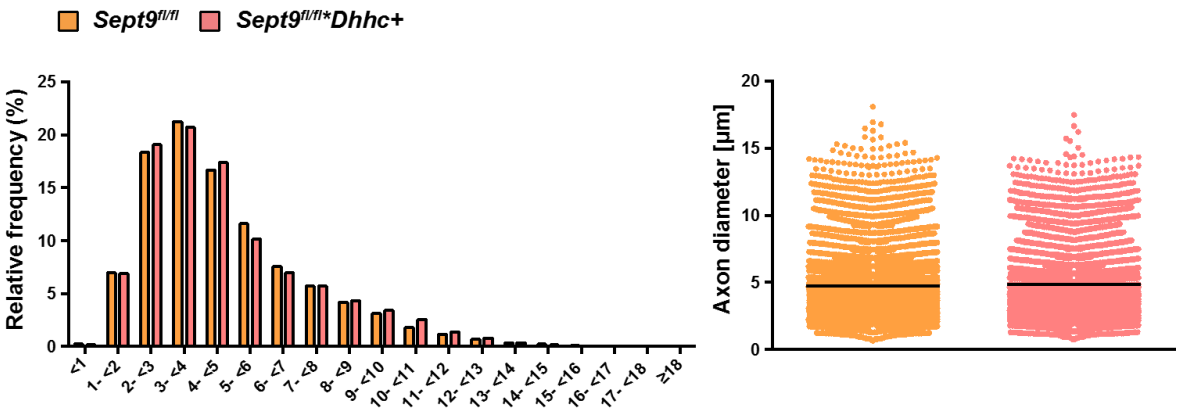

Addendum Figure 8: Axon diameter frequency distribution in *Sept9*$^{fl/fl}$*Dhhc+ mice. Frequency distribution analysis of myelinated axons in the brachial plexus of electron micrographs at 6 mo of age indicate no shift in axon diameter in *Sept9*$^{fl/fl}$*Dhhc+* mice. n=4 animals per genotype. Not significant according to Kolmogorov Smirnov test (p= 0.1746).

7.4 Perspective

The results of the performed experiment identified no significant difference between control and the different mutant mice. In previous studies, *Sept2* and *Sept9* cKO mice were analyzed more broadly (unpublished data). This analysis showed no difference in both mutants compared to controls in several different analysis including immunohistochemical labeling, behavioral tasks measuring motor and sensory capabilities, and assessment of myelin ultrastructure (unpublished data). If the emergence of HNA is related to external stress is not known. Thus, it would be interesting to challenge the three different mutants for instance by nerve compression. Similar aspects were described for other neuropathies, where conduction blocks led to the formation of outfoldings (Bai *et al.*, 2010). It is still under debate whether inflammation leads to the observed phenotype in HNA patients. To analyze this aspect, it would be interesting to induce inflammation in the PNS to activate the immune system (Wang Ip *et al.*, 2006). So far, it is known that also partial gene duplications lead to HNA (Kuhlenbaumer *et al.*, 2005). Therefore, mice overexpressing SEPT9, wild type or mutated, might be necessary to gain a genuine model for the disease.

Although lacking deeper knowledge on the disease HNA, it appears that septins seem to have different roles in CNS and PNS myelin. Although oligodendrocytes and Schwann cells form compact myelin, it seems that the mechanisms of maintaining functional compact myelin are different. It is known that the protein composition is different in oligodendrocytes and Schwann cells (Nave and Werner, 2014), as these are obviously different cell types. Nevertheless, it is remarkable that septins have a similar distribution in both cell types, but seem to have different functions.